Surface Enhanced Spectroscopy for Biosensing Applications

Shioi, Masahiko

(Degree)
博士（工学）
(Date of Degree)
2019-03-25
(Date of Publication)
2020-03-01
(Resource Type)
doctoral thesis
(Report Number)
甲第7506号
(URL)
https://hdl.handle.net/20.500.14094/D1007506

博　士　論　文

Surface Enhanced Spectroscopy for Biosensing Applications

表面増強分光法のバイオセンシング応用に関する研究

平成３１年１月

神戸大学大学院工学研究科

電気電子工学専攻

塩井　正彦

Doctoral Dissertation

博士論文

Surface Enhanced Spectroscopy for Biosensing Applications

表面増強分光法のバイオセンシング応用に関する研究

Jan. 2019

For the Degree of

Doctor of philosophy in Engineering

Graduate school of Engineering, Kobe University

神戸大学大学院工学研究科

Masahiko SHIOI
塩井　正彦

Abstract

Plasmonics is a field concerned with controlling and detecting the surface plasmon polaritons by understanding plasmonic effects which are caused by interacting electromagnetic field and free electrons of metal at the interfaces of conductive medium or in nano-scaled metallic nanostructures.

Plasmon resonance generates an electric field enhancement around the metallic nanostructures, which leads to exhibit interesting and useful characteristics to be potentially applied for extremely sensitive molecular sensors.

In order to present an overall picture about the progress in the field of plasmonics, a general introduction about plasmonics concepts, and an overview of fabrication methods for plasmonic nanostructures, optical properties, and applications of surface enhanced spectroscopy are given in chapter 1.

Chapter 2 and chapter 3 focus on the plasmonic substrates to get large enhancement in SERS for biomedical sensing applications. In chapter 2, we will discuss about plasmonic coupling with gold nanoring and gold film which is underneath the gold nanoring. For applying biomedical sensing, it's quite important to tune the resonance wavelength in near infrared region to avoid interacting the electric field with bio-related molecules. In chapter 3, we will discuss plasmonic interaction between propagating and localized surface plasmon polaritons to tune the resonance wavelength positon toward getting large enhancement.

Chapter 4 describes the plasmonic substrate development toward *in vivo* biosensor. To implant SERS substrates, there are some problems, because plasmonic substrates suffer from robustness to external forces, i.e., the release of gold nanostructures from the SiO-based support due to external forces, including laser irradiation under aqueous conditions. And biocompatibility of plasmonic substrates is also important. In this chapter, we will focus on enhancing the robustness of plasmonic substrates and its biocompatibility.

Chapter 5 focuses on the application of SEF to gain the extremely low limit of detection of fluorescence immunoassay targeted for influenza virus sensing in residential environment sensing. To detect influenza virus in air needs extremely low limit of detection. The characteristics of surface enhanced fluorescence require suppression of non-specific adsorption of the fluorescence probe to the plasmonic structure for high signal-to-noise ratio detection. Moreover the instability of antibody is crucial problem for applying for residential environment because residential environment is severe situation such as temperature, light, humidity, and cost of antibody. So we employed VHH antibody which holds great advantages in terms of large-scale production, ease of genetic modification, and resilience to organic solvents and temperature. We demonstrate successful suppression of non-specific adsorption of the fluorescence probe for high signal-to-noise ratio detection.

Finally, in Chapter 6, the results of this thesis are summarized and presented brief outlook for further study of application of surface enhanced spectroscopy for a biomedical sensing applications.

Table of Contents

Chapter 1

General introduction

1-1 Plasmonics

In recent decades, it has been revealed that metallic nanoparticles (NPs) possess a number of unique properties by the progress of research in plasmonics. However, they have a quite old history. Very notable example includes the Roman Lycurgus Cup, which was created in the 4th century. This glass cup contains silver-gold alloy nanoparticles with 70 % of silver and 30 % of gold, and 10% copper additionally and typically 50-100 nm in diameter.[1] The nanoparticles in the Roman Lycurgus Cup are origin of localized plasmon resonance, which can be excited with visible light. When it is illuminates from the outside, a green/yellow color are produced by reflecting the specific wavelength of light from the outer surface due to the effect of surface plasmon. But when a light source is inside of the cup, a red color is produced by being absorbed by specific wavelength due to localized surface plasmon resonance.[1] This effect has been also applied for fabrication of stained glass windows in historical church. But it has become to know that plasmonic resonance could cause these effects in early 1900's.[2]

In physics, the first experimental observation of collective electron oscillation was found by Wood in the research of high sensitive detector, which reported in 1902.[3] Wood discovered that "anomalous" dark band in reflection spectra of metal grating. In

Fig. 1-1 The Lycurgus cup: green/yellow color (left) was produced when light reflects from the outer surface and red (right) color was produced when it's illuminated from the inside (British Museum)

the late of 1960's, people came to know that this effect could be attributed to the excitation of surface plasmons (Otto[4] and Kreschman[5]), the collective oscillation of free electron in the metal.

In 1956, Pine proposed the term "plasmon" in his work.[6,7] The definition of plasmon is a quantum of plasma oscillation, which is caused by electric field of incident light at the interface between noble metal and dielectrics or nanostructure of which size is as same as the order of wavelength. For the behavior of light in a metal, the plasma frequency of the metal is important parameter[8]. If the frequency of light is below the plasma frequency, the electric field of the lights is screened by the electrons in the metal, which causes the light reflection at the surface of the metal. On the other hand, if the frequency of light is above the plasma frequency, because the response of electrons is too slow to screen the incident light, so the light is transmitted in the metal. The plasma frequency of the almost all of metals are in the ultraviolet (UV) region, so metals reflect the light and look shiny in the visible range, of which appearance is a feature of "metal". Some metals which have distinct color such as gold or copper, specific wavelength are absorbed due to electronic inter-band transitions in visible range.

1-1-1 Propagating and Localized surface plasmons

Surface plasmon polariton

At a boundary of metal and dielectric, there is the solution of Maxwell's equation which shows propagation of plasmon. As plasmons are propagating on the metal surface with a limited penetration depth into the metal, only the electron on the surface are significant for the propagation of collective oscillation. This collective oscillation of electron are named as surface plasmons polariton (SPPs). As depicted in Fig. 1-2, a longitudinal surface charge density propagates on the surface as SPPs mode. To derive the existence of SPs, we can start from Maxwell's equations in an infinite medium in the absence of source which are written below[8];

$$\nabla \cdot \mathrm{D} = 0 \qquad \nabla \cdot \mathrm{B} = 0$$

$$\nabla \times \mathrm{E} + \frac{\partial B}{\partial t} = 0, \quad \nabla \times H - \frac{\partial H}{\partial t} = 0 \tag{1.1}$$

where **E** is the electric field, **D** is the dielectric displacement, **B** is the magnetic induction, **H** is the magnetic field. The dielectric displacement and magnetic induction is expressed using the polarization **P** and magnetization **M** by constitutive relations in electromagnetism,

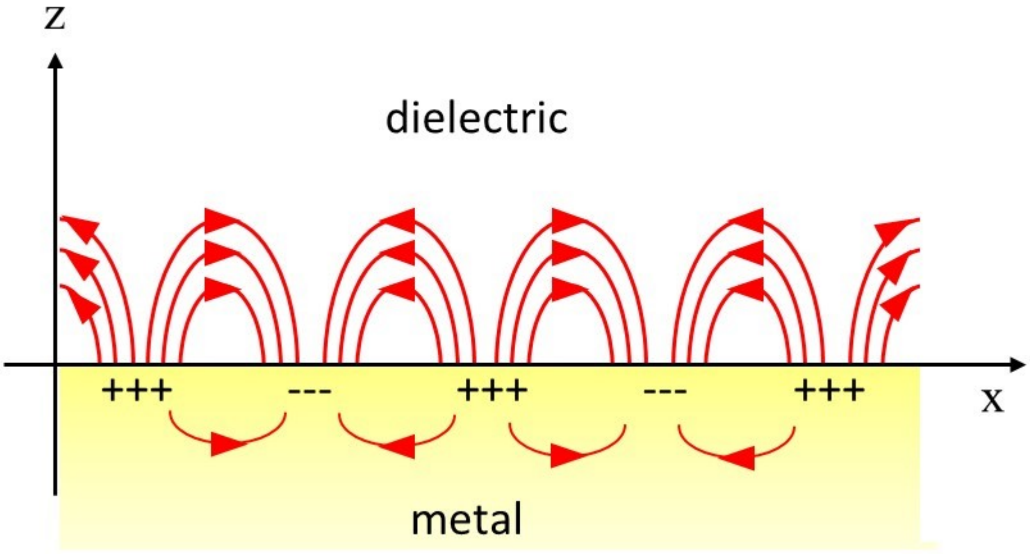

Fig. 1-2 Schematic illustration of the propagating surface plasmon on a metal-dielectric interface.[9]

$$\mathrm{D} = \varepsilon_0 E + P$$

$$\mathrm{H} = \frac{1}{\mu_0} B - M \tag{1.2}$$

where ε_0 and μ_0 are the electric permittivity and magnetic permeability of vacuum, respectively. For the non-magnetic media, we don't need to consider about magnetization. Moreover, we only deal linear, isotropic media, the equation (1.2) can be written,

$$\mathrm{D} = \varepsilon\varepsilon_0 E,\ \ H = \frac{B}{\mu_0} \tag{1.3}$$

where ε is dielectric constant. Combining curl equation about electric field, magnetic field in (1.1) and (1.2), we can get the *wave equation*

$$\nabla \times \nabla \times \mathrm{E} = -\mu_0 \frac{\partial^2 D}{\partial t^2} \tag{1.4}$$

By simplifying (1.4)[8],

$$\nabla^2 E - \frac{\varepsilon}{c^2} \frac{\partial^2 E}{\partial t^2} = 0 \tag{1.5}$$

where c is the velocity of the light in vacuum, which is defined as

$$\mathrm{c} = \frac{1}{\sqrt{\mu_0 \varepsilon_0}} \tag{1.6}$$

Then, we assume the propagating waves have a harmonic time dependence, $\mathbf{E}=\mathbf{E}e^{-i\omega t}$ of the electric field, then (1.5) can be written as;

$$\nabla^2 + k_0\varepsilon E = 0 \qquad (1.7)$$

where $k_0=\omega/c$ is the wave vector of the propagating wave in vacuum. Assuming the geometry as fig. 1-2, with non-absorbing media which means ε_2 is positive and real in half space ($z>0$) and a dielectric function $\varepsilon_1(\omega)$ with $\mathrm{Re}[\varepsilon_1]<0$ in half space ($z<0$). SPPs exist only in transverse magnetic (TM) mode. By solving (1.7) in TM mode, we can derive the dispersion relation of SPPs which propagates at the boundary of the non-absorbing media and the conducting media by following the treatment by Maier,[8]

$$\beta = k_0\sqrt{\frac{\varepsilon_1\varepsilon_2}{\varepsilon_1+\varepsilon_2}} \qquad (1.8)$$

The SPPs propagates with an in-plane wave vector β which defines the dispersion relation in fig. 1-3. The wave vector β is positioned to the right region of the light line in free space ω/c, which implies that this SPP mode can't directly excite by an incident photon. By matching the wave vector of the incident wave and the propagating SPP mode, the SPP mode can be excited by incident light. To fulfill this condition, coupling mechanism can be needed.

Localized surface plasmon resonances

In the case that surface plasmon is confined in a small volume (e.g. a NP or nanostructure), it is termed as localized surface plasmons (LSPs). A schematic illustration of LSPs is shown in fig.1-4, where the free electrons in Au NP are oscillated by the electric field of incident light. This is the origin of the above-mentioned red color of the Lycurgus cup and stained glass windows. The shape, size and density of the Au NPs determine the properties of LSP, which are resonance position, intensity of LSP resonances. The Au and silver (Ag) metals are especially important for the application of LSPs because their LSP bands are situated in the visible or near infrared region due to their dielectric function. For example, their aqueous suspensions display a strong LSP band around 510 and 400nm, respectively[10]. The analytical solutions of Maxwell's equations for metallic sphere was obtained by Mie in 1908.[2] The electric field over the nanoparticle is constant because retardation of the response is negligible, but the time dependence of wave, the wavelength dependence of the dielectric function of the metal $\varepsilon(\omega)$ and the constant or surrounding media ε_m are assumed. Under the condition of the quasi-static approximation, the Laplace equation for the potential to be solved is[8],

$$\nabla^2\Phi = 0 \qquad (1.9)$$

The electric field can be written as a divergence of the potential,

$$\mathrm{E} = -\nabla\Phi \qquad (1.10)$$

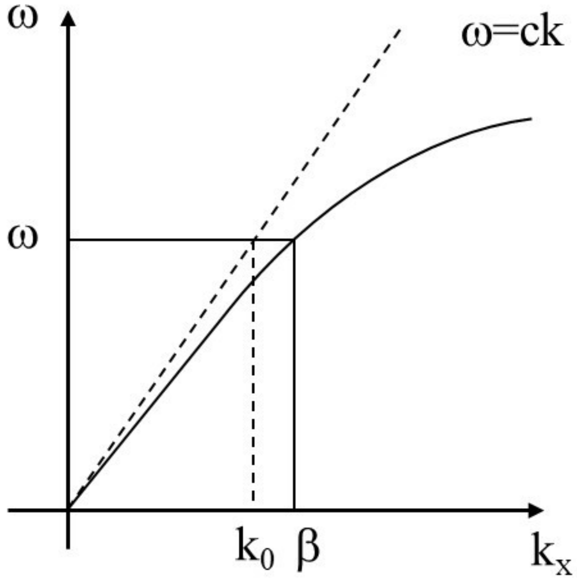

Fig. 1-3 The dispersion relation of an SPP, difference of the momentum mismatch between the propagating light and SPP.[9]

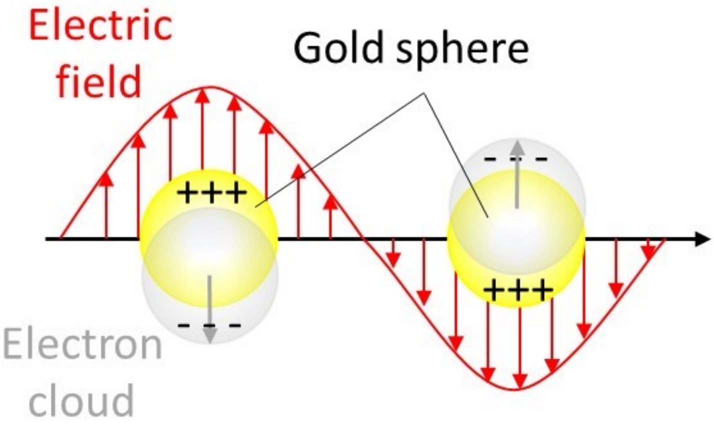

Fig. 1-4 Schematic illustration of localized surface plasmon resonance on gold nanoparticles

By taking into account the azimuthal symmetry of the problem depicted in Fig. 1-5, the general solution of the (1.10) can be written below,[11]

$$\Phi(r,\theta)=\sum_{l=0}^{\infty}\left[A_l r^l + B_l r^{-(l+1)}\right]P_l(\cos\theta) \qquad (1.11)$$

where $P_l(\cos\theta)$ are the l^{th} order of Legendre Polynomials, and θ the angle between the z-axis and the position vector at point P as depicted in Fig.1-5. Considering the equation (1.11) by separating the inner field of metallic sphere and scattering field with proper boundary conditions, finally the solution for the potentials inside Φ_{in} and outside Φ_{out} of the sphere can be obtained as[8]

$$\Phi_{in}=-\frac{3\varepsilon_m}{\varepsilon+2\varepsilon_m}E_0 r\cos\theta \qquad (1.12a)$$

$$\Phi_{out}=-E_0 r\cos\theta+\frac{\varepsilon-\varepsilon_m}{\varepsilon+2\varepsilon_m}E_0 a^3\frac{\cos\theta}{r^2} \qquad (1.12b)$$

The first term of right side in equation (1.12b) shows the applied electric field and second term shows a radiation from the induced dipole by applied field. From the denominator of (1.12b), if the $\mathrm{Re}[\varepsilon(\omega)+2\varepsilon_m]$ reached a minimum, a resonant behavior is expected to occur. For noble metals, the real part of the permittivity in visible or near infrared region is negative. So the Frölich resonance condition is obtained;[8]

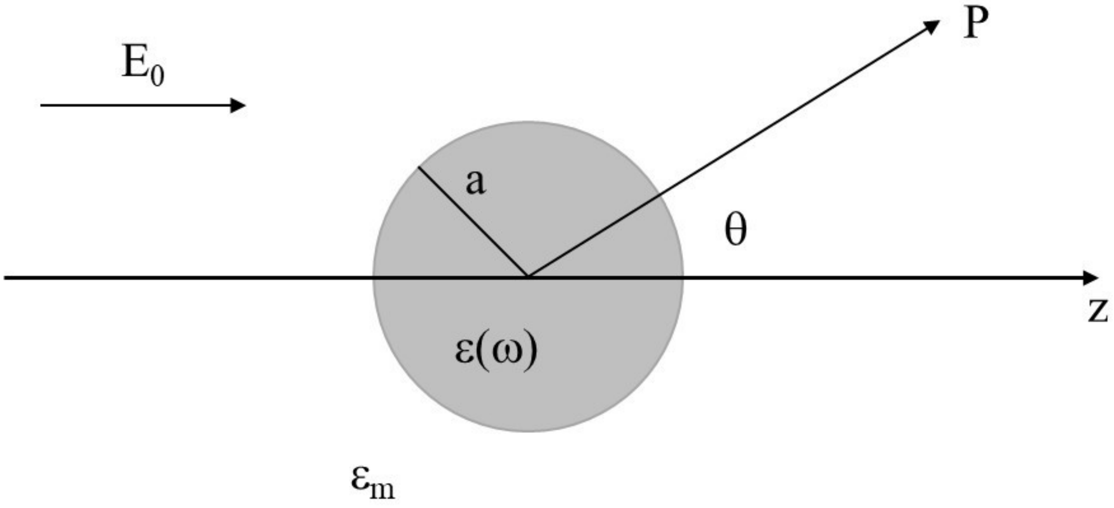

Fig. 1-5 Illustration of a homogenous sphere placed into an electrostatic field

$$\varepsilon(\omega) = -2\varepsilon_m \qquad (1.13)$$

When (1.13) is satisfied, the inner and outer electric field of the nanoparticle will be resonantly enhanced, because the denominator of (1.12) reaches minimum.

As the plasmon resonance is collective oscillation of the free electron in the metallic nanostructure, so the damping of the resonance depends on the imaginary part of permittivity, because imaginary part of permittivity means resistance so the electron oscillation damps due to its resistance. As the dielectric constant ε_m of the surrounding medium is getting larger, the resonance position changes to longer wavelength. This principle is often used in refractive index sensing which is often applied for biomedical LSPR based sensor. As above mentioned, there will be a tremendous near-field electric field enhancement of the incident wave, dipole radiation of the excited dipole in the nanoparticle as shown in equation (1.12), which is also often applied biochemical LSPR based sensor, surface enhanced spectroscopy.

1-2 Surface Enhanced Spectroscopy

1-2-1 Surface Enhanced Raman Spectroscopy

Surface Enhanced Raman Spectroscopy (SERS) effect is about amplifying Raman signals by several order of magnitude to detect single molecules.[12] To understand SERS effect, we need to know about Raman scattering at first, Raman effect was discovered by C. V. Raman at 1928[13], and now, Raman spectroscopy has been used as a useful characterization method for molecules. Raman spectroscopy has a complementary relationship with infrared adsorption spectroscopy.[14] Raman scattering doesn't require the energy matching of the incident light with the energy between the ground state and excited states like infrared absorption spectroscopy. In Raman scattering, by interacting incident light with the molecule, incident photon distorts/polarizes the electron cloud around the atomic nucleus, which form a 'virtual state' and the photon is quickly transited into ground state due to its instability and radiate Raman scattering photon (Fig.1-16(A). This process is called Stokes scattering (Fig.1-6(B)). In case that some molecules exist in an excited state due to thermal energy, shown in Fig. 1-6(A), and the different scattering called anti-Stokes scattering is occurred (Fig.1-6(B)). Typically, Raman scattering is very weak because Raman cross-section of molecules is very small.

Historically, SERS was discovered in the 1974 by Fleischmann, who investigated about Raman spectra of pyridine adsorbed on electro-chemical roughened electrode[15] et al, which is considered as the first observation of the SERS effect, and was originally explained by Jeanmaire and Van Duyne[16] and Albrecht and Creighton[17] in 1977. Since then, SERS has largely been used by the scientists of the condensed matter physics and chemical physics communities. The amplification of the Raman scattering in SERS caused by surface plasmon resonance, which produces large enhancement of the electromagnetic field of incident light. To get profits from this phenomenon, the molecules which produce Raman scattering typically should be adsorbed on the metal surface, or be placed in the proximity to the surface of plasmonic structures, typically ~10 nm at maximum. The mechanisms of SERS are considered as an effect from electromagnetic enhancement and chemical enhancement[7].

For the electromagnetic enhancement, electromagnetic field of incident light is strongly enhanced by LSPR. The electric field generated $\mathbf{E}_{loc}$ on plasmonic nanostructure surface by LSPR can be much larger than the incident field $\mathbf{E}_{inc}$. $\mathbf{E}_{loc}$ is called local field. It is the macroscopic electric field felt by the molecule. The local field $\mathbf{E}_{loc}$ induces the Raman dipole[7]

$$\mathbf{p}_R = \alpha_R \mathbf{E}_{loc}(\omega_L) \qquad (1.14)$$

where α_R is the Raman polarizability of the molecule, ω_L is the frequency of the incident field. The equation (1.14) shows that the magnitude of a Raman dipole is enhanced by the enhanced field $\mathbf{E}_{loc}$ by a factor of $|\mathbf{E}_{loc}(\omega_L)|/|\mathbf{E}_{inc}|$. If this Raman

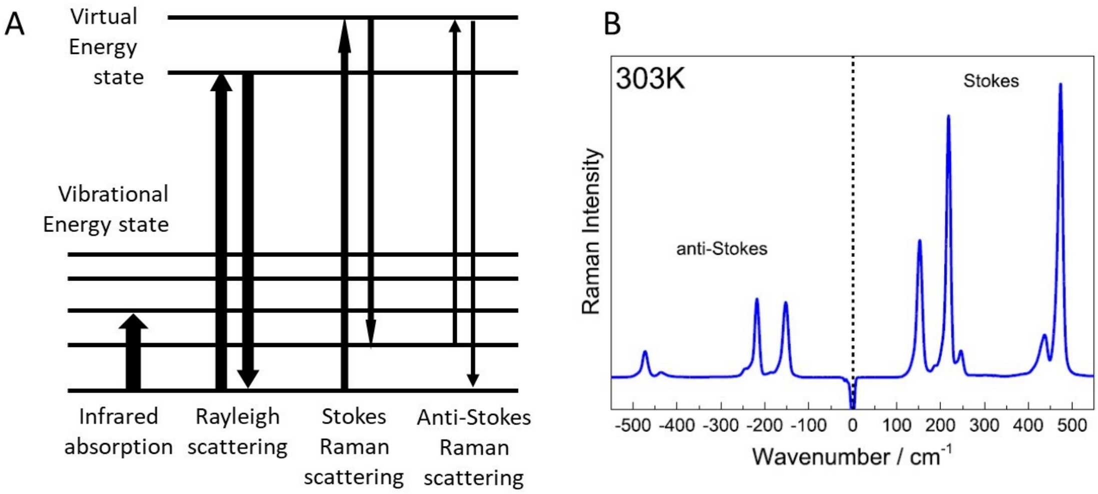

Fig. 1-6 (A) Energy state diagram in Raman scattering. The line thickness is roughly proportional to the signal intensity. (B) Stokes and anti-Stokes Raman scattering of β-sulfur at 303K.[187]

dipole radiates in free-space, the intensity | $\mathbf{p}_R$ |^2 is enhanced by a factor:

$$M_{LOC}(\omega_L) = \frac{|E_{LOC}(\omega_L)|^2}{|E_{inc}|^2} \qquad (1.15)$$

This factor, which is called as the *local field intensity enhancement factor*[7], is originated from the enhancement of the Raman dipole emission by the incident electric field enhancement due to plasmonic resonance. For an absorbing molecule which is important for surface enhanced fluorescence, it is also associated with the absorption enhancement, which will be discussed in the next section.

In SERS, we need to take into account the enhancement of Raman scattering itself. The Raman dipole radiates in close proximity to the plasmonic metal structure while SERS occurs. The radiation of Raman dipole is strongly affected by the electromagnetic field modified by plasmonic nanostructure, in a similar way with the incident field for Raman excitation. This phenomenon is called as modified spontaneous emission.[7] The modified electromagnetic field affects the Raman scattering in the radiation pattern and the total radiated power by the Raman dipole. Several factors such as the nanostructure and detection setup, optical properties of molecule and nanostructure, the dipole position and orientation, and its emission frequency ω_R[7]. Overall, this leads to an enhancement by a factor of $M^d_{Rad}(\omega_R)$ of the collected Raman signal compared to Raman dipole in free-space. This radiative enhancement factor is linked to the re-emission step in the Raman process. When we consider only these electromagnetic enhancement mechanisms (excluded chemical enhancement) which means a local field enhancement for incident field enhancement and radiation enhancement in Raman process, the SERS EM enhancement factor can be simply written below:

$$\begin{aligned}\mathrm{EF} &\approx M_{Loc}(\omega_L)M_{Rad}^{d}(\omega_R) \\ &\approx \frac{|E_{Loc}(\omega_L)|^2}{|E_{Inc}|^2}\frac{|E_{Loc}(\omega_R)|^2}{|E_{Inc}|^2}\end{aligned} \tag{1.16}$$

This equation has been extensively used and introduced as *$|E|^4$-approximation* although a more accurate description has been given by Kerker.[19] This equation provides a simple way to estimate the single molecule enhancement factor from an electromagnetic field calculation at the excitation and Raman frequencies. And also this expression implies that it’s important to match the LSPR resonance to the excitation wavelength and Raman frequency to get the large enhancement factor.

1-2-2 Surface Enhanced Fluorescence

The SERS enhancement mechanisms shown in the previous section, it is also related to other processes such as fluorescence. The modification of fluorescence due to electromagnetic modification due to surface plasmon resonance called surface enhanced fluorescence (SEF) or metal enhanced fluorescence (MEF) , which is intensively being researched.[20–26]

Fluorescence is similar process to scattering. First, incident photon is interacted with molecule, then absorption process occurs, then followed by fluorescence emission process. So a similar enhancement mechanism with SERS are expected. For the absorption process, absorption is affected by the incident field intensity as shown in the previous section. And the emission should be expected to be associated with the radiative enhancements. The absolute difference in SERS and SEF is that transition process of excitation and relaxation is instantaneous process or not. Raman process is instantaneous process and fluorescence is multi-step process shown in Fig.1-7[7]. For enhancement of fluorescence, involved mechanisms are absorption enhancement by local field enhancement by plasmon resonance and modification of the radiative and non-radiative decay rates due to local enhanced field.

The optical power absorbed by a molecule at free-space can be expressed as $P^{M}_{abs}=\sigma_{abs}n_{M}\varepsilon_{0}c|E|^{2}/2$, where $\sigma_{abs}|$ is absorption cross section, n_M is a refractive index of medium, and $n_{M}\varepsilon_{0}c|E|^{2}/2$ means power density of incident field. At the field enhanced situation due to LSPR, the local electric field $|E_{Loc}|$ is applied to the fully random

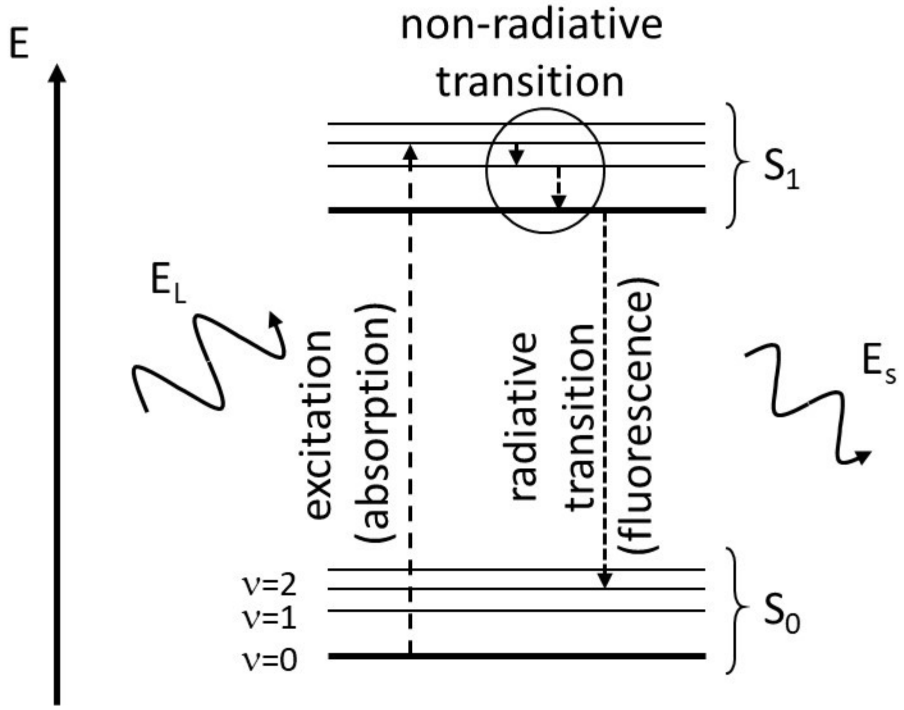

Fig. 1-7 Simplified Jablonski diagram of the fluorescence process in a molecule.[7] *Incident photon of energy* E_L *excites an electron in a molecule from a ground state* S_0 *to a sub-level of the excited state S1. The excited electron in* S_1 *relaxes a fast non-radiative transition in the ground state of* S_1 *followed by a radiative transition to* S_0*, with emission of a photon at energy* $E_S < E_L$*.*

oriented molecules. Then, the absorption enhancement factor $M_{Abs}(\omega_L)=P_{Abs}/P^M_{Abs}$ can be written[7]:

$$M_{Abs}(\omega_L) = M_{Loc}(\omega_L) \qquad (1.18)$$

where $M_{Loc} = {|E_{Loc}|^2}/{|E_{Inc}|^2}$. which is same with the case of SERS. The field enhancement due to LSPR, quantum yield is also affected by enhanced electromagnetic field. The quantum yield in free-space is expressed as following:

$$\mathrm{Q}^M = \frac{\Gamma^M_{Rad}}{\Gamma^M_{Tot}} = \frac{\Gamma^M_{Rad}}{\Gamma^M_{Rad} + \Gamma^M_{NR}} \qquad (1.19)$$

where Γ^M_{Rad} is free-space radiative decay rate, $\Gamma^M_{Tot} = \Gamma^M_{Rad} + \Gamma^M_{NR}$ is total decay rate in free-space, Γ^M_{NR} is intrinsic non-radiative decay rate. At the proximity to the metal surface, as mentioned above, radiative decay rate is affected by LSPR in following two effects: (1) the radiative decay rate Γ_{Rad} is enhanced by a factor of M_{Rad}: $\Gamma_{Rad} = M_{Rad}\Gamma^M_{Rad}$, and (2) the non-radiative decay, which is another route corresponding to absorbed emission into the metal with a non-radiative decay EM rate in addition to the intrinsic non-radiative decay with Γ^M_{Rad}, which is written as $\Gamma^{EM}_{NR} = M_{NR}\Gamma^M_{Rad}$. The modified quantum yield is expressed as:

$$\mathrm{Q} = \frac{\Gamma_{Rad}}{\Gamma_{Rad} + \Gamma^{EM}_{NR} + \Gamma^M_{NR}} \qquad (1.20)$$

By considering low of energy conservation, the relationship of enhancement factor is expressed as $M_{tot} = M_{NR} + M_{Rad}$. The modified quantum yield for fluorescence emission at frequency ω_s is finally written by using equation (1.19) and (1.20)[7],

$$Q = \frac{M_{Rad}(\omega_s)}{M_{Tot}(\omega_s) + (Q^M)^{-1} - 1} \tag{1.21}$$

Quantum yield should be within range of 0 to 1 from the definition. This means that if quantum yield in free-space is already close to 1, the enhancement can't be obtained.

By combining the absorption enhancement and quantum yield enhancement, we can define the fluorescence enhancement. In this discussion, neglecting the Stokes shift. in the excitation and emission frequency as normal fluorophore has the small. Ignoring also saturation effect, the fluorescence cross-section can be defined as $\sigma_{Abs}Q$. The fluorescence enhancement factor, M_{fluo}, is defined as the modified cross-section due to plasmon resonance divided by the free-space cross-section, which is written as[7]:

$$M_{Fluo} = \frac{\sigma_{Abs}Q}{\sigma_{Abs}^{M}Q^M} = M_{Loc}\frac{M_{Rad}}{Q^M M_{Tot} + (1 - Q^M)} \tag{1.22}$$

From equation (1.22), to get large fluorescence enhancement, it's important to enlarge the local field enhancement factor mentioned in the first term. And for the fluorophore emitting near-infrared fluorescence which is important for the biosensing application from the optically transparent point of view for the bio-related molecules, the quantum yield is normally not good. So the third term is also important.

1-3 Applications of plasmonics and surface enhanced spectroscopy and its underlying technologies

As discussed in previous section, plasmonics and surface enhanced spectroscopy (SERS and SEF) are quite high sensitivity to a change of environmental dielectric constant, huge amplification of Raman scattering, fluorescence. In this section, we will overview the technologies behind the biosensing application at first. Then we will review the application of plasmonics, SERS and SEF, especially for biosensing applications.

1-3-1 Surface functionalization

To realize biosensing applications in plasmonics, it is critical to facilitate analyte brought in the vicinity of plasmonic substrates in order to detect accurately and sensitively. To realize this situation, it's quite important to control the surface property of plasmonic substrate. For this purpose, chemically surface functionalization is used to control the surface property of plasmonic substrates. Plasmonic substrates are normally fabricated by noble metal or silicone dioxide, which can be chemically functionalized by using special chemicals which have special functional end group. Noble metal surfaces show a high affinity for thiol end group,[27] while silicon dioxide and silicon surfaces show a high affinity for silane end group.[28] Both thiol and silane forms monolayer by self-assembly on gold and silicone-based surface with quite high coverage. Typically, the SAM molecules consist of two functional end group and alkane chain between two functional end groups. The long alkane chain gives them densely packed monolayer due to Van Der-Waals bonds forming with neighboring molecules. These compounds has a thiol or silane end group on one side for coupling with a surface of plasmonic substrates, and can be chosen the other side for coupling with desired molecules such as antibody, deoxyribonucleic acids (DNA). For example, to couple antibody to a surface of plasmonic substrates, we can choose the carboxyl end group to couple antibodies via 1-Ethyl-3-(3-Dimethylaminopropyl) Carbodiimide/ N-Hydroxysuccinimide (EDC/NHS) chemistry depicted in Fig1-8.[29] And also surface hydrophobicity or hydrophilicity can be controlled by choosing the suitable end group. For example, if the methyl end group is chosen as the other side of thiol or silane end group, the surface shows hydrophobicity. If the hydroxyl end group is chosen, the surface of plasmonic substrate shows hydrophilicity. The control of surface hydrophilicity is also important to avoid non-specific adsorption of protein such as antibody, analyte itself, which leads to rise background signal and make an assay incorrect.[30]

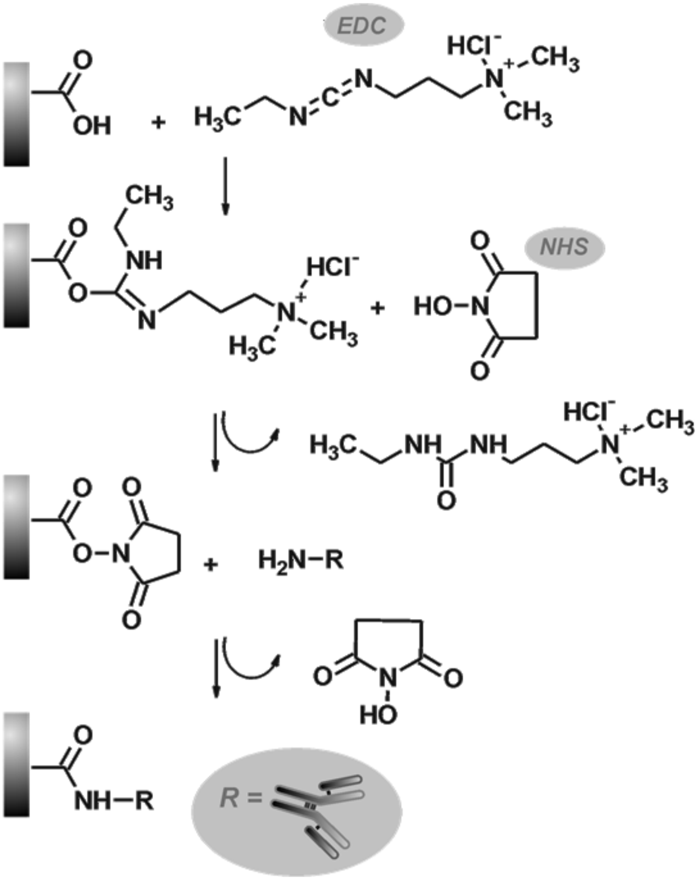

Fig. 1-8 Reaction mechanism of EDC/ NHS reaction. EDC attacks the carboxyl end group and activates. Then NHS couples to carboxyl end group by substitution reaction with residue of EDC. Furthermore, substitution reaction between primary amine on the molecule (e.g. antibody) and NHS occurs and covalently coupled carboxyl end group and the molecule.

1-3-2 Immunoassay

A biosensing is a process used to determine the concentration of a desired target analyte in a sample (blood, urine, etc.). Immunoassays are defined by IUPAC (International Union of Pure and Applied Chemistry) as ligand-binding assays making use of specific antigens or antibodies to quantify a target analyte. As such, immunoassays derive their unique properties from the characteristics of antibodies. Antibodies have an outstanding specificity towards their antigen, which was discovered by Behring and Kitasato at 1890.[31] This specificity arises from a small part of the antibody, called the variable domain, which can recognize specific parts on the antigen.[31] Furthermore, antibodies have a high strength affinity towards an antigen. This strength mainly arises from the conformational complexity which determines the proximity of the antibody-antigen interaction. This interaction involves multiple non-covalent bonds, for example hydrogen bonding between hydrophilic groups, electrostatic interactions between oppositely charged ionic groups, van der Waals forces and hydrophobic interactions between non-polar groups (Fig.1-9). Finally, antibodies have the ability to bind a broad range of chemicals, biomolecules, cells and viruses. Since antibodies consist of an arrangement of amino acids, a large variety of potential combinations can be obtained in response to antigenic stimulation.

A large variety of immunoassays has been developed and characterized. We will focus on the sandwich assay which is most commonly used for applications in plasmonics.

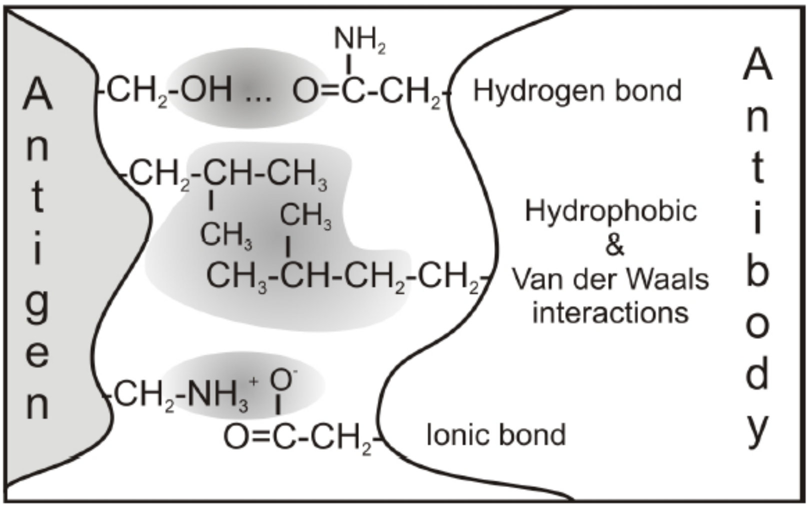

Fig. 1-9 Schematic illustration of noncovalent interaction between antigen and antibody (Adopt from R. A. Goldsby, et al. (2000) "Immunology", New York: W. H. Freeman & Co.)

The "sandwich" assay, a configuration that sandwiches the analyte between two highly specific antibodies, i.e. the primary and secondary labeled antibody, as shown in Fig. 1-10. The signal produced by the labeled antibody is related to the amount of antigen in the sample. This assay provides an increased sensitivity, and selectivity due to the recognition of two sites in the antigen by primary and secondary antibody. If the Raman probe or fluorophore is employed as a label for secondary antibody, we can directly applied for SERS or SEF to enhance the sensitivity of immunoassay, which is the most focused on this thesis..

Fig. 1-10 Schematic illustration of sandwich immunoassay

1-3-3 SPR biosensor

SPR biosensor is one of the most successful commercial platforms [32] in life science for analyzing molecular interaction such as antigen-antibody reaction. Fig.1-11 shows the schematic illustration of the sensing principle. A solution containing an analyte such as antigen flows through a flow cell which is contact with a gold film surface. The gold film surface is often functionalized with functional molecules which is interacted with the analyte. A angled beam which is p-polarized excites surface plasmon polariton on the gold surface with the Kretschmann configuration.[5] By scanning the incident angle of the excitation beam, a minimum of reflectance is observed at the angular potion where SPPs are excited. These SPPs are affected by the dielectric environment change which is caused by the interactions with analyte and the functional molecules.

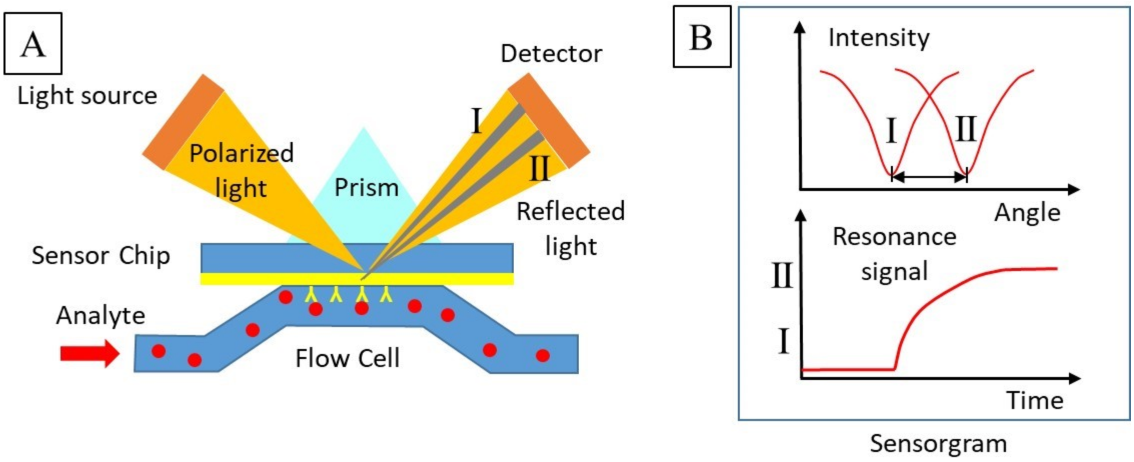

Fig. 1-11 (A) Schematic illustration of a SPP biosensor. (B) Example of Sensorgram. (Upper) By binding analyte with functional molecules immobilized to gold surface, a dip is shifted I to II due to the dielectric constant change. (Below) Rewritten the angular change into time. The amount of analyte interacted with functional molecules change is shown in time course.

As a result of the interaction, a shift in angle where reflectance is minimum will be observed corresponding to the dielectric environment change. Typically, with the increase of binding amount of analyte with functional molecules such as antibody, local refractive index is increased, resulting in a shift of the angular position to large value due to the change of the condition of SPP coupling to the gold film. Therefore SPP based sensors are sensitive to concentration changes in the bulk and to molecular interaction at the gold surface. Actually, SPP-based biosensor is widely used in the field of antibody research, affinity analysis[33,34], kinetics analysis,[33,35–37] thermodynamics analysis,[38–41] selection of antibody,[42] or analysis of macromolecules' interaction[43].

1-3-4 LSPR biosensor

LSPRs have high susceptibility to the change of refractive index of surrounding medium. When the refractive index of surrounding medium is increased, plasmon resonance wavelength of LSP shows red-shifts. And this red-shift can be detected easily by colorimetric detection without using a special instrumentation.[44] Many papers of colorimetric assays have focused on the research of nucleotide interactions by using oligonucleotide-modified Au nanostructures, and a detection limit in the range of sub-picomolar has been achieved.[45] For example, Mirkin et al reported a quantitative assay which detected target probes between 5 nM to 50 pM by using oligonucleotide-functionalized 50 nm Au nanostructures.[46] Spherical Au nanoparticles are most frequently used, but non-spherical Au nanostructures are also applicable,[47] as well as nanostructures of other noble metals.[48] These methods are interesting because sensing for specific target can be executed by functionalizing the surface of nanostructures with easy method to provide molecular selectivity.

Refractive index changes in the proximity of the surface of metallic nanostructures in solution or nanostructures on a substrate, cause measurable the LSPR wavelength shift and/or magnitude. This method can be applied for the detection of label-free chemical or bio-related molecules with real time. The sensitivity of such sensing system is commonly described by the change in resonance shift or magnitude of reflectance per ‘refractive index unit’ (RIU), which is linked to the parameters’ change when the amount of refractive index change is 1. Numerous LSPR biosensors using different shape nanostructure dispersions have been reported. Two typical examples are spherical Au nanostructure and Au nanorod dispersions. Ghosh et al found that the LSP resonance wavelength is shifted linearly with the change of refractive index[49]. More useful application, Yu and Irudayaraj reported the multiplexed bioanalytical sensing capability by using different aspect ratios of Au nanorods in solution.[50]

Nanostructures on the substrates can also be used for LSPR biosensor. They usually provide some attractive feature: (1) controllability of the nanostructures by using lithographic fabrication methods to tune resonance wavelengths and (2) no chemical agents for control of shape of nanostructure while synthesizing such as Au nanorods, or stabilizers for preventing the shape change of nanostructure, which leads to the surface functionalization with specific receptors or ligands more effectively. When spherical Au or Ag nanoparticles and Au nanorods synthesized in solution were immobilized on the substrates, they exhibited the resonance wavelength change of ~167,[51] ~76,[52] and ~ 252 nm/RIU,[53] respectively. The sensitivity can be improved by using spherical Au nanoshells and Au nanorice to ~555,[25] ~800 nm/RIU,[54] respectively. Au nanorings which were fabricated by Nanosphere Lithography have shown an even larger plasmon resonance wavelength change of ~ 880 nm/RIU and ~5.2 nm of a resonance wavelength shifted when a one of the CH_2 unit of elongated alkane chain length of self-assembled monolayers (SAMs) were immobilized.[55] Plasmonic nanostructures of other geometries on the substrate were applied for LSPR sensing as well, e.g. Ag nanotriangles,[56,57] single Au nanodisks,[58] single Ag nanocubes,[59] Au nanoislands,[60] and Au nanoholes.[61–63]

1-3-5 Surface-Enhanced Raman Spectroscopy

Surface-enhanced Raman Spectroscopy is a very powerful technique for advanced biosensing or environmental applications[12,64,65] because SERS has ability to distinguish or specify molecules by its spectral feature in addition to its huge enhancement. For the SERS for sensing applications, there are two configurations which is called a direct SERS,[66] and the other is an indirect SERS.[66,67] Fig. 1-12 shows a schematic illustration of indirect SERS and direct SERS. For indirect SERS, Raman label such as 4-aminothiophenol, 4-chlorobenzenthiol which exhibits large Raman intensity is immobilized to functional molecules such as DNA, antibody for analyte recognition.

For direct SERS, analyte can be interacted with plasmonic structures, therefore intrinsic SERS from analyte can be detected and the analyte is recognized by analyzing SERS spectra from the analyte.[66]

In another point of view, SERS can be classified *in vivo* assay and *in vitro* assay. For example, Yuen et al reported *in vivo* blood glucose measurements using SERS. Fig. 1-13 (A) show the schematic illustration of measurement setup. The Ag film over nanosphere (AgFON) substrate was functionalized with decanethiol and 6-mercapto-1-hexanol for partitioning glucose molecules and was implanted into subcutaneous tissue of Sprague-Dawley rat. Fig 1-13 (B) shows the measurement result. They succeeded to detect glucose concentration in interstitial fluid by collected SERS spectra at the mean

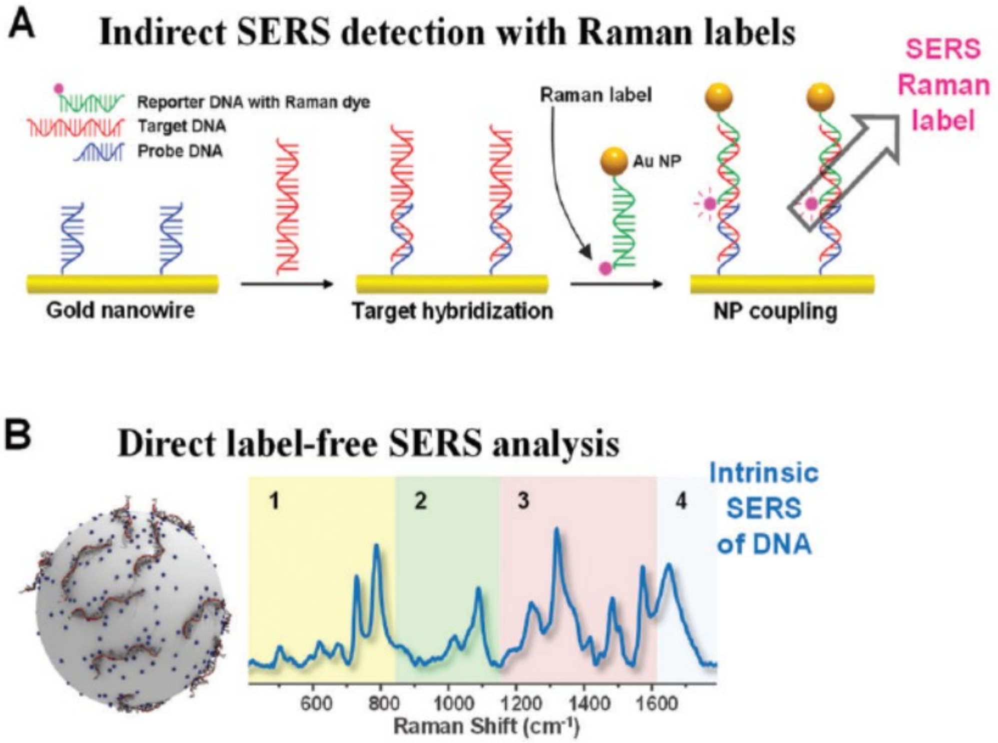

Fig. 1-12 (A) Schematic illustration of indirect SERS approach; molecules to be detected is recognized by functional molecules such as DNA, antibody. SERS from Raman label is detected, which is immobilized Au NP and functional molecule for SERS and molecular recognition (B) direct SERS approach; analytes are interacted with Au NPs and read out the SERS spectrum. Molecular recognition is done from the analysis of intrinsic SERS spectrum from analyte.[66]

absolute relative difference values for calibration was 16.6% and for validation 34.6%.[68] For *in vitro* application, there are quite lot of reports, for DNA,[67,69] cancer markers such as prostate specific antigen,[70–73] viral diseases such as influenza,[74–77] hepatitis B,[69,78,79] and also applications for environmental sensing such as trinitrotoluene[80,81] as an explosive detection, pollutants in soil,[82] air,[83] and water.[84,85]

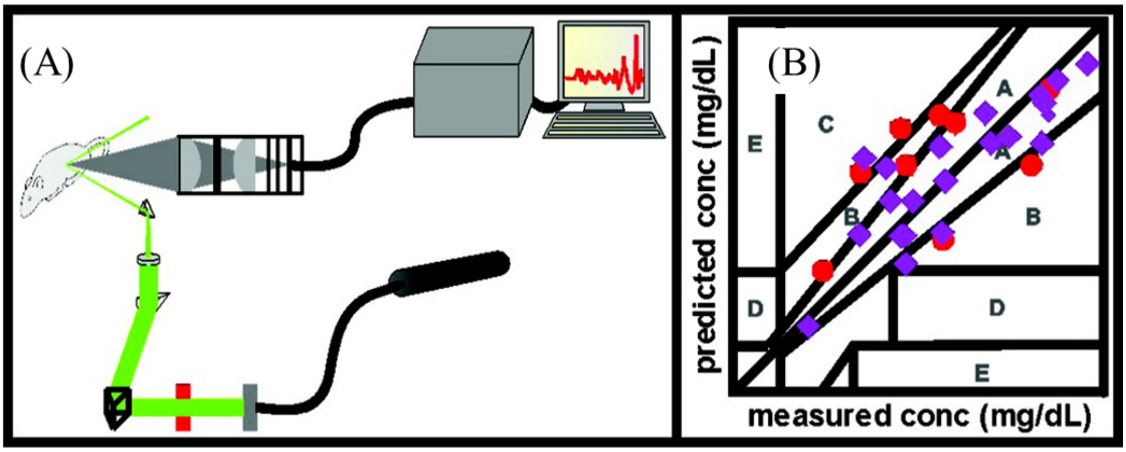

Fig. 1-13 (A) schematic illustration of measurement setup. (B) Calibration (◆) and validation (●) sets of the first in vivo transcutaneous glucose measurements.[68]

1-3-6 Surface enhanced fluorescence

Compared to SERS, surface enhanced fluorescence (SEF) has not been paid much attention because its enhancement factor is only determined by absorption enhancement in case of usage of good fluorophore, which leads to obtain small enhancement compared to SERS. But SEF has been intensively investigated especially in the field of immunoassay applications[20,22,23,86,87] or excitation of fluorescence for quantum dots at low absorption wavelength region such as silicon quantum dot (Si-QD) excitation at visible or near infrared region[88–90], which has great potential for biomedical application because Si-QD doesn't have an intrinsic toxicity and can be a suitable fluorophore for *in vivo* application[91]. Excitation by near-infrared wavelength is very important from the biomedical point of view because biomedical substances have an "optical window" which means that biological tissue has highest physiological transmissivity of light.[92] For example in the application for immunoassay, Aslan *et al* reported surface enhanced fluorescence immunoassay for myoglobin which is a marker for cardiac disease to enhance the limit of detection.[93] The silver island film (SiF) is formed on the glass substrate, which is used as plasmonic nanostructure. The format of immunoassay is sandwich format. Myoglobin was first captured by anti-myoglobin antibodies immobilized on SiFs. Then, the surfaces were incubated with fluorophore-labeled anti-myoglobin antibodies (Fig. 1-13 (a)). It's also important to avoid non-specific adsorption of fluorophore-labeled anti-myoglobin antibodies because enhanced fluorescence is emitted from the non-specific adsorbed fluorophore-labeled anti-

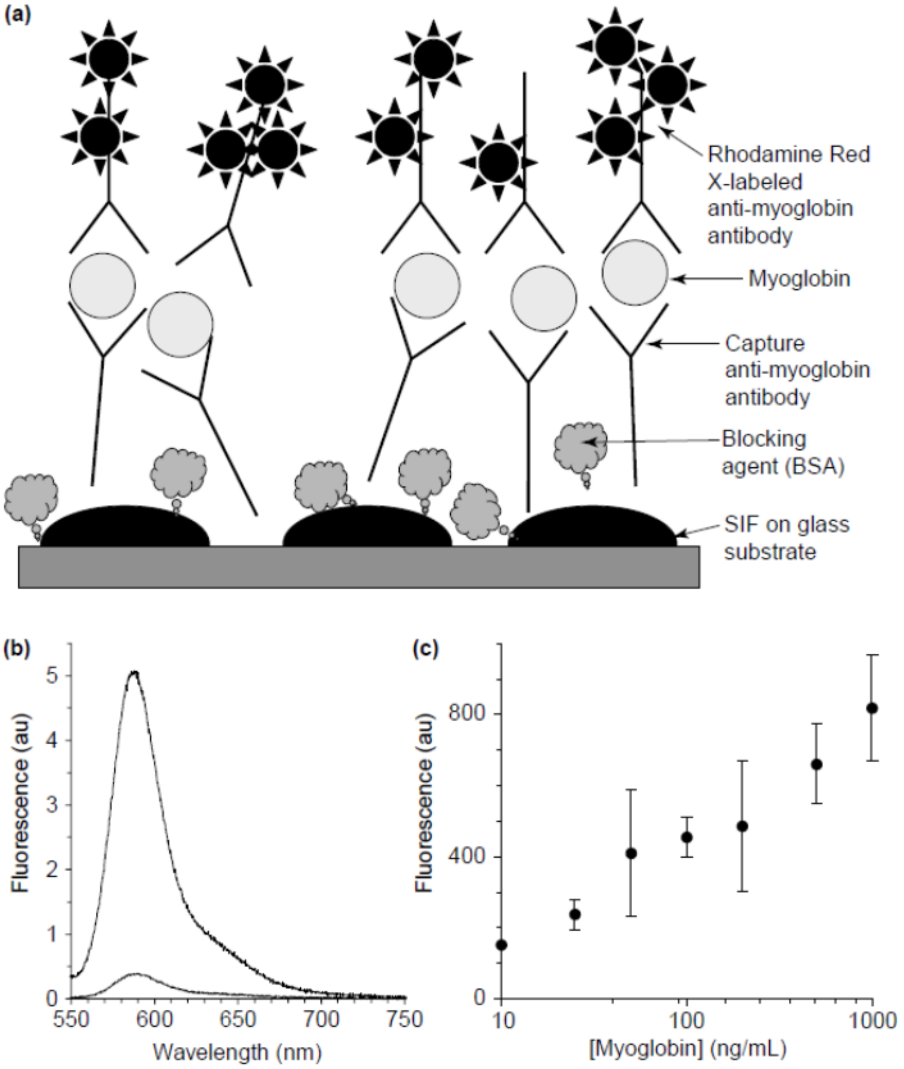

Fig. 1-14 (a) Schematic illustration of surface enhanced fluorescence with sandwich immunoassay for myoglobin on SiFs. (b) Enhanced and normal fluorescence spectra from the Rhodamine Red-X-labeled anti-myoglobin antibody at the 100ng/ml of myoglobin on SiFs and on glass. (c) Myoglobin concentration dependency of fluorescence intensity of Rhodamine Red-X-labeled anti-myoglobin antibody (excitation 532 nm).[93]

myoglobin antibodies, which leads to elevate the blank signal. To suppress the non-specific adsorption in this assay, bovine serum albumin is used as blocking agent. A 10 or 15-fold enhancement of fluorescence was detected from the fluorescent dye-labeled antibody on the SiFs due to plasmonic enhancement effect compared with that on the glass substrate where plasmonic enhancement is not expected (Fig. 1-14 (b)). Fig.1-14(c) shows that the concentration dependence of fluorescent intensity. A range between 10 and 1000 ng/mL is detectable via surface enhanced fluorescence.

For example of the application for the fluorescent enhancement of quantum dots at low absorption wavelength region, Inoue *et al* reported that enhanced photoluminescence from a core/shell nanostructure with a gold nanoparticle as core and silicon quantum dots (Si-QD) as shell was observed in the wavelength range of the LSPRs of Au-NPs.[90] (Fig. 1-15(A)). Fig. 1-15 (B) shows the transmission electron microscopic image of Au-NP/ Si-QDs composite. The Si-QDs agglomerates Fig. 1-25(C) shows a photoluminescence (PL) spectrum of Si-QD itself, a PL excitation spectrum detected at 780nm, and an absorption spectrum of Au-NP. Fig. 1-25(D) shows the excitation wavelength dependence of enhancement factor of PL from Si-QD. Due to the energy band structure of Si, the efficiency of PL excitation is very low above 500 nm due to low efficiency of absorption. However, PL can be enhanced by LSPR and the enhancement has dependence on the thickness of the Si-QD layer on the Au-NP by absorption enhancement (Fig. 1-24(D)).

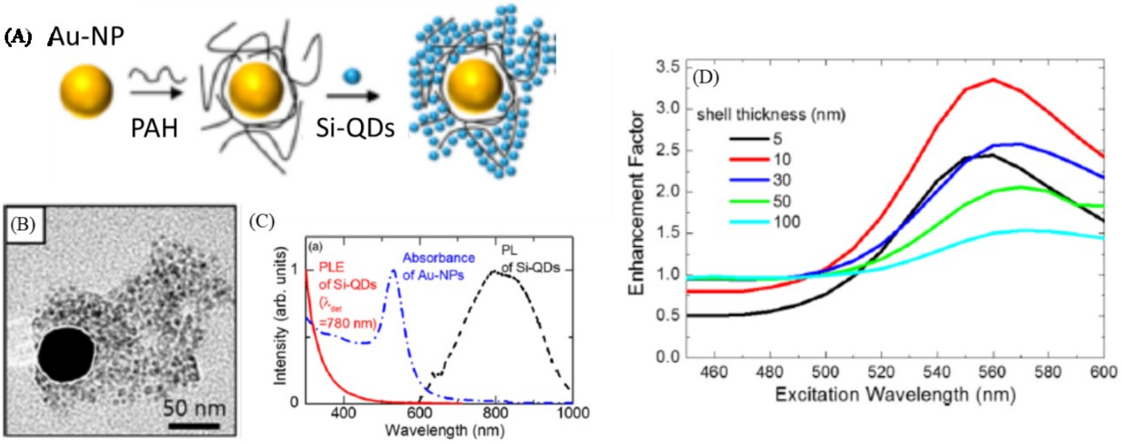

Fig. 1-15 (A) Schematic illustration of Au-NP/Si-QD composite. (B) Transmission electron micrograph of an Au-NP/Si-QD composite. (C) Fluorescence spectrum of Si/QDs in solution excited at 532 nm (black), its excitation spectrum detected at 780 nm (red), and the absorption spectrum of Au-NPs (blue dashed line). (D) Excitation wavelength dependence of enhancement factor at 780nm for different Si-QD shell thicknesses.[90]

The huge enhancement factor of SEF cannot be obtained compared to SERS, but SEF is still powerful technique in the field of immunoassay, fluorescence excitation which efficiency is not so good.

1-4 Electromagnetic simulation

In the field of research of plasmonics, the simulation of electromagnetic field plays important role in designing plasmonic nanostructure, understanding resonance mode. The finite difference time domain (FDTD) method is used for that purpose. In this method, the Maxwell's equation was replaced in set of finite difference equations of electric field and magnetic field as a function of space and time by using Yee lattice.[94] By solving the Maxwell's equations numerically for electromagnetic field in the desired plasmonic nanostructure, it offers us a useful insight into the problems in plasmonics, or electromagnetics generally. Additionally, FDTD can obtain not only the electromagnetic field in space, time solutions but also the frequency solution by taking Fourier transform. Thus, a full range of useful quantities of electromagnetics can be calculated, such as reflection and transmission spectra, field distribution.

In this thesis, we employed a three-dimensional FDTD commercial program 'FDTD solutions' by Lumerical solutions, Inc. to study the optical response of plasmonic nanostructures. All electric fields ($|E|$, $|E|^2$, or $\log_{10}|E|^2$) obtained from the simulation are normalized to the normalized to the incident field unless otherwise stated.

It’s rather useful to obtain information from FDTD calculations such as extinction, absorption, scattering spectra, electric field intensities and distributions, plasmonic mode for designing, predicting, understanding plasmonic properties of the nanostructures.

1-5 Aim and outline of this thesis

For good biosensing devices, there are some important characteristics such as sensitivity, selectivity, low noise, stability and biocompatibility. In these points, important points to be possessed by SERS or SEF sensing devices are high enhancement factor, robustness of SERS substrates, biocompatibility. For the specificity of SEF, surface functionalization with ligands such as antibody is quite important as discussed in 1-3. Moreover, to avoid autofluorescence from bio-related molecules such as proteins, pigments, SERS or SEF should be excited with near infrared (NIR) radiation which less interacts with that kind of molecules. This thesis will focus on development of application of SERS and SEF targeted for biomedical sensing.

As introduced in section 1-1 to 1-4, the background for all subject dealt within this thesis is provided.

Chapter 2 and chapter 3 introduce the plasmonic substrates to get large enhancement in SERS for biomedical sensing applications by tuning plasmonic coupling with gold film. For applying biomedical sensing, it’s quite important to tune the resonance wavelength in near infrared region at aqueous environment to avoid interacting the electric field with bio-related molecules. In chapter 3, we will discuss plasmonic interaction between propagating and localized surface plasmon polaritons to tune the resonance wavelength positon toward getting large enhancement and tuning the plasmon resonance wavelength in water.

Chapter 4 describes the plasmonic substrate development toward *in vivo* biosensor. To implant SERS substrates, there are some problems, because plasmonic substrates suffer from robustness to external forces, i.e., the release of gold nanostructures from the SiO-based support due to external forces, including laser irradiation under aqueous conditions. And biocompatibility of plasmonic substrates is also important. In this chapter, we will focus on the robustness of plasmonic substrates and its biocompatibility.

Chapter 5 focuses on the application of SEF to gain the extremely low limit of detection of fluorescence immunoassay targeted for influenza virus sensing in residential environment sensing. To detect influenza virus in air needs extremely low limit of detection. The characteristics of surface enhanced fluorescence require suppression of non-specific adsorption of the fluorescence probe to the plasmonic structure for high signal-to-noise ratio detection. Moreover the instability of antibody is crucial problem for applying for residential environment because residential environment is severe situation such as temperature, light, humidity, and cost of antibody. So we employed VHH antibody which holds great advantages in terms of large-scale production, ease of genetic modification, and resilience to organic solvents and temperature. We demonstrate successful suppression of non-specific adsorption of the fluorescence probe for high signal-to-noise ratio detection.

Finally, in Chapter 6, the results of this thesis are summarized and presented brief outlook for further study of application of surface enhanced spectroscopy for a biomedical sensing applications.

Chapter 2

Plasmonic interaction between gold nanostructure and gold film for large enhancement of SERS

2-1 Introduction

Strongly enhanced Raman scattering of adsorbates occurs on the surfaces of metallic nanostructures that exhibit LSPR and consequently a local electromagnetic (EM) field enhancement at the wavelength of the Raman excitation. In addition, the chemical interaction between adsorbed molecules and the plasmonic nanostructures may provide an additional enhancement due to the charge transfer effect between the metal and the molecules. These two mechanisms give rise to the surface enhanced Raman scattering (SERS) spectroscopy, which even has single molecule resolution.[12] Although early experiments generally were performed in the visible frequency range, there is increasing interest in SERS-based sensing or imaging in the near-infrared (NIR) optical ranges of 650–900 and 1000–1350 nm, because they are the most appropriate wavelength ranges for SERS experiments in the bovine plasma environment and in vivo detection.[92]

Gold (Au) nanorings have been proposed and demonstrated for NIR SERS application[95,96]. Au nanorings have high tunability in optical properties in the NIR region.[55,96,97] E-beam lithography has been extensively applied to fabricate the nanorings but is limited by a low throughput and high cost.[98–100] As an alternative, one turns to look for some simple, productive, and cheap methods to prepare the nanorings such as nanosphere lithography.[55,96,101] In addition, depositing metallic nanostructures in the vicinity of a metal film has been proved to be an effective way to tune the plasmon resonance and to enhance the local electric field.[102–104] For example, Lévêque et al. have shown the tunability of the plasmon resonance wavelength over 600–900 nm by changing the thickness of silicon dioxide spacer between Au nanosquares and an Au film.[103] Crozier et al.[104] also found that the strong coupling between the propagating and localized surface plasmons with an Au nanodisk array near an Au film separated by silicone dioxide spacer. By coupling propagating and localized surface plasmon, the electric field is quite strongly enhanced. In this section, we use the nanosphere lithography method to fabricate Au nanorings near an Au film on a substrate for the NIR SERS application.

2-2 Materials and methods

Quartz substrates at $\phi 14 \pm 0.02$ mm, t=350μm were purchased from China national scientific instruments and materials (China). 0.098μm (CV=5.4%) surfactant-free white sulfate latex beads was purchased from Interfacial dynamics corporation (United States). The concentration of latex beads is diluted to 0.2% (v/v). Poly diallyl dimethyl ammonium (PDDA) 20wt % in H_2O, which molecular weight is 100,000 – 200,000 as the agent for controlling the surface charge of the substrates was purchased from Sigma-Aldrich (United States). The purchased PDDA solution was diluted to 0.2 %(w/w). 4-aminothiophenol (98%) was purchased from Sigma-Aldrich.

Fig. 2-1(a) and 1(b) show the schematic illustration of Au nanorings on an Au film with a SiO_2 spacer (Au nanorings–SiO_2–Au film) and Au nanorings on a SiO2 substrate, respectively. The Au nanorings–SiO_2–Au film structure was fabricated by performing nanosphere lithography onto a SiO_2 layer which is sputtered onto an Au film. First, a quartz substrate was covered by sputter deposition of an Au film with 50 nm thick and a SiO_2 layer with a variable thickness. Then 98 nm sized sulfate latex particles were deposited on the functionalized SiO_2 surface by 0.2% (w/w) PDDA solution for 30 seconds for the electrostatic self-assembly of beads. After deposition of latex beads, Au layer was sputtered for 30 nm thick on the top of the beads deposited substrate[101]. Next, a xenon (Xe) ion milling process by in-house made ion milling system (Fig.2-2) was performed on the Au film to form the Au nanoring structure by etching away the excess gold. The detailed working mechanism is shown in previous work of our group[105]. For an ion beam with stable and constant intensity, the milling rate is constant. So the milling depth should be determined by the ion milling time. In this experiment, repeating 3 times of 20s milling, 20s cooling, and 5s milling at last. After ion milling process, an oxygen plasma treatment (100W, 5 minutes) was used to remove the remains of the latex particles. Fig. 2-1(c) displays that the nanorings (around 130 nm in diameter) are distributed randomly with a constant density onto the SiO_2 surface and are isolated with an interstructure spacing of around 200 nm. The maximum area of a single continuous nanoring domain can reach a few square centimeters after optimization.

Furthermore, a cross-section electron micrograph (bottom part in Fig. 2-1(c)) shows the smooth and flat Au and SiO_2 film under the nanorings and all free standing Au nanorings possess sharp edges and opened surface morphology, which is favorable for SERS. For a comparison, nominally identical Au nanorings were fabricated directly onto the quartz substrate without an Au film and a SiO_2 film underneath (Fig.2-1(d)).

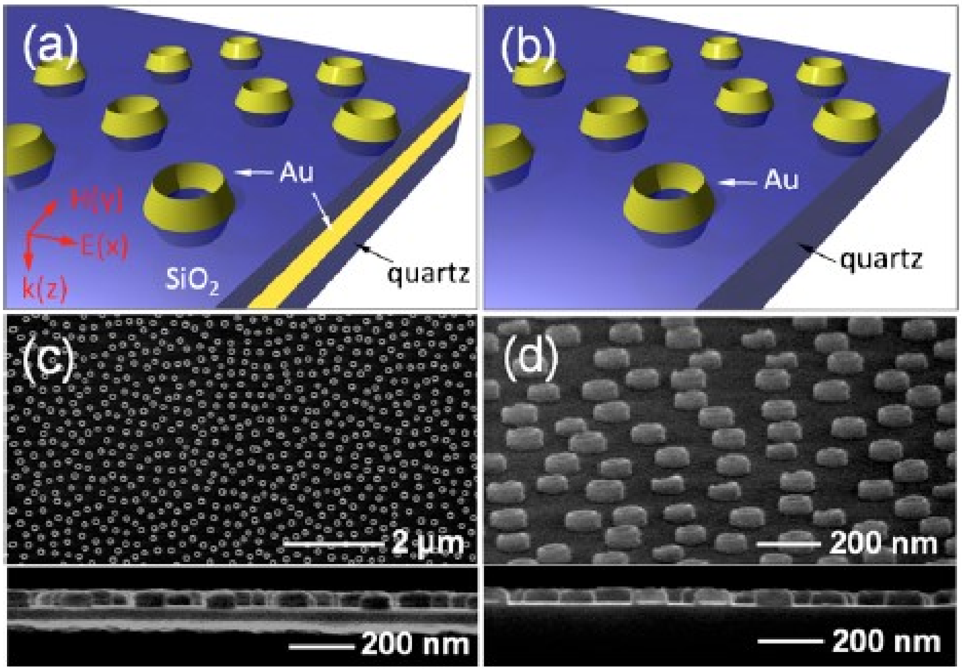

Fig. 2-1 Schematic illustrations of (a) Au nanorings – SiO$_2$ *– Au film and (b) Au nanorings on quartz substrate and their corresponding electrom micrographs in (c) and (d), respectively. Bottom parts in (c) and (d) panels are the cross-section images.*

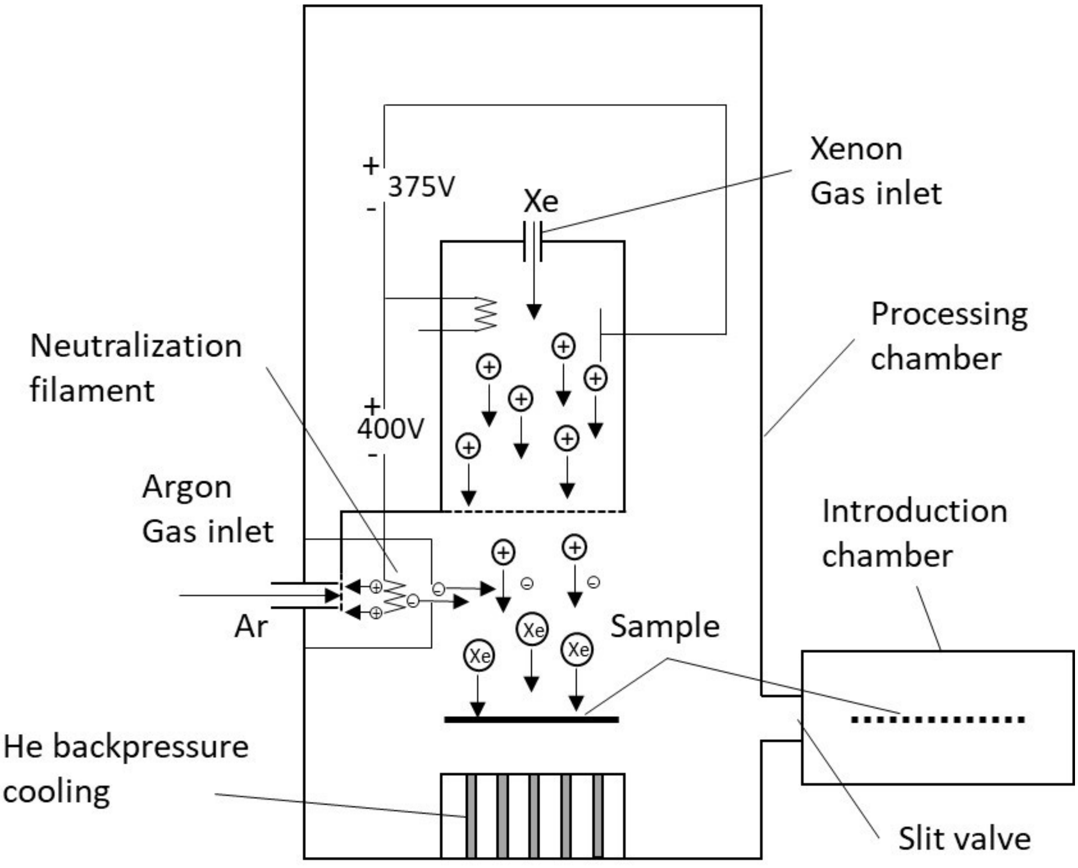

Fig. 2-2 In-house made ion milling system

2-3 Results and discussion

To investigate the optical properties of the Au nanorings–SiO_2–Au film structure, simulated and experimental reflection spectra are analyzed in Fig. 2-3. Numerical simulations for analyzing the plasmonic characteristics were performed by a FDTD method.[106–108] The structure was illuminated by normal incident light which the polarization state is along the x-direction (Fig. 2-1(a)). The empirical dielectric functions of Au and SiO_2 have been described in colleague's work.[109] For the sake of simplicity, we assumed periodic boundaries although the structures are randomly distributed in our samples. We have observed some periodicity induced effects, which we will discuss later, but in general there is good agreement with the experimental results. Experimental spectra were recorded by a Bruker spectrometer (Vertex 80 V) with a Hyperion 2000 microscope.

Fig. 2-3(a) (top) presents the simulated reflection spectra of the Au nanorings–SiO2–Au film structures with different thicknesses of the SiO_2 spacer. We can observe a strong reflectance dip in the NIR range for all structures, which is attributed to the coupling and the plasmon hybridization between the localized surface plasmon (LSP) of nanorings and the delocalized surface plasmon (DSP) of the Au film. With the decrease in the SiO_2 spacer thickness from 70 to 10 nm, the dip shifts to longer wavelengths and becomes narrower. The transmission spectrum of Au nanorings onto the quartz

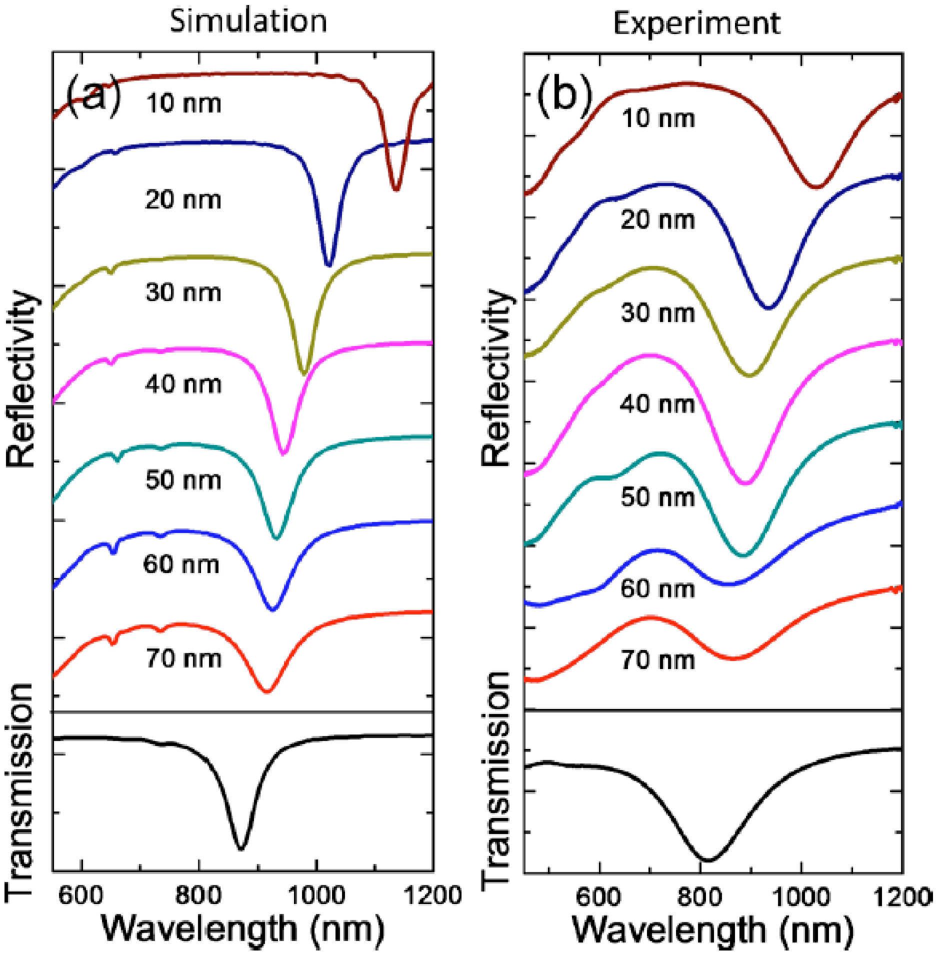

Fig. 2-3 (a) Simulated and (b) experimental reflection spectra of Au nanorings- SiO2-Au film with different thicknesses of the SiO2 layer (top) and transmission spectra of Au nanoring on quartz substrate (bottom).

substrate is shown in Fig. 2-3(a) (bottom) for comparison, where only a LSP peak of nanorings at a shorter wavelength (872 nm) is observed. To better understand the nature of the dip's shift and narrowing, the electric field enhancement (EFE, $\log|E/E_0|^2$) and charge distribution were simulated and are depicted in Fig. 2-4. It is apparent that a bonding dipolar LSP is excited in nanorings without Au film (Fig. 2-4(a))[101]. At the 50 nm thick of SiO_2 spacer which separates Au nanorings and the Au film (Fig. 2-4(b)), the strong coupling dipolar LSPR of nanorings and its own image charges on the Au film ocuurs, which generates a quadrupole-like resonance. The coupling leads to a maximum EFE that is almost three times larger compared to the bare nanorings. More importantly, this enhancement is spread over the nanoring's surface, which is particularly useful for SERS-based molecular detection. When the thickness of SiO_2 is decreased to 10 nm (Fig. 2-4(c)), the electric field confinement due to strong coupling occurs mostly in the SiO_2 spacer, which reduces the total dipole moment and radiative scattering of the nanostructure significantly as a result. By doing so, a better confinement of optical energy in the nanostructure and a higher quality factor in resonance bandwidth can be obtained. This is why the LSPR wavelength was red-shifted and the linewidth of the reflectance dip got narrowed. The latter is potentially helpful to improve the figure of merit for LSP resonance biosensing.[59] The enhanced tunability of the resonance by changing the spacer thickness also helps us to match the wavelength of the nanostructure's resonance to the laser excitation. In addition, we have observed some small dips in the range of 600–800 nm for the Au nanorings–SiO_2–Au film structure,

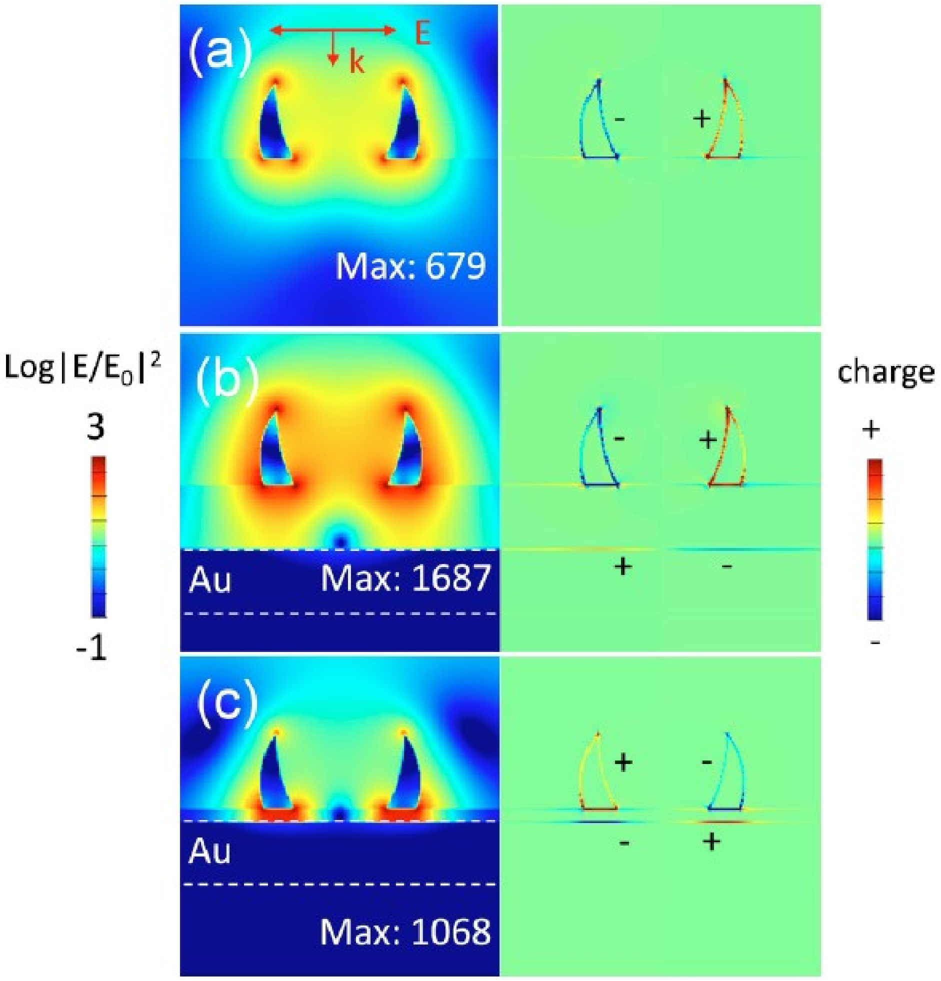

Fig. 2-4 (Left) EFE (log|E/E0|2) and (right) charge distribution of (a) Au nanorings and Au nanorings –SiO2-Au film with (b) 50nm and (c) 10nm SiO2 layer at resonance wavelengths of 872nm, 932nm, and 1138nm, respectively. Dashed line in (b) and (c) panels indicate the position of the 50 nm thick of Au film. The maximum value of EFE (|E/E0|2) of each structure shown in [(a)-(c)].

which is caused by the grating-induced excitation of DSPs at the Au film[110]. All experimental spectra qualitatively reproduce the simulated spectra except for a broader linewidth of the plasmon resonance probably induced by inhomogeneous broadening in the sample and the absence of small grating-induced dips in the visible range due to the disordered structure [Fig. 2-3(b)].

We employed 4-aminothiophenol (4-ATP) as a Raman probe to evaluate the SERS performance of the Au nanorings–SiO_2–Au film structure. Raman spectra were collected by a Horiba Jobin Yvon LabRam HR 800 system with a 100 objective and a 785 nm diode laser (0.8 mW). A monolayer of 4-ATP molecules was adsorbed onto the nanorings surface by soaking in a 0.3 mM ethanol solution overnight. Figure 2-5 shows the SERS spectra of 4-ATP on the Au nanorings and on the Au nanorings–SiO2–Au film with different thicknesses of the SiO2 layer. Although the Raman signal amplitudes vary, all spectra have the same shape with the Raman shifts at 1080, 1143, 1179, 1436, and 1589 cm^{-1}, which correspond to the vibration modes of νCS 7a(a1), δCH 9a(b2), δCH 9a(a1), νCC +δCH 19b(b2), and νCC 8a(a1), respectively.[111,112] The average EF of 4-ATP on the Au nanorings was calculated to be 2.6×10^5 by using the Raman band at 1080 cm^{-1} according to the method of Wang[113]. Obviously, the EF gets improved when the 4-ATP molecules are absorbed on the Au nanorings–SiO_2–Au film structure. In particular, the EF is increased when the SiO_2 spacer becomes thicker and reaches the maximum value of 1.4×10^7 with a 50 nm in thickness then decreases again when the

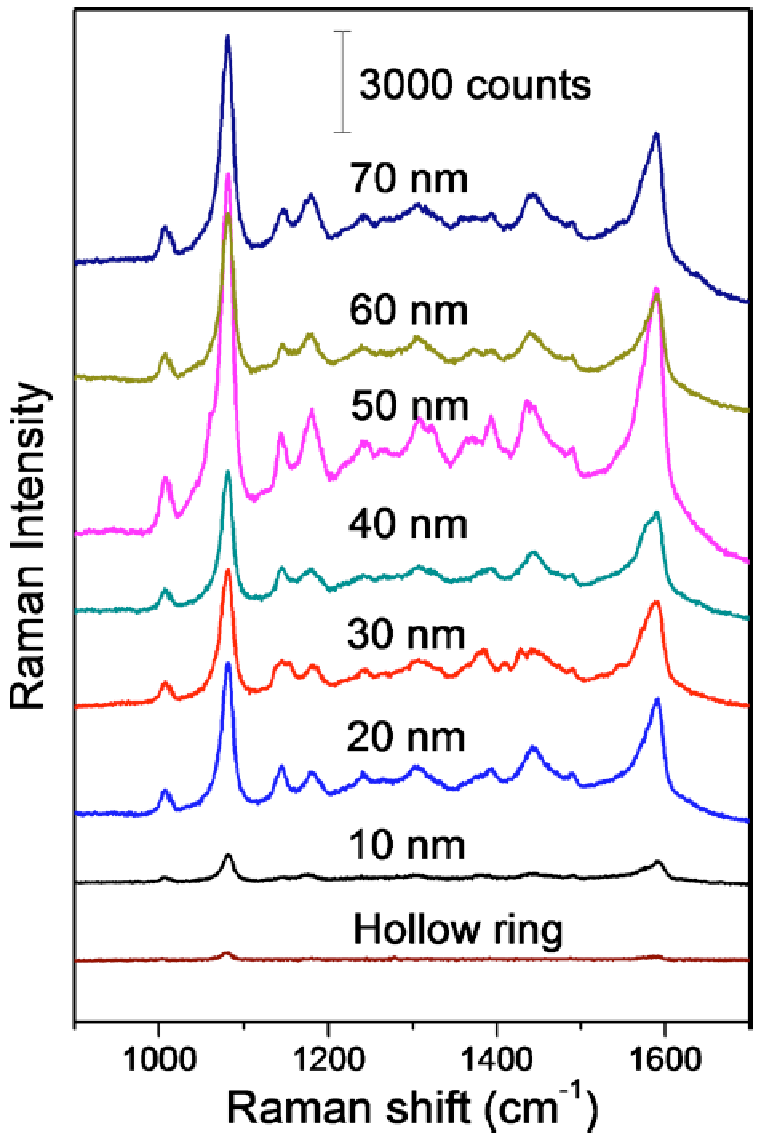

Fig. 2-5 SERS spectra of 4-ATP molecules on Au nanorings (bottom) and Au nanorings-SiO_2-Au film with the thickness of SiO_2 layer from 10 to 70 nm.

thickness is larger than 50 nm. We strongly believe that the improved SERS effect on the Au nanorings–SiO_2–Au film structure is caused by the EM mechanism due to the strong coupling of the LSP of the Au nanorings and the DSP of the Au film. When the Au nanorings and the Au film are separated with a small gap, e.g., 10 nm, the SERS EF is only slightly increased because the structural resonance wavelength (1070 nm) is far away from the laser excitation wavelength (785 nm) and the most of the enhanced electric field is confined in SiO_2 spacer, which is difficult to access by the molecules. When the gap becomes larger, e.g., 50 nm, the EF is further improved because the electric field is less confined and becomes much easily accessible by the molecules. More importantly, the largely blue-shifted structural resonance wavelength (914 nm) is closer to the laser excitation wavelength, which leads to a stronger electric field. However, the EF will decrease when the gap is larger than 50 nm due to a weaker plasmon coupling effect.

2-4 Conclusion

In conclusion, we have demonstrated the fabrication of the Au nanorings–SiO2–Au film structures by using nanosphere lithography technique. An enhanced tunability and high quality value of plasmon resonances of Au nanorings have been demonstrated by controlling the coupling LSP and DSP by changing the thickness of the SiO_2 spacer. Moreover, we have achieved a maximum NIR SERS EF as large as 1.4×10^7, an improvement with a factor of 50 times compared to the Au nanorings. We believe the

Au nanorings–SiO_2–Au film structure has a promising commercial prospect for SERS substrates due to a simple, low cost and high throughput manufacturing method, and a large EF.

Chapter 3

Plasmonic interaction between propagating and localized surface plasmon resonance in water for biomedical and environmental applications

3-1 Introduction

Strongly enhanced Raman scattering of adsorbates occurs on the surfaces of metallic nanostructures that exhibit LSPR and consequently a local electromagnetic (EM) field enhancement at the wavelength of the Raman excitation. SERS has received considerable attentions in recent years because of its high sensitivity down to the single-molecule detection limit in specific molecules[12,114,115]. The enhancement mainly arises from enhanced local electromagnetic (EM) fields due to surface plasmon resonances[7]. Additionally, chemical interactions between adsorbed molecules and metallic nanostructures may provide an additional enhancement due to charge transfer between metal and molecules. Because of its high sensitivity, SERS is a promising powerful tool for biomedical and environmental sensing, e.g., blood glucose detection[68], virus detection[116], arsenic detection in contaminated water[117], and the detection of chemical pollutants in sea-water such as polycyclic aromatic hydrocarbon.[118]

The enhancement factor (EF) of SERS depends on EM-field intensities at excitation and Raman band wavelengths[7,119]. To maximize EFs, EM-field intensities at both excitation and Raman band wavelengths should be strongly enhanced. A double-resonance substrate has been proposed and demonstrated as one of the most promising structures to achieve maximized intensities at both excitation and Raman wavelengths[110,120–123]. In general, a double-resonance substrate consists of an array of gold (Au) nanostructures or nano-disks and a continuous gold film separated by a dielectric spacer. SPPs and LSPs are strongly coupled and two hybridized modes are observed[122]. By tuning the structural parameters, a double-resonance substrate provides a SERS EF of 8.4×10^8 in air for a silver arrays and 7.2×10^7 in Au nano-disk arrays[122]. For biomedical and environmental applications of SERS, excitations in the near infrared (NIR) region are suitable because of the smallness of the interaction of NIR light with biological media[68,107,123]. In many applications, e.g., in-situ detection of biomolecules[124,125], blood glucose measurements[126], pharmaceutical chemicals detection in water[127], and aromatic chemical detection in sea water[128], SERS is measured in water.

In this section, we first calculate the electric field for Au nano-disk arrays placed in water, by a FDTD method to define the grating constant of the nano-disks array to excite SPPs in water and to tune the diameter of Au nano-disks for controlling the LSP resonance wavelength by taking into account the refractive index of water. From calculation results, we fabricated double-resonance substrates using electron beam lithography (EBL). We show that tuning of the interaction between SPPs and LSPs by controlling the pitch of the Au nano-disk in the directions parallel and perpendicular to the polarization of the excitation light results in an EF as large as 7.8×10^7 in the NIR region in water.

3-2 Materials, experimental and simulation methods

For the fabrication of double resonance plasmonic substrates, EBL was employed. Polymethyl methacrylate (PMMA) resist of which average molecular weight was 950,000 was used. The mixture of the same amount of methyl isobutyl ketone and 2-propanol was used as a developer for the PMMA after irradiation of electron beam. 1-propanol was used as a rinsing agent for the developer. A conductive water soluble polymer espacer 300 (Showa Denko, Japan) was used for charge-dissipating agent for electron beam lithography. Quartz substrates at $\phi 14 \pm 0.02$ mm, t=350μm were purchased from China national scientific instruments and materials (China).

Fig. 3-1(a) shows a schematic illustration of a double-resonance substrate. An Au nano-disk array is formed on a Au film with a SiO_2 spacer. A thin titanium (Ti) film between the Au film and a quartz substrate serves as adhesion layer. For the preparation of the structure, a quartz substrate was cleaned in a sulfuric acid/hydrogen peroxide solution (H_2SO4 (96%):H_2O_2 (30%)=3:1) for 15 minutes followed by an oxygen plasma treatment. Ti(10 nm), Au(100 nm), and silicon dioxide (SiO_2) (30 nm) layers were sputtered onto the cleaned substrate. A 200 nm polymethyl methacrylate (PMMA) resist layer was then spin-coated onto the substrate and baked at 165°C for 30 minutes. After

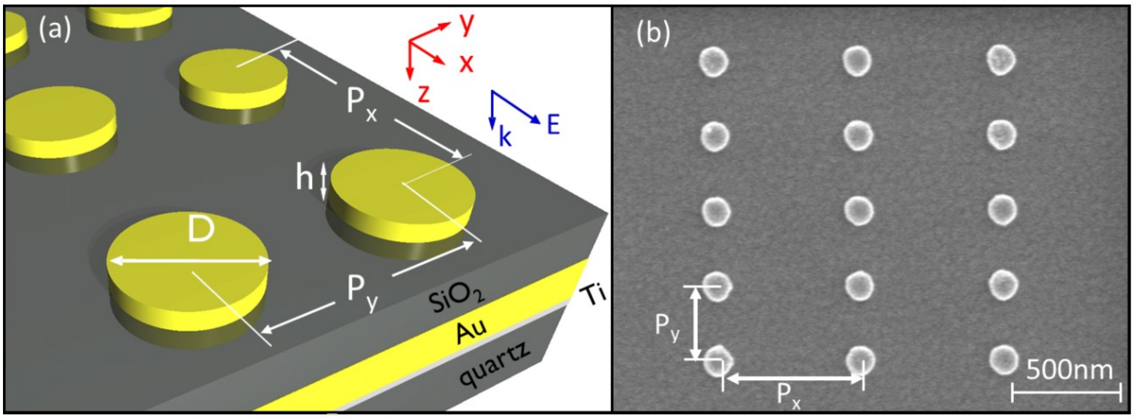

Fig. 3-1 (a) Schematic illustration of double-resonance gold nanodisks array substrate. (b) Scanning electron micrograph of a fabricated gold nanodisk array

baking PMMA resist, espacer 300 was spin-coated, followed by 10 minutes baking at 95°C. Each nanodisk arrays were exposed by electron beam lithography at different dose of electron to control the diameter of nanodisks. Development of the PMMA was done by soaking in developer for 1 minute at 22°C, resulted in the formation of nanohole arrays in the PMMA layer. Au (30 nm) was then deposited by evaporation to form nanodisks inside the holes. Finally, the PMMA layer was lifted off in acetone at 50°C. Fig. 3-1(b) shows a scanning electron microscope image of an Au nanodisk array. The overall size of the gold nanodisk array is 100×100 μm [Fig. 3-1 (b)].

The optical response of the structure was calculated by a FDTD method (FDTD solutions, Lumerical Solutions, Inc. Vancouver, Canada). A metallic nanodisk array was illuminated with a plane wave at normal incidence, which propagates in the k-direction

[Fig. 3-1(a)]. The electric field E was directed along the x-direction; see Fig. 3-1(a). Periodic boundary condition was used. The simulation region was $P_x \times P_y \times 1920$ nm^3 with a non-uniform mesh, where P_x and P_y were the nanodisk pitches in x- and y-directions, respectively, in Fig. 3-1(a). For fine simulations around the nanodisks, 200×200×1920 nm^3 regions were calculated with a mesh size of 2 nm. The thickness of the quartz substrate was set to 2000 nm, and those of the SiO2, Ti, and Au films were 30, 10, and 100 nm, respectively. The height of the Au nano-disk was 30 nm. P_x and P_y were changed from 540 to 630 nm and from 200 to 400 nm, respectively. The refractive index of the background was set to 1.33 (water) and those of other materials were obtained by fitting the empirical Au[129], SiO2[130], and Ti[131] dispersion data with Lumerical's multi-coefficient model[132].

3-3 Results and discussion

To measure the reflectance and SERS in water, the double-resonance substrates were mounted in a home-made flow cell with a 1-mm-thick cavity. Water was sent into the cell by a peristaltic pump. For reflectance measurements, 10× objective (numerical aperture (NA): 0.2) was used for irradiation and detection. The polarization of the incident light was set parallel to the x-direction in Fig. 3-1(a). An area without nano-disks, i.e., a SiO2-coated Au film, was used as a reference. For SERS measurements, 4-aminothiophenol (4-ATP) was employed as a Raman probe. A monolayer of 4-ATP molecules was adsorbed onto nanodisks by soaking in a 1mM ethanol solution overnight. Raman spectra were excited via 10× objective (NA=0.2) using a 785-nm diode laser (2.5 mW) and recorded by a LabRam HR 800 spectrometer (Horiba Jobin Yvon). Raman peaks in the 600-1800-cm^{-1} region, corresponding to wavelengths 824-915 nm, were studied.

Fig. 3-2(a) presents a contour plot of calculated reflectance as a function of P_x and the wavelength. P_y and the nano-disk diameter are set to 300 nm and 130 nm, respectively. Two modes corresponding to SPP and LSP can be seen. SPP shifts to shorter wavelengths as P_x decreases. This occurs as a result of the matching of wave vectors for light and SPP (k_{spp}). In the double-resonance structure, k_{spp} is inversely proportional to P_x, specifically $2\pi/P_x$[133]. Fig. 3-2(a) indicates that the largest enhancement of the excitation field (785 nm) in water is achieved when P_x is 580 nm. Similar data when P_y is changed is shown in Fig. 3-2(b). P_x and the nano-disk diameter are set to 580 nm and 130 nm, respectively. The SPP resonant wavelength is almost independent of P_y, whereas that of the LSP moves to longer wavelength and becomes broader as P_y decreases. This is because of the coupling between neighboring nano-disks in the y-direction, and resultant damping of the LSP resonance. [26]

Fig.3-2(c) shows a contour plot of calculated reflectance in water as a function of diameter (80-145 nm) and the wavelength. P_x and P_y are set to 580 nm and 300 nm, respectively. The anti-crossing behavior is clearly seen[121]. Fig. 3-2(d) shows

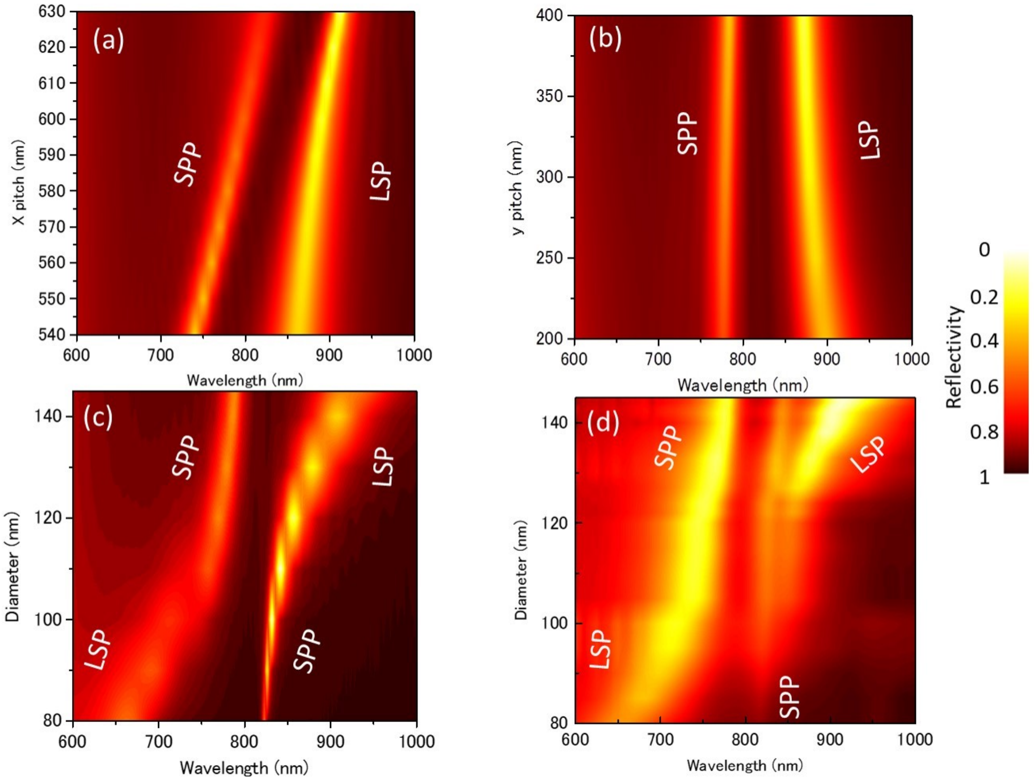

Fig. 3-2 Contour plots of calculated reflectance as functions of (a) P_x and wavelength (P_y= 300 nm, diameter= 130 nm), (b) P_y and wavelength (P_x= 580 nm, diameter= 130 nm), (c) diameter and wavelength (P_x= 580 nm, P_y= 300 nm). (d) Contour plot of experimentally obtained reflectance as a function of diameter and wavelength (P_x= 580 nm, P_y= 300 nm).

experimentally obtained reflectance for the structure in Fig. 3-1(b). The experimental and calculated results agree very well except for a small reflection dip around 820 nm in the experimental data. This is caused by a SPP grating mode excited by z-polarization of the nano-disk illuminated under angled incident light[121]. A slight broadening of the experimental data compared with calculated values is also caused by this angled illumination[122]. The overall agreement between experimental and calculated results indicates that the double-resonance structure has been fabricated as designed with high accuracy.

Fig. 3-3(a) and (b) presents cross-sectional images of the electric field distribution at 785 and 879 nm, respectively. For the calculation, P_x and P_y are set to 580 and 300 nm, respectively, and the diameter and height of a nano-disk to 130 and 30 nm, respectively. For both resonances, the electric field is significantly enhanced near the Au nano-disk. Furthermore, over the nano-disk, a large extensive evanescent field, which is a characteristic of SPP, is observed in Fig. 3-3(a).[121]

Fig. 3-3(c) shows a contour plot of the electric field intensity at the position 2 nm above and 1nm away from the edge of Au nanodisk (inset) as a function of P_y and the diameter. The electric field at the SPP resonance wavelength (~785 nm) and the LSP resonance one (~880 nm) is strongly enhanced especially when P_y is relatively large. When P_y is relatively small, e.g., smaller than ~300 nm, the field enhancement becomes small. This arises from the coupling between neighboring nanodisks, which leads to damping of surface plasmon resonances[134]. Fig. 3-4(a) shows SERS spectra of 4-ATP

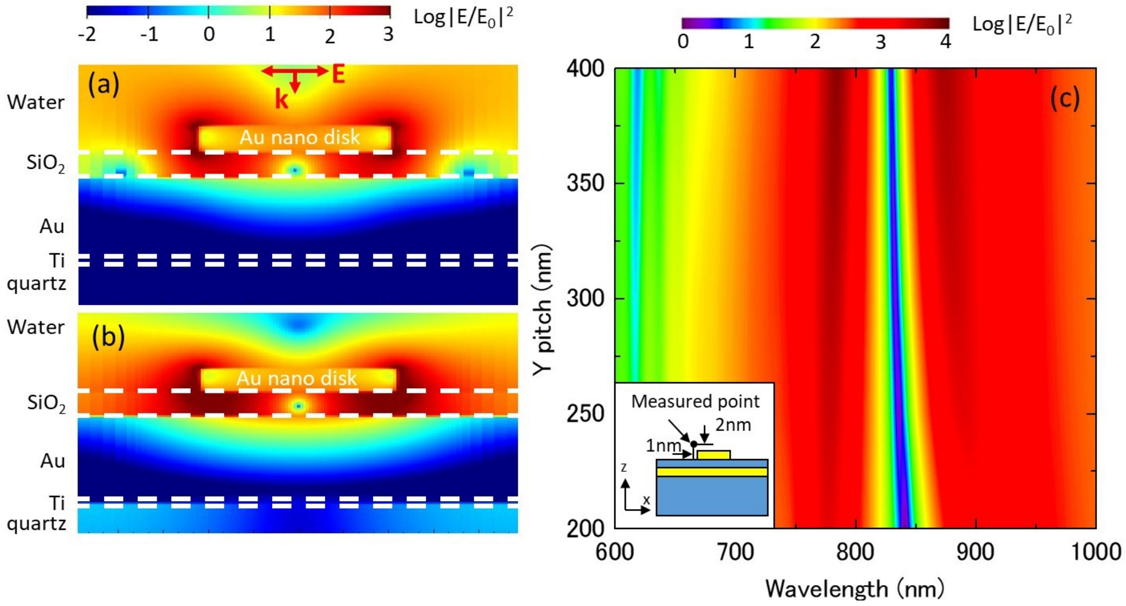

Fig. 3-3 Simulated electric field distributions for the structure with P_x= 580 nm, P_y= 300 nm, and d= 130 nm at (a) 785 nm (SPP resonance), (b) 879 nm (LSP resonance). (c) Contour plot of electric field intensity as functions of P_y and wavelength (P_x= 580 nm)

on the double-resonance substrates with P_x=580 nm and P_y=300 nm (upper part). The nano-disk diameter is changed from 100 nm to 143 nm. For comparison, a normal Raman spectrum of 100-μm-thick 4-ATP formed by melting by heat and re-crystallizing by cooling is shown at the bottom. The Raman signals at 1004, 1081, 1140, 1178, 1439, 1490, and 1589 cm^{-1} correspond to the vibration modes of γCC+γCCC 18a(a1), νCS 7a(a1), δCH 9b(b2), δCH 9a(a1), νCC+νCH 19b(b2), ν(CC) + δ(CH), and ν(CC) at, respectively. The Raman signals are strongly enhanced on the double-resonance substrates. As the diameter of nano-disks increases, the Raman signal at 1589 cm−1 with respect to that at 1080 cm−1 increases. This can be explained by the red-shift of the LSP resonance as diameter increases, as can be seen in the reflectance spectra in Fig. 3-4(b). The Raman signal at 1080cm−1 is strongest when the diameter is 130 nm, arising through the almost exact coincidence of SPP and LSP resonance wavelengths with the excitation and Raman wavelengths.

In Fig. 3-4(c), SERS spectra when P_y is changed from 300 nm to 580 nm and P_x and the diameter are fixed to 580 nm and 130 nm, respectively, are presented. The reflectance spectra of the same samples are shown in Fig. 3-4(d). The SERS signals monotonically increase with decreasing P_y, which is accompanied by a deepening in the reflectance dip in Fig. 3-4(d). These results indicate that the energy of the incident light is more effectively confined when P_y is smaller. However, this is not consistent with the result of the electric field simulation in Fig. 3-3(c). In the simulation, the field enhancement is the largest when P_y is 580 nm and decreases as P_y decreases. Since

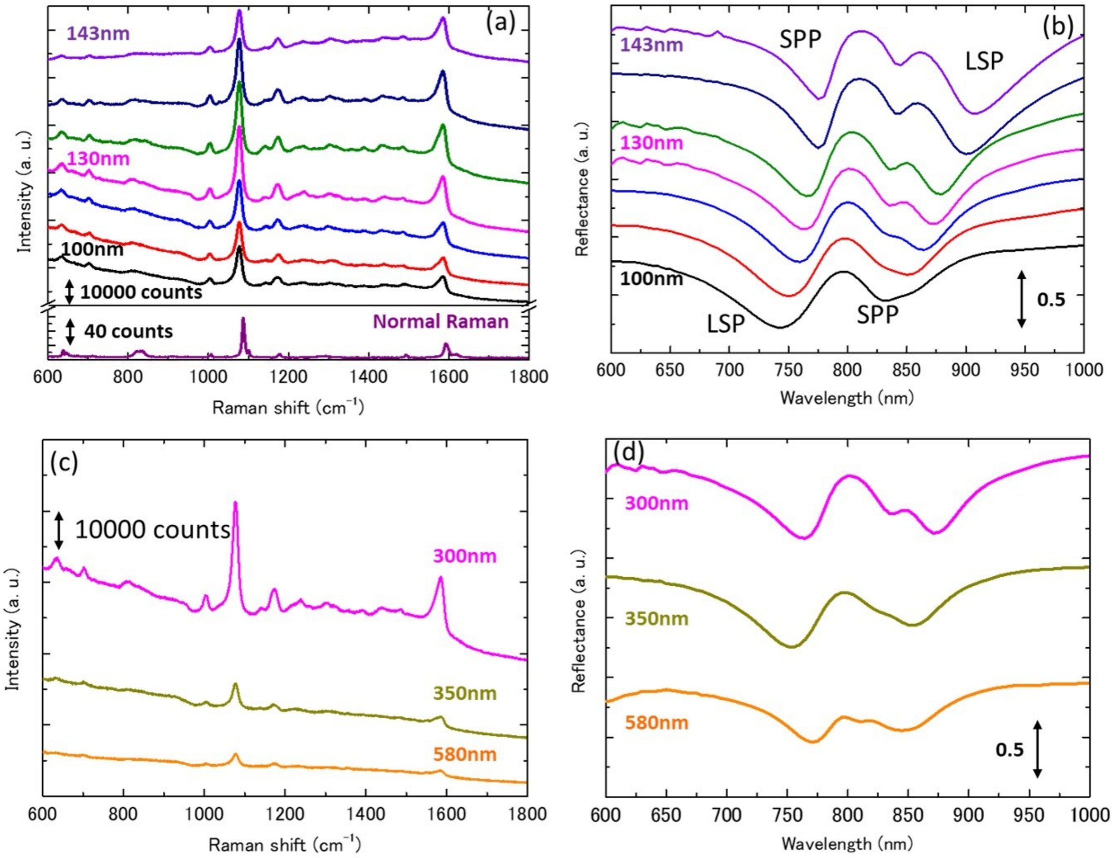

Fig. 3-4 (a) (Top panel) SERS spectra of 4-ATP on double-resonance nanodisk array substrates (Px= 580 nm and Py= 300 nm). For the spectra, the diameter changes from 100 to 143 nm. (bottle panel) Normal Raman spectrum of 100 mm thick 4-ATP film. (b) Reflectance spectra corresponding to (a). (c) SERS spectra as Pf changes from 300 nm to 580 nm (Px= 580 nm and diameter = 130 nm). (d) Reflectance spectra corresponding (c).

SERS EF is considered to be proportional to the EF of the electric fields at the excitation and Raman wavelengths[7,119], the simulation suggests the largest Raman EF when P_y is 580 nm. The reason for the discrepancy is not very clear at present, but may be caused by slightly different parameters between simulation and experiment[135], e.g., incident angle and imperfection of the structure.

The SERS EF averaged over a laser spot is defined as $EF=(I_{SERS}/N_{SERS})/(I_{NR}/N_{NR})$, where I_{SERS} and I_{NR} are the intensities of SERS and normal Raman scattering at a specific Raman band, N_{SERS} and N_{NR} are the number of molecules in the laser spot for SERS and normal Raman scattering, respectively[7]. In the present structure, N_{SERS} is calculated as $N_{SERS}=\rho_s S_{gold}A/(P_x \times P_y)$, where ρ_s is the surface packing density of 4-ATP, S_{gold} is the surface area of one gold nanodisk and A is the laser spot area[121]. N_{NR} is calculated using the volume density and molecular weight of 4-ATP and the laser illumination volume which is defined by the laser spot size and the penetration depth of the spot[113]. The volume density, molecular weight, and surface packing density is 1180 kg/m^3, 125.19, and 5×10^{14}/m^2,[113] respectively. The average EF obtained for the optimized double-resonance substrate (P_x: 580 nm, P_y: 300 nm, diameter: 130 nm) in water is 7.8×10^7. This value is among the highest in SERS substrates intended for use in biomedical and environmental applications.[136]

3-4 Conclusion

In conclusion, through FDTD simulations and experiments, we have studied optimizing conditions to enhance responses of a double-resonance nano-disk array for NIR SERS in water. We showed high tunability of the SPP and LSP resonance wavelengths by changing the pitch and diameter of Au nano-disks. By the optimization of the SPP and LSP resonance wavelengths, a maximum averaged NIR SERS EF of 7.8×10^7 can be achieved in water. We believe that SERS substrates of double-resonance nanodisk arrays can be used in biomedical or environmental applications that require SERS measurements in water in the NIR region.

Chapter 4

SERS substrates for *in vivo* application

4-1 Introductions

Plasmonic nanostructures markedly increase the Raman scattering intensity of molecules adsorbed on their surfaces. This phenomenon is known as surface-enhanced Raman scattering (SERS), which can achieve a single-molecule resolution[7,137]. SERS is based on electromagnetic field enhancement and results from the excitation of a localized surface plasmon resonance in a nanostructure. The chemical interaction between adsorbed molecules and a metallic nanostructure may provide an additional enhancement because of charge transfer between metal and molecules[7]. The high sensitivity and selectivity of SERS lend itself to biosensing applications, including in vivo sensing on animal models using of SERS substrates[138–140].

To improve the sensitivity and control of SERS for specific applications, precisely controlled gold nanostructure arrays have been formed on SiO_2-coated gold mirrors[107,122,141]. SERS substrates suffer from robustness to external forces, i.e., the release of gold nanostructures from the SiO-based support due to external forces, including laser irradiation under aqueous conditions [Fig. 3(b)]. This is because these nanostructures do not adhere well to the SiO_2 substrate. Ti and Cr are traditional adhesion materials that provide good mechanical adhesion between gold and SiO_2. They are compatible with evaporation processes, but often limit the plasmonic sensor performance by damping the plasmon mode[142,143].

Alternative adhesive materials include organic silanes, such as mercaptosilane. Lamy de la Chappelle et al. introduced a mercaptosilane layer to a lithographic lift-off process to provide an adhesive layer between SiO_2 and gold[144]. The mercaptosilane layer improved the mechanical adhesion of gold nanodisks and did not adversely affect the SERS performance, in contrast to Cr adhesive layers. However, the increased adhesion provided by this process is limited, because the gold plasmonic layer is deposited after the patterning of the mercaptosilane layer. Hence, the mercaptosilane coating is exposed to several wet processing steps, deteriorating its adhesive properties.

In this article, we report the fabrication of a nanopatterned gold film on SiO_2, including a (3-mercaptopropyl)triethoxysilane (MPTES) adhesion coating between SiO2 and the gold. In contrast to the report of Lamy de la Chapelle et al.[144] , fabrication of nanostructure is achieved using an etching process. In this manner, the gold film is deposited on a fresh mercaptosilane coating, resulting in a superior adhesion strength, without compromising SERS performance. The substrate is sufficiently robust for in vivo sensing, as successfully demonstrated by its implantation in the animal skin for 2 months.

4-2 Materials and methods

SERS substrate fabrication

Fig. 4-1(a) shows the SERS substrate fabrication process. The nanopatterned top gold film on a MPTES coating was fabricated by electron beam lithography (EBL) and subsequent etching. A 100-nm-thick gold film, i.e., an internal mirror, was deposited on a quartz substrate by sputtering a 10-nm-thick titanium adhesion layer. A 30-nm-thick SiO2 spacer was deposited on top of the gold film by sputtering. The silanization of the SiO2 top layer was carried out according to Ye et al.[107] The substrate was immersed in a solution of 10% (v/v) MPTES in 95:5 ethanol/distilled water for various durations. The substrate was then carefully rinsed with ethanol, dried under N_2, and baked in an oven at 105 °C under N_2 flow for 10 min.

Within 30 min after silanization, a 30-nm-thick gold layer was deposited on the MPTES-functionalized substrate by sputtering. This short time frame was required to prevent carbon contamination of the substrate surface by air, and thus achieve a high gold adhesion strength. Subsequently, the film was coated with a thin negative electron beam resist (Micro Resist Technology, ma-N 2400) and exposed by EBL.

After the development of the resist, Xe ion milling of the gold film was carried out. The substrate was cleaned by oxygen plasma treatment, yielding gold nanodisks on the

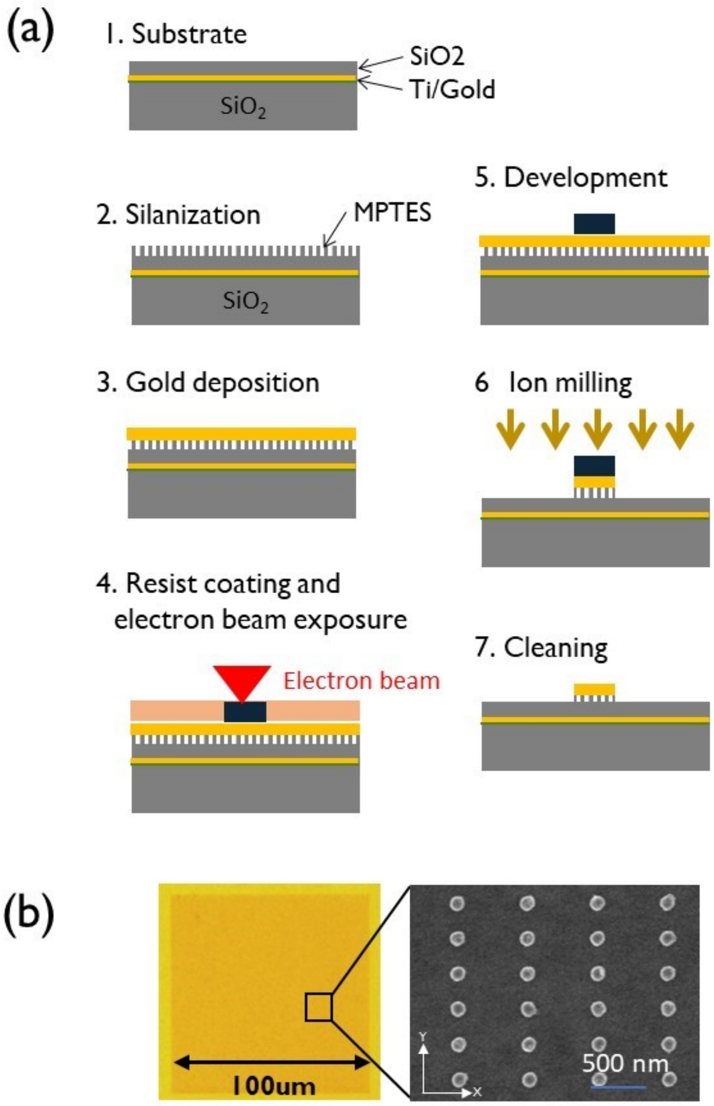

Fig. 4-1(a) EBL preparation of the MPTES-containing SERS substrate. (b) Bright- field microscopy (left) and SEM (right) images of gold nanodisks deposited on the MPTES-containing substrate by EBL.

MPTES-functionalized substrate [Fig. 4-1(b)]. For comparison, substrates containing gold nanodisks deposited on a 2-nm-thick Ti film (instead of MPTES) and gold nanodisks deposited without any adhesion layer were also fabricated. The distances between two gold nanodisks were 590 and 300 nm in the x- and y-directions, respectively. The total area of the gold disc array was 100×100 μm^2.

Adhesion test

Adhesion tests were performed using a scratch testing tool (Rhesca, CSR-2000 Nano-layer scratch tester) enabling the calculation of the adhesion strength of gold to the SiO_2 substrate. The samples were either 30-nm-thick flat gold layers on functionalized SiO_2 slides containing MPTES deposited for different reaction times, or a 2 nm-thick Ti adhesion layer.

SERS measurements

SERS spectra were recorded on a Horiba Jobin Yvon LabRam HR 800 spectrometer, with a ×10 objective and a 785 nm diode laser [2.8 mW]. 4-Mercaptophenyl boronic acid (4MPBA) was used as a Raman probe. A monolayer of 4MPBA was adsorbed on

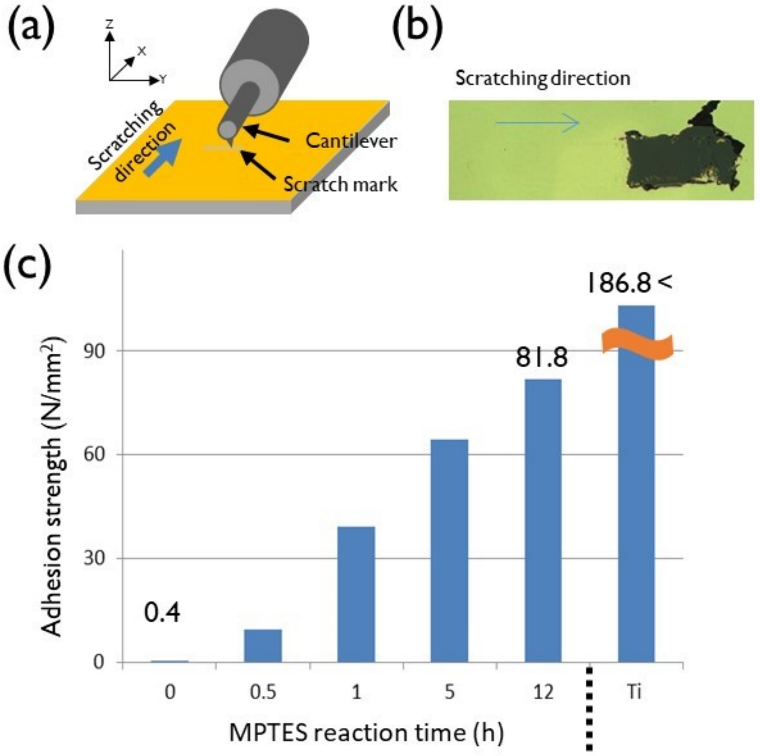

Fig. 4-2 Schematics of the (a) scratch tester and (b) microscopy image of scratched sample after measurement. (c) Adhesion strength of gold with increasing silanization reaction time, and that of the gold layer on the Ti-containing substrate.

the gold nanostructure surface by immersing it in a 4MPBA solution (1 mM in ethanol) overnight.

Surgical implantation and explantation

Ethical approval for performing the surgical experiments on two healthy female goats (Saanen) was granted by the Veterinary Faculty ethical committee of Ghent University (EC 2012/104). Before surgery the goats were anesthetized with ketamine (Ceva Santé Animale, Ketamine 1000®, 1.1mg/kg) and midazolam (Roche, Dormicum®, 0.03mg/kg) and maintained after tracheal intubation with O2 in an isofluorane mixture (Abbott Lab, Isoflo®). Routine monitoring (electrocardiogram, pulsoximetry, capnography, direct blood pressure and arterial blood gasses) was performed. After the induction of anesthesia, the animals were placed in lateral recumbency and the implantation site (flank area) was surgically prepared. For each implant, a 10-mm-long incision was made through the skin, followed by blunt dissection to create a subcutaneous pocket for the substrate. 3×3 mm^2 substrates were placed in each pocket, with the sensor surface facing outwards. Incisions were closed with resorbable sutures (Ethicon, Vicryl 2/0 muscle) and protected with a sterile self-adhesive bandage. The goats were closely monitored in the post-operative period.

After two months, the substrates were surgically explanted from the goat abdomen with their surrounding tissue following the same anesthesia protocol as described. The explanted substrates and surrounding tissue were placed in 1% buffered formalin for 3

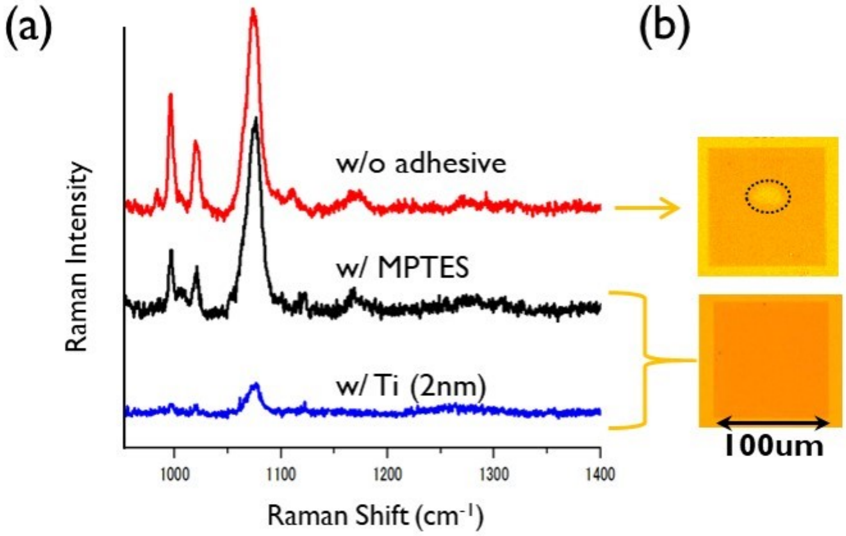

Fig. 4-3 (a) SERS spectra of 4MPBA immobilized on SERS substrates with and without adhesive layers (laser power 2.8 mW, 1.0 s exposure), (b) Microscopy images of SERS substrates after laser exposure for 20 min (laser power 2.8 mW). The black circle in the upper picture indicates the position of laser exposure and peeling off of gold nanodisks.

days, for the fixation of tissues. The substrates were then carefully removed from the tissue.

4-3 Results and discussion

To investigate the suitability of MPTES as an adhesion layer and optimize the silanization reaction time, adhesion tests were conducted using a scratch testing tool. Fig. 4-2(a) shows a gold film on a SiO2 surface being scratched in the x-direction by a vibrating diamond stylus mounted on an elastic arm; the stylus was being lowered in the z-direction (load-increasing direction). The elastic arm was deformed during lowering of the stylus. This increased the load on the film being applied by the stylus. The film broke when the shear stress exceeded the film adhesive strength, as shown in Fig. 4-2(b). The adhesion strength of gold to the Si substrate was calculated from the average share stress over five measurements.

Fig. 4-2(c) shows the adhesion strength of gold as a function of silanization reaction time, and also that of the gold layer on the Ti-containing substrate. In the absence of MPTES (i.e., 0 h reaction time), the gold adhesion strength was 0.4 N/mm^2. MPTES increased the adhesion strength of the gold layer. At a reaction time >12 h, the adhesion strength was 81.8 N/mm^2.

MPTES worked as an adhesion layer between the Au and SiO_2 layer, because the silane end group of MPTES were covalently bound to the SiO_2 through siloxane bonds. The thiol group strongly bound to the evaporated gold through Au-S bonding[145].

The increase in adhesion strength with time indicated the formation of siloxane bonds. This suggested that the adhesion strength of gold nanodisks to MPTES on SiO_2 was improved. However, by using a very long reaction time (>17 h), MPTES is prone to self-polymerization, resulting in substrate roughening[146].

In the Ti-containing sample, abrasion of the gold layer occurred prior to peeling it off of the substrate. This was because of the very high adhesion strength (186.8 N/mm^2), which was in close agreement with the gold Vickers hardness (216 N/mm^2).

To compare the SERS performance characteristics of the three SERS substrates containing different adhesive layers, 4MPBA was employed as a Raman probe.

Fig. 4-3(a) shows the SERS spectra of 4MPBA on each SERS substrate recorded under aqueous conditions, which exhibited Raman shifts at 995, 1018, 1075, and 1167 cm^{-1}. These corresponded to the γ(C-C), ν(C-S), ν(B-OH), and ν(C-B) vibrations, respectively[147]. Fig. 4-3(a) shows that the SERS signal from the Ti-containing substrate was about an order of magnitude lower than that from the substrate containing no adhesive. It is well known that Ti has a high refractive index and a strong optical absorption at the excitation wavelength, so Ti causes a damping of the plasmon resonance when the layer is in close contact with gold or silver films[143,144]. The SERS spectrum of 4MPBA on the substrate containing MPTES was similar to that on the substrate containing no adhesive. This indicated that the MPTES adhesion layer had little effect on SERS performance. This was because the MPTES layer thickness corresponded to the thickness of a single molecule, and the dielectric environment of the gold nanodisks was largely unaffected by this monolayer.

Fig. 4-3(b) shows microscopy images of the SERS substrate after laser irradiation with a 10× objective and a 785 nm diode laser [2.8 mW] for 20 min under aqueous conditions. No changes were observed in the MPTES- and Ti-containing substrates before and after irradiation. However, the gold nanodisks were removed from the substrate containing no adhesion layer. We anticipated that this was caused by local heat generation through the laser exposure. The gold nanodisks absorbing the laser produced an increase in temperature. The convection flow of the solution surrounding the gold nanodisks by heat induced the removal of the gold nanodisks from the substrate. This result indicated that the MPTES-containing substrate provided a satisfactory SERS performance and a sufficient robustness for extended high-intensity SERS measurements.

The robustness of the SERS substrate against external forces is an important factor for its application in in vivo sensing, in addition to its optical performance. In in vivo environments, these forces act on the SERS substrate surface by friction with biological tissues and by the healing of tissues that commences immediately after implantation. Thus, gold nanodisks could potentially peel off of the SERS substrate.

To investigate the robustness of the MPTES-containing substrate for in vivo sensing, 3×3 mm^2 substrates were implanted in the skin of a goat abdomen for 2 months, as

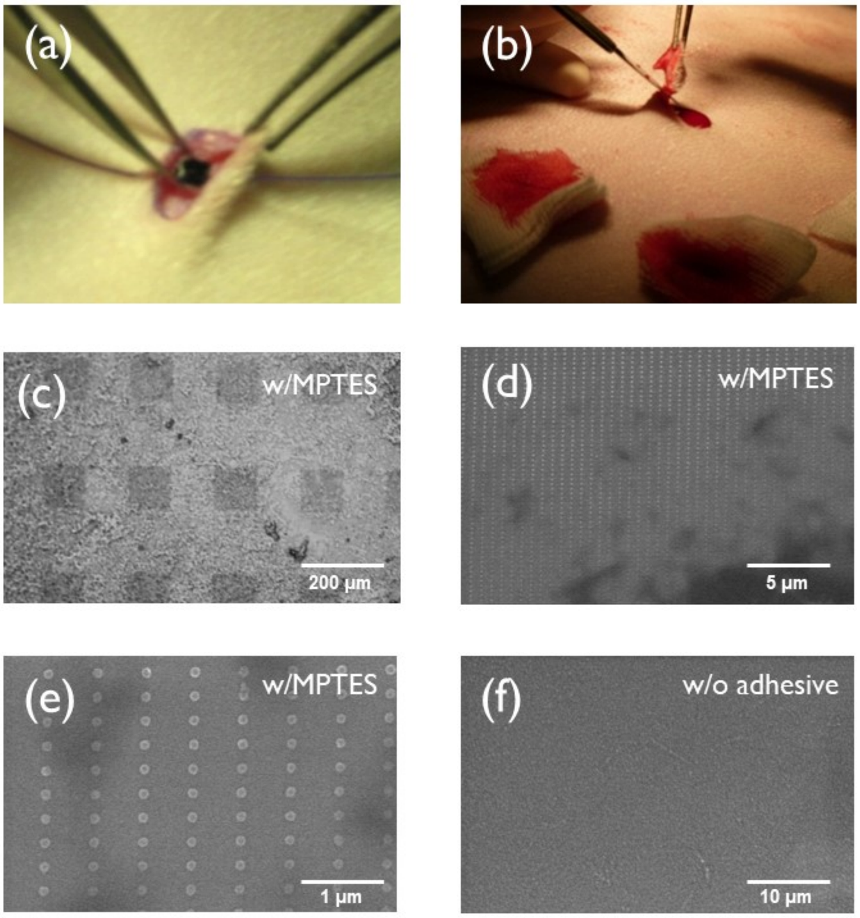

Fig. 4-4 (a) 3×3 mm2 SERS substrate being implanted in the skin of a goat abdomen, and (b) explantation with surrounding tissues. (c) Bright-field image (×10 magnification), SEM images of the same SERS substrate with MPTES at (d) ×10,000 and (e) ×50,000 magnification, and (f) SEM images of the SERS substrate without MPTES after implantation for 2 months at ×5,000 magnification.

shown in Fig. 4-4(a) and (b). Fig. 4-4(c) shows a representative microscopy image of the explanted SERS substrate at ×10 magnification. A 100 µm square array of gold nanodisks was observed. A conductive polymer (Showa denko, ESPACER) was coated on the surface to prevent charging by the residual tissue, and SEM images were recorded at ×10000 and ×50000 magnifications, as shown in Fig. 4(d) and 4(e), respectively. Darker areas indicated thicker tissues on the substrate. The MPTES nanostructure as well as a Ti coated substrate (picture not shown) remained intact, and the adhesion of the gold nanodisks was sufficient for the forces applied during healing and friction with the body tissue. During implantation, the gold nanodisks peeled off of the substrate containing no adhesive [Fig. 4-4(f)].

4-4 Conclusions

MPTES-containing SERS substrates were prepared by etching process with EBL. The MPTES adhesion layer provided an adhesion strength of ~80 N/mm2 between the gold and the SiO2 surface. This was ~200 times greater than the adhesion strength in the absence of an adhesion layer (0.4 N/mm^2). The SERS substrate was sufficiently robust for extended high-frequency measurements without plasmon loss. The substrate was robust in an in vivo environment, as evidenced by its implantation for 2 months. This substrate has potential in in vivo SERS sensing. In future work, SERS signal detection will be examined with the substrate implanted in an animal model.

Chapter 5

Immuno-based virus sensing using surface enhanced fluorescence

5-1 Introduction

Flu epidemics, which occur annually during the winter in the northern hemisphere, caused economic losses, and even mortality in older people, children, or immunocompromised individuals due to its high morbidity[148,149]. Recently, Yan et al. reported that the RNA of influenza virus was found in the exhaled breath from infected patients, without sneezing or coughing[150]. They reported influenza virus RNA was detected in 76% of the exhaled aerosol samples below 5 μm in diameter and 40% of the exhaled aerosol samples over 5 μm in diameter. This suggested that sneezing was not important for viral shedding. Moreover, the infectiousness of the sampled aerosol below 5 μm in diameter was examined and infectiousness was confirmed in 39% of samples[150]. Moreover, Kormuth et al. showed that aerosolized influenza virus co-existed with extracellular material originating from the apical surface of human bronchial epithelial cells, retaining their viability in a wide range of relative humidities.[151] These observations suggest that influenza virus detection in the environment is important for assessing the risk of influenza infection, although the mechanism of influenza transmission is still under discussion[152].

Immuno-based assays have been successfully applied in diagnostics, the pharmaceutical industry, the food industry, and in environmental monitoring due to the high specificity and sensitivity that they offer[153–155]. Antibodies, one of the most important elements in immuno-based assays, determine the specificity and sensitivity, and the characteristics of the antibodies, especially their affinity to the analyte, cross reactivity, and low level of non-specific adsorption are important. Camelid single variable domain heavy chain (VHH) antibodies were discovered about 25 years ago.[156] These antibodies don't have the light chain naturally, so its structure is simple compared to IgG, of which characteristics offers many advantages in terms of large-scale production, ease of genetic modification, and resilience to organic solvents and temperature[157,158]. VHH antibodies could potentially be used in an immuno-based assay for environmental sensing, such as the specific detection of a virus, fungus, or bacterium in a residential environment. The characteristics of VHH antibodies have been intensively investigated as well as their potential applications in clinical therapeutics[159], immunodiagnostics[160], environmental monitoring[157], and small molecular detection[157].

For highly sensitive detection using an immuno-based assay, a transducer that converts the antigen–antibody reaction to a detectable signal is important[161]. Surface plasmon resonance (SPR) is a powerful tool for analysis of the antibody characteristics of an antigen–antibody reaction[162] and requires an enhancer for the optical response such as Raman scattering or fluorescence[12,25,163]. Surface enhanced fluorescence, which enhances the fluorescent intensity of the fluorophore, occurs because the electric field of exciting light is strongly enhanced by the surface plasmon resonance[164] or localized SPR[165]. This phenomenon occurs in close proximity to the plasmonic structure, such as the gold nanostructures or thin gold film, and is applicable as an enhancer for the fluorescent probe. The characteristics of surface enhanced fluorescence require suppression of non-specific adsorption of the fluorescence probe to the plasmonic structure for high signal-to-noise ratio detection[20] because the fluorescence from the non-specifically-bound fluorescence probe is also enhanced.

For the suppression of non-specific adsorption, many researcher have been intensively investigated. To reduce the non-specific adsorption, the role of intermediate water is important to repel the protein from the surface.[166] In this purpose, BSA[167],[168] or polyethylene glycol (ethylene glycol: EG)[169], has been mainly used. Especially, EG monolayer with thiol end group are employed for the gold surface functionalization as a suppressor of non-specific adsorption[170],[171].

In this chapter, we investigated the application of VHH antibody in an immuno-based assay for influenza nucleoprotein A detection with surface enhanced fluorescence. We demonstrate successful suppression of non-specific adsorption of the fluorescence probe for high signal-to-noise ratio detection.

5-2 Materials and methods

Reagents.

11-Mercaptoundecanol triethyleneglycol ether (hydroxy-EG3-undecanethiol) and 20-(11-mercapto-undecanyloxy)-3, 6, 9, 12, 15, 18-hexaoxaeicosanoic acid (carboxy-EG6-undecanethiol) for plasmonic substrates functionalization were purchased from Doujindo Laboratories (Kumamoto, Japan). Anhydrous ethanol was purchased from FUJIFILM Wako Chemical (Japan). 1-(3-Dimethylaminopropyl)-3-ethylcarbodiimide hydrochloride (EDC) and N-hydroxysuccinimide (NHS) for the EDC/NHS reaction were purchased from Tokyo Chemical Industry Co., Ltd. (Tokyo, Japan). ELISA assay diluent (5x) as bovine serum albumin (BSA) and glucosamine hydrochloride as the blocking agent were purchased from BioLegend (San Diego, CA, USA) and FUJIFILM Wako Pure Chemical, respectively. Anti NP VHH antibodies (1C6 and 2B9) were purchased from the Antibody Engineering Research Center (Chiba, Japan). Anti-FLAG IgG (F1804) was purchased from Sigma-Aldrich. Dylight 800™ NHS ester as a fluorescent dye and 0.67 M borate buffer were purchased from Thermo Fisher Scientific (Waltham, MA, USA). Influenza A H1N1 (A/Puerto Rico/8/34/Mount Sinai) recombinant nucleoprotein A was purchased from Sino Biological Inc. (Beijing, China).

Affinity constant measurement of VHH antibody by SPR.

Affinity constant measurements of two VHH antibodies were performed using a Biacore T200 analytical system (GE Healthcare UK Ltd., Buckinghamshire, England) with a multi kinetics method. CM5 sensor chips (GE Healthcare UK Ltd.), consisting of a gold-coated glass which surface is functionalized with a carboxymethyl dextran layer were used. Anti-FLAG IgG were immobilized to the sensor surface by the EDC/NHS reaction using the recommended amine coupling kit (GE Healthcare Bio-Sciences). The carboxyl end groups of sensor chip surface were activated using 37.5 mg/mL EDC solution and 5.75 mg/mL NHS solution. After activation, a 29 mg/mL of anti-FLAG IgG solution diluted in 10 mM sodium acetate buffer, pH 5.0, was injected for 420 s. After immobilization of anti-FLAG IgG, the active carboxyl end groups which was not reacted with anti-FLAG IgG were deactivated with 35 μL of 1 M ethanolamine-hydrochloride, pH 8.5. Then, 100 nM influenza nucleoprotein A solution (A/Puerto Rico/8/34/Mount Sinai) with FLAG-tag, which was biosynthesized using the SF9 cell line, was prepared in PBS-T buffer (pH 7.4, 0.15 M NaCl, 0.05% v/v Tween 20). Prepared influenza nucleoprotein A solution was injected for 60 s association, followed by injecting PBS-T buffer for 600 s dissociation to stabilize the captured nucleoprotein A. A two-fold dilution from 12.5 nM to 0.0975 nM for VHH antibody 1C6 and from 25 nM to 0.19 nM for VHH antibody 2B9 were prepared in PBS-T buffer and 60 μL of each solution was applied at a flow rate of 30 μL/min. After the injection of the VHH antibody, 300 μL of PBS-T buffer was applied at the same flow rate for the dissociation phase measurement of VHH antibody. After acquisition of sensorgram of association and dissociation for a concentration of VHH antibody, the sensor chip surface was regenerated by using 1 M arginine hydrochloride solution for different VHH antibody. Sequentially, another concentrations of VHH antibodies (from 0.0975 nM to 12.5 nM for 1C6, from 0.19 nM to 25 nM for 2B9) were injected for sensorgram acquisition. The association/dissociation constants of each VHHs were calculated by using Biacore Evaluation Software version 4.1 (GE Healthcare Bio-Sciences) from the obtained sensorgrams. A Langmuir model under the assumption of 1:1 binding of antigen and antibody is used for fitting the obtained sensorgram.

VHH antibody preparation for fluorescence measurement.

VHH antibody 1C6 was employed as a primary antibody and 2B9 as a secondary antibody. The concentration of 1C6 solution was 10 μg/mL in PBS buffer at pH 7.4, with 0, 0.01, 0.1, 1, and 10% (w/v) of glucosamine added to evaluate the blocking effect of glucosamine hydrochloride. For 2B9, Dylight 800™ was immobilized to 2B9 VHH antibody via the following procedure. Briefly, 3 mL of 1.8 mg/mL of 2B9 PBS solution and 240 μL of 0.67 M borate buffer were mixed, followed by the addition of 1.62 mL of Dylight 800™ NHS ester and the mixture was incubated for 1 h at room temperature protected from the light. Then buffer exchange to 50 mM

Tris-HCl was performed. After buffer exchange, dye-immobilized 2B9 was purified by anion exchange chromatography to remove non-reacted dye and 2B9 using a Mono Q 5/50GL column purchased from GE Healthcare UK Ltd.. After purification, the degree of labeling was estimated by measuring the absorbance at 280 nm and 777 nm. The estimated degree of labeling was 0.72. Finally, the concentration of dye-immobilized 2B9 was adjusted to 0.5 μg/mL with diluted ELISA assay diluent (1/10) at pH 7.4.

Plasmonic substrate preparation.

To prepare the plasmonic substrate, an olefin nano-imprint film with dome-shaped structures was employed, as previously reported[88]. The width, pitch, and height of the structures were 230, 460, and 200 nm, respectively. An Au film of 400 nm in thickness was deposited by sputtering onto the structure, an. Fig. 5-1 shows a scanning electron micrograph after Au film deposition. Fig. 5-1(a) and (b) show top views of the plasmonic structure at 10,000 and 30,000 magnifications, respectively. Fig. 5-1(c) shows the tilted (52 degree) view at a 50,000 magnification, and Fig. 5-1(d) shows the cross sectional view at a 30,000 magnification. As shown in Fig. 5-1, each elements of the plasmonic structure is arranged as hexagonal closed packed structure and the diameter is around 460nm. Fig. 5-2 shows the reflection spectrum of plasmonic substrate. The arrows in Fig. 5-2 shows the localized surface plasmon resonance wavelengths. From Fig. 5-2, two localized surface plasmon resonance is occurred around 610nm and 790nm. Surface enhanced fluorescence is occurred by the electric field enhancement of excitation light and fluorescence emission due to plasmon resonance. The dye in this work is excited at 785nm and emitted fluorescence at 800nm, so the plasmonic substrates in this work is suited to induce surface enhanced fluorescence. Just after Au deposition, plasmonic substrates were immersed into a mixed solution comprising equal amounts of 0.75 mM hydroxy-EG3-undecanethiol and 0.25 mM carboxy-EG6-undecanethiol anhydrous ethanol solution for overnight incubation at room temperature, followed by rinsing with anhydrous ethanol and blow drying with N2 gas. After surface functionalization with hydroxy-EG3-undecanethiol and carboxy-EG6-undecanethiol, the plasmonic substrates were settled in 24-cell plates and the carboxyl end group was activated by immersing it into 1 mL/well of mixed solution comprising equal amounts of 400 mM EDC in MES buffer and 100 mM NHS in MES buffer for 15 min at room temperature protected from the light. The pH of the EDC and NHS solutions was 4.7. After removal of EDC and NHS solution, 1 mL/well of the 1C6 VHH antibody and glucosamine hydrochloride mixture was poured immediately and incubated for 2 h at room temperature with shaking. Following incubation, the substrates were washed three times with PBS-T buffer and were blocked with ELISA assay diluent (1x).

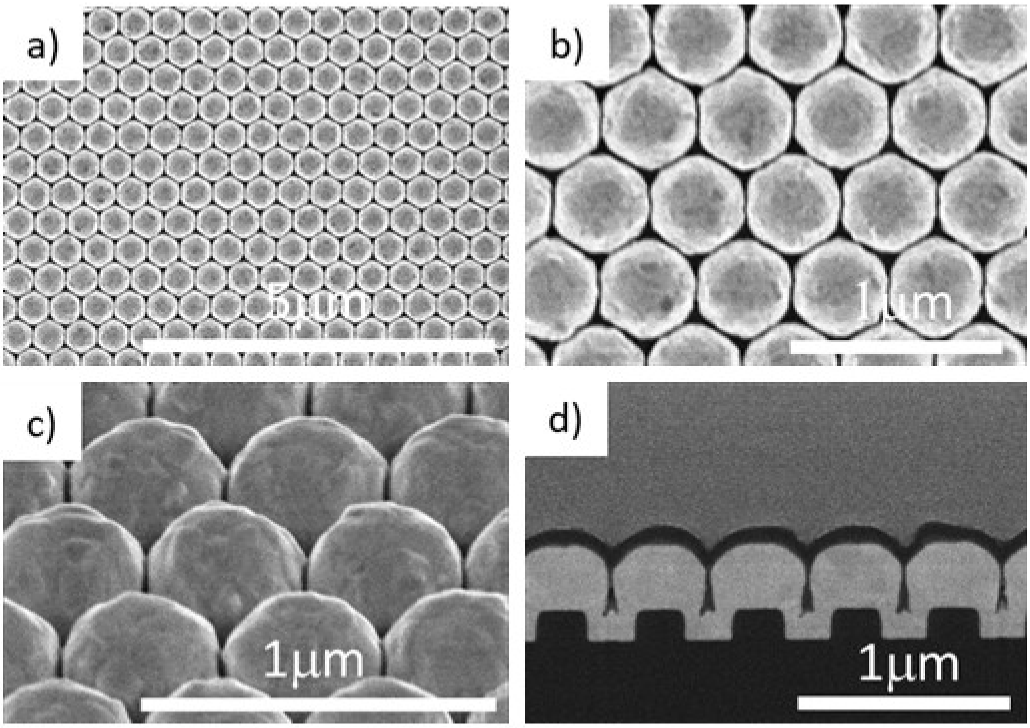

Fig. 5-1 Scanning electron micrograph of plasmonic substrates. (a) top view, (b) top view (high magnification), (c) tilted (52 degree) view, (d) cross-sectional view

Immunoassay and detection of nucleoprotein A by fluorescence measurements.

After immobilization of 1C6 VHH antibody, the plasmonic substrates were incubated in 1 mL of influenza A H1N1 (A/Puerto Rico/8/34/Mount Sinai) recombinant nucleoprotein A solution for 1 h at room temperature. Nucleoprotein A was diluted in ELISA assay diluent (1x) to concentrations of 1000, 100, 10, 1, 0.5, 0.1, and 0.05 pM. After incubation, the substrates were washed three times with PBS-T buffer and immersed into 500 μL of 0.5 μg/mL dye-immobilized 2B9 VHH antibody solution and incubated for 1 h at room temperature. After incubation with dye-immobilized VHH antibody, the substrates were washed three times with PBS-T, then immediately immersed into Milli-Q water to avoid precipitation of constituents of the PBS-T buffer and were dried under nitrogen gas.

For the detection of nucleoprotein A by fluorescence measurements, a self-constructed optical system comprising a 785-nm diode laser (PDLD Inc., Germany) and an iHR-320 spectrometer (HORIBA, Ltd., Japan) with a Symphony liquid nitrogen cooling Charge Coupled Device (CCD) detector (HORIBA, Ltd., Japan) was employed. A dichroic mirror (LP02-785RE-25, Semrock, USA) was used to separate the laser line and emitted fluorescence from the dye immobilized on the VHH 2B9 antibody. The 785-nm excitation light (50 μW) was focused on the substrates using a 10x objective lens (NA=0.3, Nikon, Japan). The emitted fluorescence was corrected using the same objective lens and was transferred to the iHR320 spectrometer. The acquisition time of the CCD was 0.5 s.

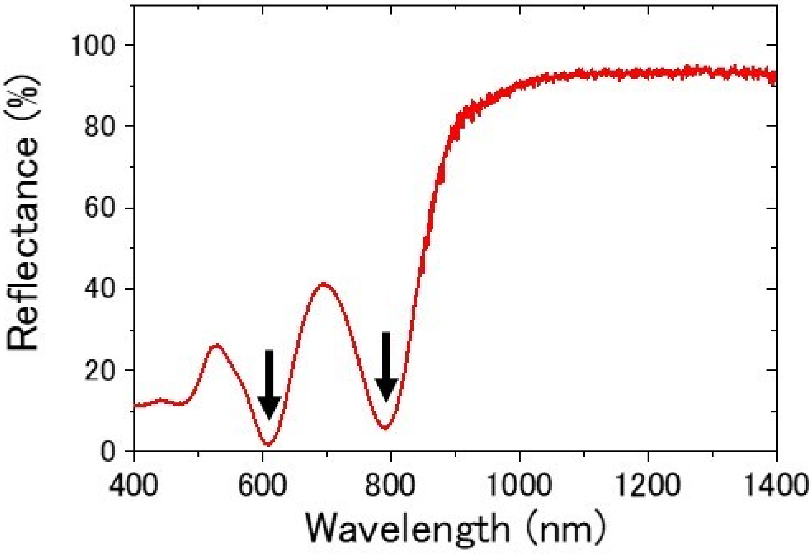

Fig. 5-2 Reflection spectrum of plasmonic substrate. The arrows show plasmon resonance

5-3 Results and discussion

Affinity constant measurement by SPR.

The association and dissociation constants are quite important parameters to analyze antigen-antibody reaction. Fig. 5-3 shows a schematic image of the experimental setup. First, a 29 mg/mL anti-FLAG IgG was coupled to the CM5 chip surface to immobilize the biosynthesized FLAG-tagged influenza nucleoprotein A solution via the FLAG-tag for easy regeneration to conduct a multi kinetics method[172]. Using the biosynthesized nucleoprotein A, affinity constant measurements should be done preferably using a monomer to confirm the 1:1 reaction of antibody and antigen. However, influenza nucleoprotein A readily forms oligomers[173]. To overcome this, after synthesis of nucleoprotein A, size exclusion chromatography was employed to separate monomers from a mixture of multimers of nucleoprotein A. Then VHH antibodies were injected from low concentration (0.0975 nM for 1C6, 0.19 nM for 2B9) to high concentration (12.5 nM for 1C6, 25 nM for 2B9). Fig. 5-4(a) and (b) show the resulting sensorgrams when 1C6 and 2B9 VHH antibodies were injected. Table 5-1 shows the obtained association/dissociation rates and dissociation constant that were calculated by fitting the sensorgram of SPR with a 1:1 Langmuir model. Both VHH antibodies showed good interactions with nucleoprotein A because the dissociation constants of both 1C6 and 2B9 were low (9.5×10^{-10} and 2.2×10^{-10}, respectively).

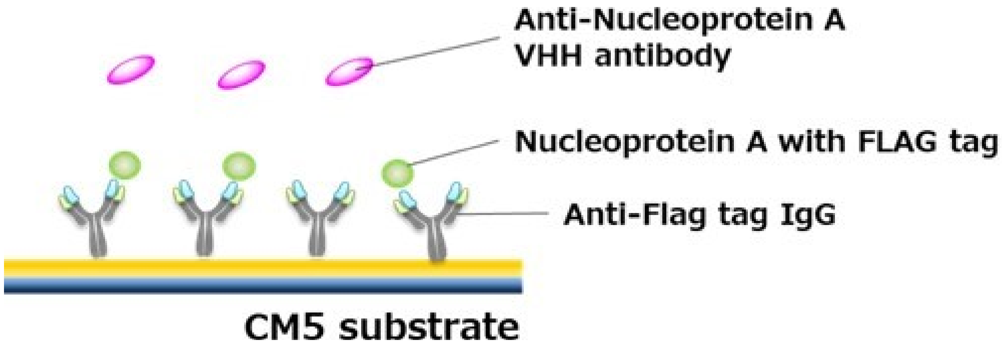

Fig. 5-3 Schematic image illustrating the experimental setup for affinity constant measurements

This means that both VHH antibodies have high affinity for nucleoprotein A. The sensorgram (Fig. 5-4) shows that 1C6 has a high association rate ($k_{on}=4.2 \times 10^6$), whereas 2B9 has a low dissociation rate ($k_{off}=2.3 \times 10^{-4}$). These characteristics indicate that both VHH antibodies have desirable characteristics for an immunoassay.

Immunoassay and detection of nucleoprotein by fluorescence measurements.

At first, the amount of non-specific adsorption of dye-immobilized VHH antibody was examined because surface enhanced fluorescence has quite high sensitivity in the vicinity of the surface of the Au nanostructure due to the highly enhanced electric field generated by the surface plasmon resonance. To reduce the non-specific adsorption, the role of intermediate water is important to repel the protein from the surface[166].

To suppress the non-specific adsorption, BSA, carboxy-EG6-undecanethiol for VHH antibody immobilization and hydroxy-EG3-undecanethiol, which contain oligo ethylene glycol, were employed because ethylene glycol has intermediate water and reduces non-specific adsorption[174]. Moreover, to add more hydroxyl end groups to the plasmonic substrate's surface to suppress non-specific adsorption, glucosamine hydrochloride was employed to cap the activated carboxyl end group instead of ethanolamine. To confirm the effect of the amount of glucosamine hydrochloride, 1C6 VHH antibody and glucosamine hydrochloride were co-functionalized by changing the concentration of glucosamine hydrochloride. The 1C6 VHH antibody was diluted with

Table 5-1 Obtained association and dissociation constants by fitting the sensorgram using a 1:1 Langmuir model

	K_{on}(1/Ms)	K_{off}(1/s)	K_{D}(M)
1C6	4.22 X 10^{6}	4.02 X 10^{-3}	9.52 X 10^{-10}
2B9	1.04 X 10^{6}	2.33 X 10^{-4}	2.24 X 10^{-10}

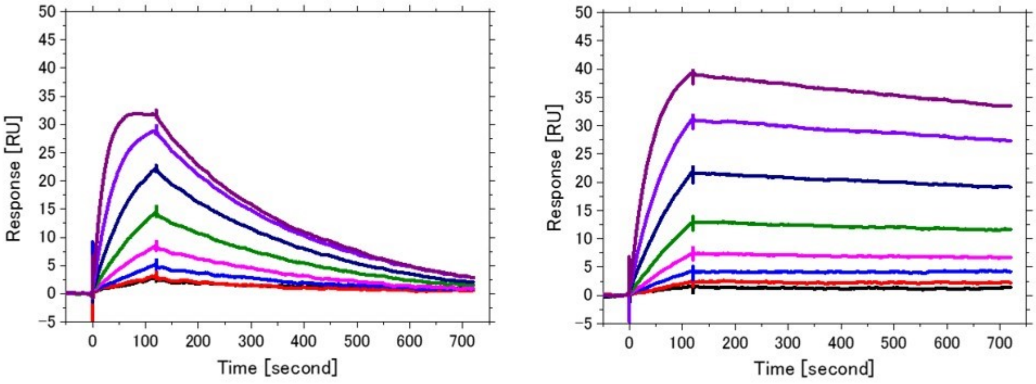

Fig. 5-4 Sensorgrams of affinity constant measurements of (a) 1C6 VHH antibody, (b) 2B9 VHH antibody. A sensorgram from 0 to 120 seconds shows the association reaction and from 120 seconds onwards shows the dissociation reaction.

PBS buffer containing glucosamine hydrochloride at a concentration of 0.01, 0.1, 1, and 10% (w/v).

By reacting the mixture of glucosamine hydrochloride and 1C6 VHH antibody to the activated carboxyl end group of the plasmonic substrate, the VHH antibody and glucosamine hydrochloride can be co-immobilized to the plasmonic substrate's surface via the primary amine end group. The immobilized amount of VHH and glucosamine hydrochloride can be determined by the concentration of VHH and glucosamine hydrochloride according to the law of mass action. Fig. 5-5(a) and (b) show the glucosamine hydrochloride concentration dependence of the fluorescence intensity when the nucleoprotein A concentrations were 0 nM and 1 nM, respectively. The fluorescence intensity of 0 nM of nucleoprotein A (Fig. 5-5(a)) shows the amount of non-specific adsorption of dye-immobilized 2B9 VHH antibody to the plasmonic substrate. When the glucosamine hydrochloride concentration was zero (the far left data in Fig. 5-5(a)), the fluorescence was intense and showed a wide distribution. This indicated that the effect of the hydroxy-EG3-undecanethiol and carboxy-EG6-undecanethiol mixture for avoiding non-specific adsorption was neither sufficient nor stable. The fluorescence intensity became weaker with increased glucosamine hydrochloride concentration, which indicated that glucosamine hydrochloride is effective for the suppression of non-specific adsorption of dye-immobilized 2B9 VHH antibody to the plasmonic substrate. The non-specific adsorption of dye-immobilized 2B9 VHH decreased to a seventh of its original level when the glucosamine

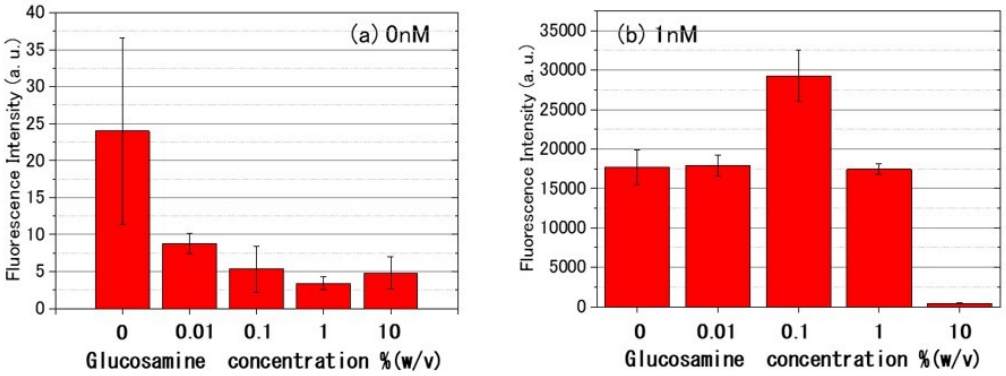

Fig. 5-5 Glucosamine hydrochloride concentration dependency of fluorescence intensity under BSA and ethylene glycol existence when the nucleoprotein A concentration was (a) 0 nM and (b) 1 nM. Error bar shows standard deviation of 5 measurements.

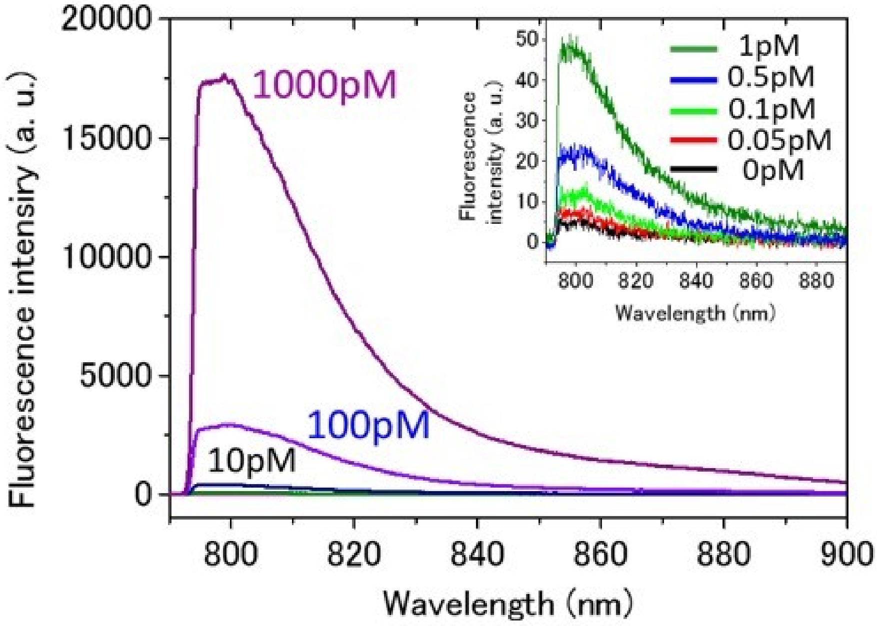

Fig. 5-6 Fluorescence spectra with different nucleoprotein A concentrations at 1% (w/v) glucosamine hydrochloride. Inset shows magnified spectra at low concentration.

hydrochloride concentration was 1% (w/v).

The fluorescence intensity of 1 nM of nucleoprotein A (Fig. 5-5(b)) was weakest when the glucosamine hydrochloride concentration was 10% (w/v). The procedure of data analysis is shown in supplemented information. As the amount of glucosamine hydrochloride increases, the amount of immobilized hydrochloride also increases, whereas the amount of immobilized 1C6 VHH decreases. The small amount of immobilized 1C6 VHH can bind to a small amount of nucleoprotein A, which leads to less dye-immobilized 2B9, resulting in weak fluorescence. When 0.01% and 1% (w/v) glucosamine hydrochloride was added, the fluorescence intensity was almost the same. The fluorescence intensity of 0.1% (w/v) glucosamine hydrochloride was about 1.6 times higher than that of 0.01% glucosamine hydrochloride. [174,175] Fig. 5-6 shows typical fluorescence spectra with different nucleoprotein A concentrations and 1% (w/v) glucosamine hydrochloride. The inset is the magnified spectra corresponding to a low concentration of nucleoprotein A. The peak of fluorescence intensity is around 800 nm, which corresponds to a fluorescence intensity peak of dylight 800™. The peak intensity clearly depends on the concentration of nucleoprotein A. The fluorescent intensity at 0 pM, although small, seems to reflect the shape of the dylight 800™ spectrum because the peak is around 800 nm. The amount of non-specific adsorption of dye-immobilized VHH antibody is considerably suppressed, but the fluorescence is still observed.

Fig. 5-7 shows the nucleoprotein A concentration dependence of the fluorescence intensity at 800 nm, which is drawn as a double-logarithmic graph. The red solid horizontal line in Fig. 5-7 shows the average fluorescence intensity of 0 nM nucleoprotein A and the dashed line shows the standard deviation. The inset in Fig. 5-7 shows a linear plot of the low concentration range. Nucleoprotein A was detected in the concentration range over four orders of magnitude from 0.1 to 1000 pM. As shown in the graph in the inset, fluorescence at 0.1 pM was still observed although dye-immobilized VHH antibodies have only 0.72 molecules per one molecule of VHH, as indicated in the Materials and Methods. If the degree of dye-labeling to VHH antibodies is increased, the fluorescence intensity would also increase, which would help lower the limit of detection.

To evaluate the limit of detection of nucleoprotein A, the slope of the linear approximation was calculated in the range from 0.01 to 1 pM, which is shown in the inset of Fig.5-7. We employed an unweighted linear model for fitting the data. The slope of the linear approximation line was 43.2, the intercept was 3.75. The standard deviation at 0 pM determined by the fluorescence measured at 0 pM was 12.6 in the absence of glucosamine hydrochloride and 0.87 with the addition of 1% (v/v) glucosamine hydrochloride. Because the fluorescence intensities of 1 nM at 0% (v/v) hydrochloride and 1% (v/v) glucosamine hydrochloride appeared the same from Fig. 5-5(b), the slope of 0% (v/v) can be assumed to be the same as that of 1% (v/v) hydrochloride. As the limit of detection is calculated by the 3σ/slope, the limit of of this

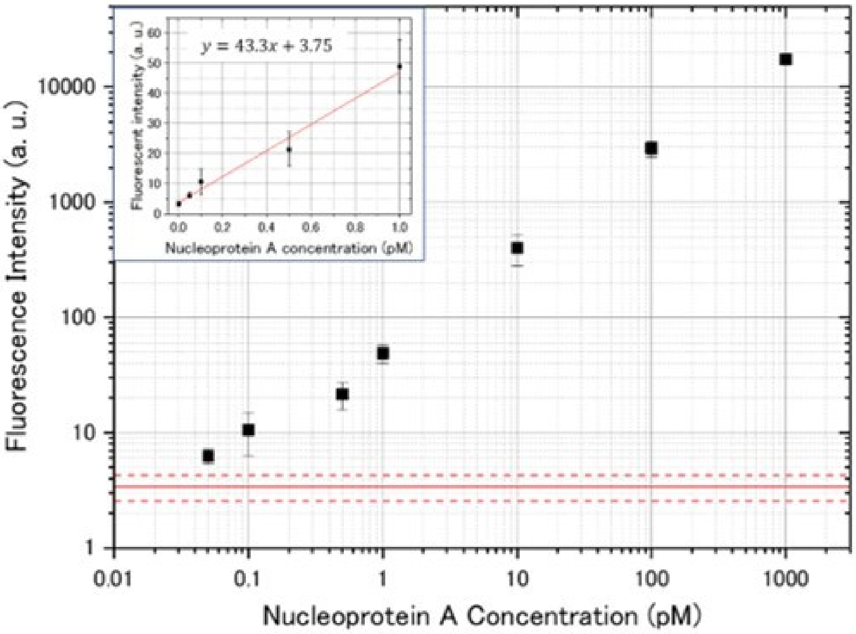

Fig. 5-7 The nucleoprotein A concentration dependency of fluorescence intensity at 800 nm in a double-logarithmic scale. Inset shows magnification of the graph around the low concentration region in a linear scale, regression line and function. Red solid line shows averaged fluorescent intensity at blank, red dashed line shows standard deviation at blank from 5 times measurement.

assay was found to be 0.875 pM in the absence of glucosamine and 60 fM for 1% (v/v) glucosamine addition. Therefore, the addition of 1% (v/v) glucosamine hydrochloride lowers the detection limit 15 times due to the suppression of non-specific adsorption of dye-immobilized VHH antibody.

5-4 Conclusions

We developed an ultrasensitive VHH antibody-based immunoassay for nucleoprotein A using surface enhanced fluorescence for signal enhancement. The affinity constant of VHH antibodies was evaluated and the dissociation constants of these antibodies were estimated to be 9.5×10^{-10} for 1C6 and 2.2×10^{-10} for 2B9. This means that both VHH antibodies have high affinity to nucleoprotein A, i.e., 1C6 VHH antibody has a high association rate ($k_{on}=4.2 \times 10^{6}$) and 2B9 VHH antibody has a low dissociation rate ($k_{off}=2.3 \times 10^{-4}$). These values indicate that both VHH antibodies have desirable characteristics for the immunoassay.

We demonstrated that by applying 1% (v/v) glucosamine hydrochloride for co-immobilization with a capture VHH antibody as a suppressor of non-specific adsorption of dye-immobilized VHH antibody, a detection limit of 60 fM can be achieved, which is 15 times lower than that achieved in the absence of glucosamine hydrochloride. This low detection limit has been achieved whilst maintaining the benefits of the VHH antibody, such as large-scale production, ease of genetic modification, thermal resistance and high stability, which are important for environmental sensing in residential environments. Our findings are therefore an important breakthrough for assessing various risks in residential environments. Although nucleoprotein A of influenza was detected in this work, the VHH antibody assay with surface enhanced fluorescence could be readily extended to other targets by changing the type of VHH antibody.

Chapter 6

Conclusions and outlook

Throughout in this thesis, we focused on the tuning the plasmonic properties for surface enhanced spectroscopy in near infrared region toward biosensing applications including *in vivo* and *in vitro* sensing.

In Chapter 2, we have demonstrated the fabrication of the Au nanorings–SiO2–Au film structures by using nanosphere lithography technique to enhance SERS enhancement factor by between the Au nanorings and the Au film. In the result, we can tune the plasmonic coupling and we have achieved a maximum NIR SERS EF as large as 1.4×10^7, an improvement with a factor of 50 times compared to the Au nanorings.

In chapter 3, we have studied optimizing conditions to enhance responses of a double-resonance nano-disk array for NIR SERS in water by tuning the SPPs and LSPs coupling. We showed high tunability of the SPP and LSP resonance wavelengths by changing the pitch and diameter of Au nano-disks through FDTD simulations and experiments. By the optimization of the SPP and LSP resonance wavelengths, a maximum averaged NIR SERS EF of 7.8×10^7 can be achieved in water.

In chapter 4, high robustness SERS substrates were fabricated by using MPTES as adhesion layer for *in vivo* applications. The MPTES adhesion layer provided an adhesion strength of ~80 N/mm2 between the gold and the SiO2 surface. This was ~200 times greater than the adhesion strength in the absence of an adhesion layer (0.4 N/mm^2). The SERS substrate was sufficiently robust for extended high-frequency measurements without plasmon loss. The robustness of the substrate was shown at *in vivo* environment, as evidenced by its implantation for 2 months. We have shown this substrate has potential for *in vivo* SERS sensing.

In chapter 5, we developed an ultrasensitive VHH antibody-based immunoassay for nucleoprotein A using surface enhanced fluorescence for signal enhancement by suppressing non-specific adsorption of dye-immobilized VHH antibody. In this chapter, we have shown it's important for biosensing applications to improve not only an enhancement factor but also surface functionalization to exploit the detection ability of surface enhanced fluorescence. Our findings are an important breakthrough for assessing various risks in residential environments.

We have provided a proof of principle for several elemental technology for biosensing applications using surface enhanced spectroscopy. To commercialize these applications, there are still many questions and tasks to be solved.

(i) Stability for nanostructure fabrications for mass production.

Almost applications based on plasmonics are still in research phase. Difficulty to fabricate nanostructure in desired tolerance at mass production can be a one of the reason[7,176]. The advanced lithography such as DUV[177], or nanoimprint technology[88] can be a candidate to solve

(ii) Further investigation about toxicity of nanomaterials *in vivo* and SERS detection through subcutaneous tissue.

Gold in its bulk form consider as inert, biocompatible, and non-toxic. But when the size of gold goes to nanometer-order, the behavior is completely different compared to bulk.[178] Especially, toxicity regarding to genotoxic, mutagenicity or cytotoxicity are determined by the size of material, surface chemistry, and charged surface functional groups.[179] To evaluate the biocompatibility of Au plasmonic nanomaterials rigorously with reliability and realistic data, the establishment of a standardized experimental protocol is needed.[178] This is a great issue to be solved to commercialize plasmonic applications *in vivo*.

For the detection of SERS through subcutaneous tissue, a large progress has been made for *in vivo* SERS applications[180–183]. In terms of instrumentation, particularly glucose monitoring, user-friendly and intuitively instrumentation is needed for real use rather than specialized equipment[184] though Raman spectroscopy requires quite high resolution of wavelength.

(iii) Construction of integrated sensing system from sampling to detection

Viral detection from residential environment to assess the risk of infection with high sensitivity, it’s quite important to not only the improvement of enhancement of detection, but also efficient sampling and transporting to sensing position. Especially airborne viral detection, there is difficulty in confinement of large volume air sample into small volume of sample solution. Sophisticated total sensing system design is needed to commercialize virus detection system to manage high sensitivity and user-friendly system.

Bibliography

(1) Freestone, I.; Meeks, N.; Sax, M.; Higgitt, C. The Lycurgus Cup - A Roman Nanotechnology. *Gold Bull.* **2008**, *40* (4), 270–277.

(2) Mie, G. Beiträge Zur Optik Trüber Medien, Speziell Kolloidaler Metallösungen. *Ann. Phys.* **1908**, *330* (3), 377–445.

(3) Wood, R. On a Remarkable Case of Uneven Distribution of Light in a Diffraction Grating Spectrum. *Philos. Mag.* **1902**, *18*, 396–402.

(4) Otto, A. Excitation of Nonradiative Surface Plasma Waves in Silver by the Method of Frustrated Total Reflection. *Zeitschrift für Phys.* **1968**, *216* (4), 398–410.

(5) Kretschmann, E.; Raether, H. Radiative Decay of Non Radiative Surface Plasmons Excited by Light. *Zeitschrift fur Naturforsch. - Sect. A J. Phys. Sci.* **1968**, *23* (12), 2135–2136.

(6) David, P. Collective Energy Losses in Solids. *Rev. Mod. Phys.* **1956**, *28* (3), 184–198.

(7) Le Ru, E. C.; Etchegoin, P. G. *Principles of Surface-Enhanced Raman Spectroscopy*; Elsevier: Amsterdam, 2009.

(8) Maier, S. A. *Plasmonics: Fundamentals and Applications*; Springer Science+Business Media LLC, 2007.

(9) Barnes, W. L.; Dereux, A.; Ebbesen, T. W. Surface Plasmon Subwavelength Optics. *Nature* **2003**, *424* (August), 824–830.

(10) Xia, Y.; Halas, N. J.; Editors, G. S Hape-Controlled Surface Plasmonic Nanostructures. *MRS Bull.* **2005**, *30*, 338.

(11) Jackson, J. D. *Classical Electrodynamics*, Third Edit.; John Wiley & Sons, Inc, 1999.

(12) Kneipp, K.; Wang, Y.; Kneipp, H.; Perelman, L. T.; Itzkan, I.; Dasari, R. R.; Feld, M. S. *Single Molecule Detection Using Surface-Enhanced Raman Scattering (SERS)*; 1997.

(13) C.V. Raman; Krishnan, K. S. A New Type or Secondary Radiation. *Nature* **1928**, *121*, 501.

(14) Catchpole, K. R.; Polman, A. Design Principles for Particle Plasmon Enhanced Solar Cells. *Appl. Phys. Lett.* **2008**, *93*, 191113.

(15) Fleischmann, M.; Hendra, P. J.; McQuillan, A. J. Raman Spectra of Pyridine Adsprbed at a Silver Electrode. *Chem. Phys. Lett.* **1974**, *26* (2), 2–5.

(16) Jeanmaire, D. L.; Van Duyne, R. P. In Relating the Observables to Molecular Parameters ; (2) the Selection of Elec- Trodes , Potential Range , or Solvents Is Restricted ; and (3) There Is Limited Molec- Ular Specificity . Consequently , a Definite Need Exists for the Development of New. *J. Electroanal. Chem.* **1977**, *84*, 1–20.

(17) Albrecht, M. G.; Creighton, J. A. Anomalously Intense Raman Spectra of Pyridine at a Silver Electrode. *J. Am. Chem. Soc.* **1977**, *99* (15), 5215–5217.

(18) Guimbretière, G.; Duraipandian, S.; Ricci, T. Field Remote Stokes/Anti-Stokes Raman Characterization of Sulfur in Hydrothermal Vents. *J. Raman Spectrosc.* **2018**, *49* (8), 1385–1394.

(19) Kerker, M. Estimation of Surface-Enhanced Raman Scattering from Surface-Averaged Electromagnetic Intensities. *J. Colloid Interface Sci.* **1987**, *118* (2), 417–421.

(20) Tawa, K.; Umetsu, M.; Nakazawa, H.; Hattori, T.; Kumagai, I. Application of 300?? Enhanced Fluorescence on a Plasmonic Chip Modified with a Bispecific Antibody to a Sensitive Immunosensor. *ACS Appl. Mater. Interfaces* **2013**.

(21) Anger, P.; Bharadwaj, P.; Novotny, L. Enhancement and Quenching of Single-Molecule Fluorescence. *Phys. Rev. Lett.* **2006**.

(22) Cho, I. H.; Mauer, L.; Irudayaraj, J. In-Situ Fluorescent Immunomagnetic Multiplex Detection of Foodborne Pathogens in Very Low Numbers. *Biosens. Bioelectron.* **2014**.

(23) Ahmed, S. R.; Hossain, M. A.; Park, J. Y.; Kim, S. H.; Lee, D.; Suzuki, T.; Lee, J.; Park, E. Y. Metal Enhanced Fluorescence on Nanoporous Gold Leaf-Based Assay Platform for Virus Detection. *Biosens. Bioelectron.* **2014**.

(24) Ming, T.; Chen, H.; Jiang, R.; Li, Q.; Wang, J. Plasmon-Controlled Fluorescence: Beyond the Intensity Enhancement. *Journal of Physical Chemistry Letters*. 2012.

(25) Tam, F.; Goodrich, G. P.; Johnson, B. R.; Halas, N. J. Plasmonic Enhancement of Molecular Fluorescence. *Nano Lett.* **2007**.

(26) Lakowicz, J. R. Radiative Decay Engineering 5: Metal-Enhanced Fluorescence and Plasmon Emission.

(27) Vericat, C.; Vela, M. E.; Benitez, G.; Carro, P.; Salvarezza, R. C. Self-Assembled Monolayers of Thiols and Dithiols on Gold: New Challenges for a Well-Known System. *Chem. Soc. Rev.* **2010**, *39* (5), 1805–1834.

(28) Ulman, A. Formation and Structure of Self-Assembled Monolayers. *Chem. Rev.* **1996**, *96* (4), 1533–1553.

(29) Staros, J.; Wright, W. Enhancement by N-Hydroxysulfosuccinimid of Water-Soluble Carbodiimide-Mediated Caoupling Reaction. *Anal. Biochem.* **1986**, *156*, 220–222.

(30) Th. Wink*, S. J. van Zuilen, a. B. and W. P. V. B. Tutorial Review Self-Assembled Monolayers for Biosensors. *Analyst,* **1997**, *122* (April), 43R–50R.

(31) Llewelyn, M. B.; Hawkins, R. E.; Russell, S. J. Monoclonal Antibodies in Medicine: Discovery of Antibodies. *Br. Med. J.* **1992**, *305* (November), 1269–1272.

(32) Jason-Moller, L.; Murphy, M.; Bruno, J. Overview of Biacore Systems and Their Applications. *Curr. Protoc. Protein Sci.* **2006**, 19.13.1-19.13.14.

(33) Malmborg, A. C.; Borrebaeck, C. A. K. BIAcore as a Tool in Antibody Engineering. *J. Immunol. Methods* **1995**, *183* (1), 7–13.

(34) Hantusch, B.; Schöll, I.; Harwanegg, C.; Krieger, S.; Becker, W. M.; Spitzauer, S.; Boltz-Nitulescu, G.; Jensen-Jarolim, E. Affinity Determinations of Purified IgE and IgG Antibodies against the Major Pollen Allergens Phl p 5a and Bet v 1a: Discrepancy between IgE and IgG Binding Strength. *Immunol. Lett.* **2005**, *97* (1), 81–89.

(35) Myszka, D. G.; Jonsen, M. D.; Graves, B. J. Equilibrium Analysis of High Affinity Interactions Using BIACORE. *Anal. Biochem.* **1998**, *265* (2), 326–330.

(36) Myszka, D. G.; He, X.; Dembo, M.; Morton, T. A.; Goldstein, B. Extending the Range of Rate Constants Available from BIACORE: Interpreting Mass Transport-Influenced Binding Data. *Biophys. J.* **1998**, *75* (2), 583–594.

(37) Katsamba, P. S.; Navratilova, I.; Calderon-Cacia, M.; Fan, L.; Thornton, K.; Zhu, M.; Bos, T. Vanden; Forte, C.; Friend, D.; Laird-Offringa, I.; et al. Kinetic Analysis of a High-Affinity Antibody/Antigen Interaction Performed by Multiple Biacore Users. *Anal. Biochem.* **2006**, *352* (2), 208–221.

(38) Roos, H.; Karlsson, R.; Nilshans, H.; Persson, A. Thermodynamic Analysis of Protein Interactions with Biosensor Technology. *J. Mol. Recognit.* **1998**, *11* (1–6), 204–210.

(39) Papalia, G. A.; Giannetti, A. M.; Arora, N.; Myszka, D. G. Thermodynamic Characterization of Pyrazole and Azaindole Derivatives Binding to P38 Mitogen-Activated Protein Kinase Using Biacore T100 Technology and van't Hoff Analysis. *Anal. Biochem.* **2008**, *383* (2), 255–264.

(40) Lipschultz, C. A.; Yee, A.; Mohan, S.; Li, Y.; Smith-Gill, S. J. Temperature Differentially Affects Encounter and Docking Thermodynamics of Antibody-Antigen Association. *J. Mol. Recognit.* **2002**, *15* (1), 44–52.

(41) Navratilova, I.; Papalia, G. A.; Rich, R. L.; Bedinger, D.; Brophy, S.; Condon, B.; Deng, T.; Emerick, A. W.; Guan, H. W.; Hayden, T.; et al. Thermodynamic Benchmark Study Using Biacore Technology. *Anal. Biochem.* **2007**, *364* (1), 67–77.

(42) Malmborg, A. C.; Dueñas, M.; Ohlin, M.; Söderlind, E.; Borrebaeck, C. A. K. Selection of Binders from Phage Displayed Antibody Libraries Using the BIAcore(TM) Biosensor. *J. Immunol. Methods* **1996**, *198* (1), 51–57.

(43) Fivash, M.; Towler, E. M.; Fisher, R. J. BIAcore for Macromolecular Interaction. *Curr. Opin. Biotechnol.* **1998**, *9* (1), 97–101.

(44) Su, K. H.; Wei, Q. H.; Zhang, X.; Mock, J. J.; Smith, D. R.; Schultz, S. Interparticle Coupling Effects on Plasmon Resonances of Nanogold Particles. *Nano Lett.* **2003**, *3* (8), 1087–1090.

(45) Rosi, N. L.; Mirkin, C. A. Nanostructures in Biodiagnostics. *Chem. Rev.* **2005**, *105* (4), 1547–1562.

(46) Reynolds, R. A.; Mirkin, C. A.; Letsinger, R. L. Homogeneous, Nanoparticle-Based Quantitative Colorimetric Detection of Oligonucleotides [13]. *J. Am. Chem. Soc.* **2000**, *122* (15), 3795–3796.

(47) Nakashima, H.; Furukawa, K.; Kashimura, Y.; Torimitsu, K. Anisotropic Assembly of Gold Nanorods Assisted by Selective Ion Recognition of Surface-Anchored Crown Ether Derivatives. *Chem. Commun.* **2007**, *1* (10), 1080–1082.

(48) Schofield, C. L.; Haines, A. H.; Field, R. A.; Russell, D. A. Silver and Gold Glyconanoparticles for Colorimetric Bioassays. *Langmuir* **2006**, *22* (15), 6707–6711.

(49) Ghosh, S. K.; Nath, S.; Kundu, S.; Esumi, K.; Pal, T. Solvent and Ligand Effects on the Localized Surface Plasmon Resonance (LSPR) of Gold Colloids. *J. Phys. Chem. B* **2004**, *108* (37), 13963–13971.

(50) Yu, C.; Irudayaraj, J. Multiplex Biosensor Using Gold Nanorods. *Anal. Chem.* **2007**, *79* (2), 572–579.

(51) Malynych, S.; Chumanov, G. Coupled Planar Silver Nanoparticle Arrays as Refractive Index Sensors. *J. Opt. A Pure Appl. Opt.* **2006**, *8* (4), 0–4.

(52) Nath, N.; Chilkoti, A. A Colorimetric Gold Nanoparticle Sensor to Interrogate Biomolecular Interactions in Real Time on a Surface. *Anal. Chem.* **2002**, *74* (3), 504–509.

(53) Marinakos, S. M.; Chen, S.; Chilkoti, A. Plasmonic Detection of a Model Analyte in Serum by a Gold Nanorod Sensor. *Anal. Chem.* **2007**, *79* (14), 5278–5283.

(54) Wang, H.; Brandl, D. W.; Le, F.; Nordlander, P.; Halas, N. J. Nanorice: A Hybrid Plasmonic Nanostructure. *Nano Lett.* **2006**, *6* (4), 827–832.

(55) Larsson, E. M.; Alegret, J.; Kǎll, M.; Sutherland, D. S. Sensing Characteristics of NIR Localized Surface Plasmon Resonances in Gold Nanorings for Application as Ultrasensitive Biosensors. *Nano Lett.* **2007**, *7* (5), 1256–1263.

(56) Jensen, T. R.; Duval, M. L.; Kelly, K. L.; Lazarides, A. A.; Schatz, G. C.; Van Duyne, R. P. Nanosphere Lithography: Effect of the External Dielectric Medium on the Surface Plasmon Resonance Spectrum of a Periodic Array of Silver Nanoparticles. *J. Phys. Chem. B* **1999**, *103* (45), 9846–9853.

(57) Haes, A. J.; Zou, S.; Schatz, G. C.; Van Duyne, R. P. Nanoscale Optical Biosensor: Short Range Distance Dependence of the Localized Surface Plasmon Resonance of Noble Metal Nanoparticles. *J. Phys. Chem. B* **2004**, *108* (22), 6961–6968.

(58) Sönnichsen, C.; Geier, S.; Hecker, N. E.; Von Plessen, G.; Feldmann, J.; Ditlbacher, H.; Lamprecht, B.; Krenn, J. R.; Aussenegg, F. R.; Chan, V. Z. H.; et al. Spectroscopy of Single Metallic Nanoparticles Using Total Internal Reflection Microscopy. *Appl. Phys. Lett.* **2000**, *77*, 2949–2951.

(59) Sherry, L. J.; Chang, S. H.; Schatz, G. C.; Van Duyne, R. P.; Wiley, B. J.; Xia, Y. Localized Surface Plasmon Resonance Spectroscopy of Single Silver Nanocubes. *Nano Lett.* **2005**, *5* (10), 2034–2038.

(60) Kalyuzhny, G.; Schneeweiss, M. A.; Shanzer, A.; Vaskevich, A.; Rubinstein, I. Differential Plasmon Spectroscopy as a Tool for Monitoring Molecular Binding to Ultrathin Gold Films. *J. Am. Chem. Soc.* **2001**, *123* (13), 3177–3178.

(61) Rindzevicius, T.; Alaverdyan, Y.; Dahlin, A.; Höök, F.; Sutherland, D. S.; Käll, M. Plasmonic Sensing Characteristics of Single Nanometric Holes. *Nano Lett.* **2005**, *5* (11), 2335–2339.

(62) Dahlin, A. B.; Tegenfeldt, J. O.; Hŏŏk, F. Improving the Instrumental Resolution of Sensors Based on Localized Surface Plasmon Resonance. *Anal. Chem.* **2006**, *78* (13), 4416–4423.

(63) Dahlin, A.; Zäch, M.; Rindzevicius, T.; Käll, M.; Sutherland, D. S.; Höök, F. Localised Surface Plasmon Resonance Sensing of Lipid-Membrane-Mediated Biorecognition Events. *J. Am. Chem. Soc.* **2005**, *127* (14), 5043–5048.

(64) Smith, E.; Dent, G. *Modern Raman Spectroscopy - A Practical Approach*; John Wiley & Sons, Inc.: Chichester, England, 2005.

(65) Kneipp, K.; Moskovits, M.; Kneipp, H. *Surface-Enhanced Raman Scattering Physics and Application*; Springer: Berlin HGeidelberg, 2006.

(66) Driscoll, A. J.; Harpster, M. H.; Johnson, P. A. The Development of Surface-Enhanced Raman Scattering as a Detection Modality for Portable in Vitro Diagnostics: Progress and Challenges. *Phys. Chem. Chem. Phys.* **2013**, *15* (47), 20415–20433.

(67) Garcia-Rico, E.; Alvarez-Puebla, R. A.; Guerrini, L. Direct Surface-Enhanced Raman Scattering (SERS) Spectroscopy of Nucleic Acids: From Fundamental Studies to Real-Life Applications. *Chem. Soc. Rev.* **2018**, *47* (13), 4909–4923.

(68) Yuen, J. M.; Shah, N. C.; J, W. J.; Duyne, P. Van. Transcutaneous Glucose Sensing by Surface-Enhanced Spatially Offset Raman Spectroscopy in a Rat Model. *Anal. Chem.* **2010**, *82* (20), 8382.

(69) Zengin, A.; Tamer, U.; Caykara, T. SERS Detection of Hepatitis B Virus DNA in a Temperature-Responsive Sandwich-Hybridization Assay. *J. Raman Spectrosc.* **2017**, *48* (5), 668–672.

(70) Cheng, Z.; Choi, N.; Wang, R.; Lee, S.; Moon, K. C.; Yoon, S. Y.; Chen, L.; Choo, J. Simultaneous Detection of Dual Prostate Specific Antigens Using Surface-Enhanced Raman Scattering-Based Immunoassay for Accurate Diagnosis of Prostate Cancer. *ACS Nano* **2017**, *11* (5), 4926–4933.

(71) Nima, Z. A.; Alwbari, A. M.; Dantuluri, V.; Hamzah, R. N.; Sra, N.; Motwani, P.; Arnaoutakis, K.; Levy, R. A.; Bohliqa, A. F.; Nedosekin, D.; et al. Targeting Nano Drug Delivery to Cancer Cells Using Tunable, Multi-Layer, Silver-Decorated Gold Nanorods. *J. Appl. Toxicol.* **2017**, *37* (12), 1370–1378.

(72) Chang, H.; Kang, H.; Ko, E.; Jun, B. H.; Lee, H. Y.; Lee, Y. S.; Jeong, D. H. PSA Detection with Femtomolar Sensitivity and a Broad Dynamic Range Using SERS Nanoprobes and an Area-Scanning Method. *ACS Sensors* **2016**, *1* (6), 645–649.

(73) Yang, K.; Hu, Y.; Dong, N.; Zhu, G.; Zhu, T.; Jiang, N. A Novel SERS-Based Magnetic Aptasensor for Prostate Specific Antigen Assay with High Sensitivity. *Biosens. Bioelectron.* **2017**, *94* (March), 286–291.

(74) Maneeprakorn, W.; Bamrungsap, S.; Apiwat, C.; Wiriyachaiporn, N. Surface-Enhanced Raman Scattering Based Lateral Flow Immunochromatographic Assay for Sensitive Influenza Detection. *RSC Adv.* **2016**, *6* (113), 112079–112085.

(75) Moon, J.; Yi, S. Y.; Hwang, A.; Eom, G.; Sim, J.; Jeong, J.; Lim, E. K.; Chung, B. H.; Kim, B.; Jung, J.; et al. Facile and Sensitive Detection of Influenza Viruses Using SERS Antibody Probes. *RSC Adv.* **2016**, *6* (87), 84415–84419.

(76) Negri, P.; Dluhy, R. A. Detection of Genetic Markers Related to High Pathogenicity in Influenza by SERS. *Analyst* **2013**, *138* (17), 4877–4884.

(77) Sivashanmugan, K.; Liao, J. Der; You, J. W.; Wu, C. L. Focused-Ion-Beam-Fabricated Au/Ag Multilayered Nanorod Array as SERS-Active Substrate for Virus Strain Detection. *Sensors Actuators, B Chem.* **2013**, *181*, 361–367.

(78) Kamińska, A.; Witkowska, E.; Winkler, K.; Dziecielewski, I.; Weyher, J. L.; Waluk, J. Detection of Hepatitis B Virus Antigen from Human Blood: SERS Immunoassay in a Microfluidic System. *Biosens. Bioelectron.* **2015**, *66*, 461–467.

(79) Karn-Orachai, K.; Sakamoto, K.; Laocharoensuk, R.; Bamrungsap, S.; Songsivilai, S.; Dharakul, T.; Miki, K. Extrinsic Surface-Enhanced Raman Scattering Detection of Influenza A Virus Enhanced by Two-Dimensional Gold@silver Core-Shell Nanoparticle Arrays. *RSC Adv.* **2016**, *6* (100), 97791–97799.

(80) Wei, H.; Hossein Abtahi, S. M.; Vikesland, P. J. Plasmonic Colorimetric and SERS Sensors for Environmental Analysis. *Environ. Sci. Nano* **2015**, *2* (2), 120–135.

(81) Guerrini, L.; Garcia-Ramos, J. V.; Domingo, C.; Sanchez-Cortes, S. Sensing Polycyclic Aromatic Hydrocarbons with Dithiocarbamate- Functionalized Ag Nanoparticles by Surface-Enhanced Raman Scattering. *Anal. Chem.* **2009**, *81* (3), 953–960.

(82) Alak, A. M.; Vo-Dinh, T. Surface-Enhanced Raman Spectrometry of Organophosphorus Chemical Agents. *Anal. Chem.* **1987**, *59* (17), 2149–2153.

(83) Ayora, M. J.; Ballesteros, L.; Pérez, R.; Rupérez, A.; Laserna, J. J. Detection of Atmospheric Contaminants in Aerosols by Surface-Enhanced Raman Spectrometry. *Anal. Chim. Acta* **1997**, *355* (1), 15–21.

(84) Carrabba, M. M.; Edmonds, R. B.; Rauh, R. D. Feasibility Studies for the Detection of Organic Surface and Subsurface Water Contaminants by Surface-Enhanced Raman Spectroscopy on Silver Electrodes. *Anal. Chem.* **1987**, *59* (21), 2559–2563.

(85) Herrmann, H.; Reese, A.; Wicktor, F.; Zellner, R. A Spectroscopic Study of Small Organic Peroxyl Radicals (RO2) in Aqueous Solution. *J. Mol. Struct.* **1997**, *408–409*, 539–542.

(86) Dostálek, J.; Knoll, W. Biosensors Based on Surface Plasmon-Enhanced Fluorescence Spectroscopy (Review). *Biointerphases* **2008**, *3* (3), FD12-FD22.

(87) Lu, L.; Qian, Y.; Wang, L.; Ma, K.; Zhang, Y. Metal-Enhanced Fluorescence-Based Core-Shell Ag@SiO2nanoflares for Affinity Biosensing via Target-Induced Structure Switching of Aptamer. *ACS Appl. Mater. Interfaces* **2014**, *6* (3), 1944–1950.

(88) Yanagawa, H.; Inoue, A.; Sugimoto, H.; Shioi, M.; Fujii, M. Photoluminescence Enhancement of Silicon Quantum Dot Monolayer by Plasmonic Substrate Fabricated by Nano-Imprint Lithography. *J. Appl. Phys.* **2017**, *122* (22).

(89) Biteen, J. S.; Lewis, N. S.; Atwater, H. A.; Mertens, H.; Polman, A. Spectral Tuning of Plasmon-Enhanced Silicon Quantum Dot Luminescence. *Appl. Phys. Lett.* **2006**, *88*, 131109.

(90) Inoue, A.; Fujii, M.; Sugimoto, H.; Imakita, K. Surface Plasmon-Enhanced Luminescence of Silicon Quantum Dots in Gold Nanoparticle Composites. *J. Phys. Chem. C* **2015**, *119* (44), 25108–25113.

(91) Erogbogbo, F.; Yong, K.; Roy, I.; Xu, G.; Prasad, P. N.; Swihart, M. T. Biocompatible Luminescent Silicon. *ACS Nano* **2008**, *2* (5), 873–878.

(92) Smith, A. M.; Mancini, M. C.; Nie, S. Bioimaging: Second Window for in Vivo Imaging. *Nat. Nanotechnol.* **2009**, *4* (11), 710–711.

(93) Aslan, K.; Gryczynski, I.; Malicka, J.; Matveeva, E.; Lakowicz, J. R.; Geddes, C. D. Metal-Enhanced Fluorescence: An Emerging Tool in Biotechnology. *Curr. Opin. Biotechnol.* **2005**, *16* (1 SPEC. ISS.), 55–62.

(94) Yee, K. S. Numerical Solution of Initial Boundary Value Problems Involving Maxwell's Equations in Isotropic Media. *IEEE Trans. Antennas Propag.* **1966**, *14* (3), 302.

(95) Banaee, M. G.; Crozier, K. B. Gold Nanorings as Substrates for Surface-Enhanced Raman Scattering. *Opt. Lett.* **2010**, *35* (5), 760.

(96) Aizpurua, J.; Hanarp, P.; Sutherland, D. S.; Käll, M.; Bryant, G. W.; García de Abajo, F. J. Optical Properties of Gold Nanorings. *Phys. Rev. Lett.* **2003**, *90* (5), 4.

(97) Kim, S.; Jung, J. M.; Choi, D. G.; Jung, H. T.; Yang, S. M. Patterned Arrays of Au Rings for Localized Surface Plasmon Resonance. *Langmuir* **2006**, *22* (17), 7109–7112.

(98) Jung, K. Y.; Teixeira, F. L.; Reano, R. M. Au/SiO2 Nanoring Plasmon Waveguides at Optical Communication Band. *J. Light. Technol.* **2007**, *25* (9), 2757–2765.

(99) Hao, F.; Nordlander, P.; Burnett, M. T.; Maier, S. A. Enhanced Tunability and Linewidth Sharpening of Plasmon Resonances in Hybridized Metallic Ring/Disk Nanocavities. *Phys. Rev. B - Condens. Matter Mater. Phys.* **2007**, *76* (24), 1–6.

(100) Hao, F.; Sonnefraud, Y.; Van Dorpe, P.; Maier, S. A.; Halas, N. J.; Nordlander, P. Symmetry Breaking in Plasmonic Nanocavities: Subradiant LSPR Sensing and a Tunable Fano Resonance. *Nano Lett.* **2008**, *8* (11), 3983–3988.

(101) Ye, J.; Van Dorpe, P.; Lagae, L.; Maes, G.; Borghs, G. Observation of Plasmonic Dipolar Anti-Bonding Mode in Silver Nanoring Structures. *Nanotechnology* **2009**, *20* (46).

(102) Le, F.; Lwin, N. Z.; Halas, N. J.; Nordlander, P. Plasmonic Interactions between a Metallic Nanotube Array and a Thin Metallic Film. *Phys. Rev. B* **2007**, *76*, 165410.

(103) Lévêque, G.; Martin, O. J. F. Tunable Composite Nanoparticle for Plasmonics. *Opt. Lett.* **2006**, *31* (18), 2750.

(104) Chu, Y. Z.; Crozier, K. B. Experimental Study of the Interaction between Localized and Propagating Surface Plasmons. *Opt. Lett.* **2009**, *34* (3), 244–246.

(105) Ye, J.; Chen, C.; Roy, W. Van; Dorpe, P. Van; Maes, G.; Borghs, G. The Fabrication and Optical Property of Silver Nanoplates with Different Thicknesses. *Nanotechnology* **2008**, *19* (32).

(106) Ye, J.; Dorpe, P. Van; Roy, W. Van; Borghs, G.; Maes, G. Fabrication, Characterization, and Optical Properties of Gold Nanobowl Submonolayer Structures. *Langmuir* **2009**, *25* (3), 1822–1827.

(107) Ye, J.; Shioi, M.; Lodewijks, K.; Lagae, L.; Kawamura, T.; Van Dorpe, P. Tuning Plasmonic Interaction between Gold Nanorings and a Gold Film for Surface Enhanced Raman Scattering. *Appl. Phys. Lett.* **2010**, *97* (16).

(108) Ye, J.; Van Dorpe, P.; Van Roy, W.; Lodewijks, K.; De Vlaminck, I.; Maes, G.; Borghs, G. Fabrication and Optical Properties of Gold Nanowire Arrays. *J. Phys. Chem. C* **2009**, *113*, 3110–3115.

(109) Ye, J.; Verellen, N.; Van Roy, W.; Lagae, L.; Maes, G.; Borghs, G.; Van Dorpe, P. Plasmonic Modes of Metallic Semishells in a Polymer Film. *ACS Nano* **2010**, *4* (3), 1457–1464.

(110) Jean Cesario Romain Quidant, G. B.; Cesario, J.; Quidant, R.; Badenes, G.; Enoch, S. Electromagnetic Coupling between a Metal Nanoparticle Grating and a Metallic Surface. *Opt. Lett.* **2005**, *30* (24), 3404–3406.

(111) Osawa, M.; Matsuda, N.; Yoshii, K.; Uchida, I. Charge Transfer Resonance Raman Process in Surface-Enhanced Raman Scattering from p-Aminothiophenol Adsorbed on Silver: Herzberg-Teller Contribution. *J. Phys. Chem.* **1994**, *98* (48), 12702–12707.

(112) Guo, S.; Wang, Y.; Wang, E. Large-Scale, Rapid Synthesis and Application in Surface-Enhanced Raman Spectroscopy of Sub-Micrometer Polyhedral Gold Nanocrystals. *Nanotechnology* **2007**, *18* (40).

(113) Wang, Y.; Chen, H.; Dong, S.; Wang, E. Surface Enhanced Raman Scattering of P-Aminothiophenol Self-Assembled Monolayers in Sandwich Structure Fabricated on Glass. *J. Chem. Phys.* **2006**, *124* (7), 0–8.

(114) Moskovits, M. Surface-Enhanced Spectroscopy. *Rev. Mod. Phys.* **1985**, *57* (3), 783–826.

(115) Otto, A.; Mrozek, I.; Grabhorn, H.; Akemann, W. Surface-Enhanced Raman Scattering. *J. Phys. Condens. Matter Surface-enhanced* **1992**, *4*, 1143.

(116) Shanmukh, S.; Jones, L.; Driskell, J.; Zhao, Y.; Dluhy, R.; Tripp, R. A. Rapid and Sensitive Detection of Respiratory Virus Molecular Signatures Using a Silver Nanorod Array SERS Substrate. *Nano Lett.* **2006**, *6* (11), 2630–2636.

(117) Mulvihill, M.; Tao, A.; Benjauthrit, K.; Arnold, J.; Yang, P. Surface-Enhanced Raman Spectroscopy for Trace Arsenic Detection in Contaminated Water. *Angew. Chemie - Int. Ed.* **2008**, *47* (34), 6456–6460.

(118) Péron, O.; Rinnert, E.; Lehaitre, M.; Crassous, P.; Compère, C. Detection of Polycyclic Aromatic Hydrocarbon (PAH) Compounds in Artificial Sea-Water Using Surface-Enhanced Raman Scattering (SERS). *Talanta* **2009**, *79* (2), 199–204.

(119) Gaponenko, S. V. Effects of Photon Density of States on Raman Scattering in Mesoscopic Structures. *Phys. Rev. B* **2002**, *65* (14), 140303.

(120) Kahl, M.; Voges, E. Analysis of Plasmon Resonance and Surface-Enhanced Raman Scattering on Periodic Silver Structures. *Phys. Rev. B - Condens. Matter Mater. Phys.* **2000**, *61* (20), 14078–14088.

(121) Ghoshal, A.; Divliansky, I.; Kik, P. G. Experimental Observation of Mode-Selective Anticrossing in Surface-Plasmon-Coupled Metal Nanoparticle Arrays. *Appl. Phys. Lett.* **2009**, *94*, 171108.

(122) Chu, Y.; Banaee, M. G.; Crozier, K. B. Double-Resonance Plasmon Substrates for Surface-Enhanced Raman Scattering Stokes Frequencies. *ACS Nano* **2010**, *4* (5), 2804.

(123) Petschulat, J.; Cialla, D.; Janunts, N.; Rockstuhl, C.; Huebner, U.; Moeller, R.; Schneidewind, H.; Mattheis, R.; Popp, J.; Tuennermann, A.; et al. Doubly Resonant Optical Nanoantenna Arrays for Polarization Resolved Measurements of Surface-Enhanced Raman Scattering. *Opt. Express* **2010**, *18* (5), 13.

(124) Kaminska, A.; Inya-Agha, O.; Forster, R. J.; Keyes, T. E. Chemically Bound Gold Nanoparticle Arrays on Silicon: Assembly, Properties and SERS Study of Protein Interactions. *Phys. Chem. Chem. Phys.* **2008**, *10* (28), 4172–4180.

(125) Picorel, R.; Chumanov, G.; Cotton, T. M.; Montoya, G.; Toon, S.; Seibert, M. Surface-Enhanced Resonance Raman Scattering Spectroscopy of Photosystem II Pigment-Protein Complexes. *J. Phys. Chem.* **1994**, *98* (23), 6017–6022.

(126) Shafer-Peltier, K. E.; Haynes, C. L.; Glucksberg, M. R.; Van Duyne, R. P. Toward a Glucose Biosensor Based on Surface-Enhanced Raman Scattering. *J. Am. Chem. Soc.* **2003**, *125* (2), 588–593.

(127) Lee, V. Y.-H.; Farquaharson, S.; Rainey, P. M. Surface-Enhanced Raman Sensor for Trace Chemical Detection in Water.

(128) Schmidt, H.; Ha, N. B.; Pfannkuche, J.; Amann, H.; Kronfeldt, H. D.; Kowalewska, G. Detection of PAHs in Seawater Using Surface-Enhanced Raman Scattering (SERS). *Mar. Pollut. Bull.* **2004**, *49* (3), 229–234.

(129) *CRC Handbook of Chemistry and Physics*; Lide, D., Ed.; CRC Press: Boca Raton, FL, 2000.

(130) *Handbook of Optical Constant of Solids*; Palik, E. D., Ed.; Academic Press: Orlando, FL, 1985.

(131) Johnson, P. B.; Christy, R. W. Optical Constants of Transition Metals: Ti, V, Cr, Mn, Fe, Co, Ni, and Pd. *Phys. Rev. B* **1974**, *9* (12), 15.

(132) *FDTD Solutions Reference Guide*; Lumerical Solutions: Suite 300–535 Thurlow Street Vancouver, BC V6E 3L2, Canada, 2009.

(133) Lodewijks, K.; Ryken, J.; Van Roy, W.; Borghs, G.; Lagae, L.; Van Dorpe, P. Tuning the Fano Resonance Between Localized and Propagating Surface Plasmon Resonances for Refractive Index Sensing Applications. *Plasmonics* **2013**, *8* (3), 1379–1385.

(134) Sönnichsen, C.; Franzl, T.; Wilk, T.; von Plessen, G.; Feldmann, J.; Wilson, O.; Mulvaney, P. Drastic Reduction of Plasmon Damping in Gold Nanorods. *Phys. Rev. Lett.* **2002**, *88* (7), 774021–774024.

(135) Guzatov, D. V.; Vaschenko, S. V.; Stankevich, V. V.; Lunevich, A. Y.; Glukhov, Y. F.; Gaponenko, S. V. Plasmonic Enhancement of Molecular Fluorescence near Silver Nanoparticles: Theory, Modeling, and Experiment. *J. Phys. Chem. C* **2012**, *116* (19), 10723–10733.

(136) Fan, M.; Andrade, G. F. S.; Brolo, A. G. A Review on the Fabrication of Substrates for Surface Enhanced Raman Spectroscopy and Their Applications in Analytical Chemistry. *Anal. Chim. Acta* **2011**, *693* (1–2), 7–25.

(137) Yamamoto, Y. S.; Ishikawa, M.; Ozaki, Y.; Itoh, T. Fundamental Studies on Enhancement and Blinking Mechanism of Surface-Enhanced Raman Scattering (SERS) and Basic Applications of SERS Biological Sensing. *Front. Phys.* **2014**, *9* (1), 31–46.

(138) Stuart, D. A.; Yuen, J. M.; Shah, N.; Lyandres, O.; Yonzon, C. R.; Glucksberg, M. R.; Walsh, J. T.; Van Duyne, R. P. In Vivo Glucose Measurement by Surface-Enhanced Raman Spectroscopy. *Anal. Chem.* **2006**, *78* (20), 7211–7215.

(139) Lyandres, O.; Yuen, J. M.; Shah, N. C.; VanDuyne, R. P.; Walsh, J. T.; Glucksberg, M. R. Progress Toward an In Vivo Surface-Enhanced Raman Spectroscopy Glucose Sensor. *Diabetes Technol. Ther.* **2008**, *10* (4), 257–265.

(140) Ma, K.; Yuen, J. M.; Shah, N. C.; Walsh, J. T.; Glucksberg, M. R.; Van Duyne, R. P. In Vivo, Transcutaneous Glucose Sensing Using Surface-Enhanced Spatially Offset Raman Spectroscopy: Multiple Rats, Improved Hypoglycemic Accuracy, Low Incident Power, and Continuous Monitoring for Greater than 17 Days. *Anal. Chem.* **2011**, *83* (23), 9146–9152.

(141) Shioi, M.; Jans, H.; Lodewijks, K.; Van Dorpe, P.; Lagae, L.; Kawamura, T. Tuning the Interaction between Propagating and Localized Surface Plasmons for Surface Enhanced Raman Scattering in Water for Biomedical and Environmental Applications. *Appl. Phys. Lett.* **2014**, *104*, 243102.

(142) Cui, B.; Clime, L.; Li, K.; Veres, T. Fabrication of Large Area Nanoprism Arrays and Their Application for Surface Enhanced Raman Spectroscopy. *Nanotechnology* **2008**, *19* (14).

(143) Siegfried, T.; Ekinci, Y.; Martin, O. J. F.; Sigg, H. Engineering Metal Adhesion Layers That Do Not Deteriorate Plasmon Resonances. *ACS Nano* **2013**, *7* (3), 2751–2757.

(144) Lamy de la Chapelle, M.; Shen, H.; Guillot, N.; Frémaux, B.; Guelorget, B.; Toury, T. New Gold Nanoparticles Adhesion Process Opening the Way of Improved and Highly Sensitive Plasmonics Technologies. *Plasmonics* **2013**, *8* (2), 411–415.

(145) Goss, C. A.; Charych, D. H.; Majda, M. Application of (3-Mercaptopropyl)Trimethoxysilane as a Molecular Adhesive in the Fabrication of Vapor-Deposited Gold Electrodes on Glass Substrates. *Anal. Chem.* **1991**, *63* (1), 85–88.

(146) Fadeev, A. Y.; McCarthy, T. J. Self-Assembly Is Not the Only Reaction Possible between Alkyltrichlorosilanes and Surfaces: Monomolecular and Oligomeric Covalently Attached Layers of Dichloro- and Trichloroalkylsilanes on Silicon. *Langmuir* **2000**, *16* (18), 7268–7274.

(147) Torul, H.; Boyaci, I. H.; Tamer, U. Attomole Detection of Glyphosate by Surface-Enhanced Raman Spectroscopy Using Gold Nanorods. *Fabad J. Pharm. Sci.* **2010**, *35* (4), 179–184.

(148) Mahony, J.; Chong, S.; Bulir, D.; Ruyter, A.; Mwawasi, K.; Waltho, D. Multiplex Loop-Mediated Isothermal Amplification (M-LAMP) Assay for the Detection of Influenza A/H1, A/H3 and Influenza B Can Provide a Specimen-to-Result Diagnosis in 40min with Single Genome Copy Sensitivity. *J. Clin. Virol.* **2013**.

(149) Molinari, N. A. M.; Ortega-Sanchez, I. R.; Messonnier, M. L.; Thompson, W. W.; Wortley, P. M.; Weintraub, E.; Bridges, C. B. The Annual Impact of Seasonal Influenza in the US: Measuring Disease Burden and Costs. *Vaccine* **2007**.

(150) Yan, J.; Grantham, M.; Pantelic, J.; Bueno de Mesquita, P. J.; Albert, B.; Liu, F.; Ehrman, S.; Milton, D. K. Infectious Virus in Exhaled Breath of Symptomatic Seasonal Influenza Cases from a College Community. *Proc. Natl. Acad. Sci.* **2018**.

(151) Kormuth, K. A.; Lin, K.; Prussin, A. J.; Vejerano, E. P.; Tiwari, A. J.; Cox, S. S.; Myerburg, M. M.; Lakdawala, S. S.; Marr, L. C. Influenza Virus Infectivity Is Retained in Aerosols and Droplets Independent of Relative Humidity. *J. Infect. Dis.* **2018**.

(152) Brankston, G.; Gitterman, L.; Hirji, Z.; Lemieux, C.; Gardam, M. Transmission of Influenza A in Human Beings. *Lancet Infect. Dis.* **2007**, *7* (4), 257–265.

(153) Darwish, I. A. *Immunoassay Methods and Their Applications in Pharmaceutical Analysis: Basic Methodology and Recent Advances*; 2006.

(154) Leirs, K.; Tewari Kumar, P.; Decrop, D.; Pérez-Ruiz, E.; Leblebici, P.; Van Kelst, B.; Compernolle, G.; Meeuws, H.; Van Wesenbeeck, L.; Lagatie, O.; et al. Bioassay Development for Ultrasensitive Detection of Influenza A Nucleoprotein Using Digital ELISA. *Anal. Chem.* **2016**.

(155) Ahn, K. C.; Kim, H.-J.; McCoy, M. R.; Gee, S. J.; Hammock, B. D. Immunoassays and Biosensors for Monitoring Environmental and Human Exposure to Pyrethroid Insecticides. *J. Agric. Food Chem.* **2011**.

(156) Hamers-Casterman, C.; Atarhouch, A.; Muyldermans, S.; Robinson, G.; Hamers, C.; Bajyana Songa, E.; Bendahman, N.; Hamers, R. Naturally Occuring Antibodies Devoid of Light Chains. *Nature* **1993**, *363* (3), 446.

(157) Bever, C. S.; Dong, J. X.; Vasylieva, N.; Barnych, B.; Cui, Y.; Xu, Z. L.; Hammock, B. D.; Gee, S. J. VHH Antibodies: Emerging Reagents for the Analysis of Environmental Chemicals. *Analytical and Bioanalytical Chemistry*. 2016.

(158) Dumoulin, M.; Conrath, K.; Van Meirhaeghe, A.; Meersman, F.; Heremans, K.; Frenken, L. G. J.; Muyldermans, S.; Wyns, L.; Matagne, A. Single-Domain Antibody Fragments with High Conformational Stability. *Protein Sci.* **2009**.

(159) Saerens, D.; Frederix, F.; Reekmans, G.; Conrath, K.; Jans, K.; Brys, L.; Huang, L.; Bosmans, E.; Maes, G.; Borghs, G.; et al. Engineering Camel Single-Domain Antibodies and Immobilization Chemistry for Human Prostate-Specific Antigen Sensing. *Anal. Chem.* **2005**.

(160) Gonzalez-Sapienza, G.; Rossotti, M. A.; Tabares-da Rosa, S. Single-Domain Antibodies as Versatile Affinity Reagents for Analytical and Diagnostic Applications. *Frontiers in Immunology*. 2017.

(161) Li, D.; Cui, Y.; Morisseau, C.; Gee, S. J.; Bever, C. S.; Liu, X.; Wu, J.; Hammock, B. D.; Ying, Y. Nanobody Based Immunoassay for Human Soluble Epoxide Hydrolase Detection Using Polymeric Horseradish Peroxidase (PolyHRP) for Signal Enhancement: The Rediscovery of PolyHRP? *Anal. Chem.* **2017**.

(162) Homola, J. Present and Future of Surface Plasmon Resonance Biosensors. *Anal. Bioanal. Chem.* **2003**, *377* (3), 528–539.

(163) Wang, J.; Mukhtar, H.; Ma, L.; Pang, Q.; Wang, X. VHH Antibodies: Reagents for Mycotoxin Detection in Food Products. *Sensors (Switzerland)*. 2018.

(164) Liebermann, T.; Knoll, W. Surface-Plasmon Field-Enhanced Fluorescence Spectroscopy. *Colloids Surfaces A Physicochem. Eng. Asp.* **2000**.

(165) Petryayeva, E.; Algar, W. R.; Medintz, I. L. Quantum Dots in Bioanalysis: A Review of Applications across Various Platforms for Fluorescence Spectroscopy and Imaging. *Appl. Spectrosc.* **2013**, *67* (3), 215–252.

(166) Zheng, J.; Li, L.; Tsao, H. K.; Sheng, Y. J.; Chen, S.; Jiang, S. Strong Repulsive Forces between Protein and Oligo (Ethylene Glycol) Self-Assembled Monolayers: A Molecular Simulation Study. *Biophys. J.* **2005**.

(167) Kovalchuk, S. I.; Anikanov, N. A.; Ivanova, O. M.; Ziganshin, R. H.; Govorun, V. M. Bovine Serum Albumin as a Universal Suppressor of Non-Specific Peptide Binding in Vials Prior to Nano-Chromatography Coupled Mass-Spectrometry Analysis. *Anal. Chim. Acta* **2015**, *893*, 57–64.

(168) Zhang, Y.; Heller, A. Reduction of the Nonspecific Binding of a Target Antibody and of Its Enzyme-Labeled Detection Probe Enabling Electrochemical Immunoassay of an Antibody through the 7 Pg/ML-100 Ng/ML (40 FM-400 PM) Range. *Anal. Chem.* **2005**, *77* (23), 7758–7762.

(169) Harbers, G. M.; Emoto, K.; Greef, C.; Metzger, S. W.; Woodward, H. N.; Mascali, J. J.; Grainger, D. W.; Lochhead, M. J. Functionalized Poly(Ethylene Glycol)-Based Bioassay Surface Chemistry That Facilitates Bio-Immobilization and Inhibits Nonspecific Protein, Bacterial, and Mammalian Cell Adhesion. *Chem. Mater.* **2007**, *19* (18), 4405–4414.

(170) Prime, K. L.; Whitesides, G. M. Adsorption of Proteins onto Surfaces Containing End-Attached Oligo(Ethylene Oxide): A Model System Using Self-Assembled Monolayers. *J. Am. Chem. Soc.* **1993**, *115* (23), 10714–10721.

(171) Mrksich, M.; Sigal, G. B.; Whitesides, G. M. Surface Plasmon Resonance Permits in Situ Measurement of Protein Adsorption on Self-Assembled Monolayers of Alkanethiolates on Gold. *Langmuir* **1995**, *11* (11), 4383–4385.

(172) Einhauer, A.; Jungbauer, A. Affinity of the Monoclonal Antibody M1 Directed against the FLAG Peptide. *J. Chromatogr. A* **2001**, *921* (1), 25–30.

(173) Ye, Q.; Krug, R. M.; Tao, Y. J. The Mechanism by Which Influenza A Virus Nucleoprotein Forms Oligomers and Binds RNA. *Nature* **2006**.

(174) Frederix, F.; Bonroy, K.; Laureyn, W.; Reekmans, G.; Campitelli, A.; Dehaen, W.; Maes, G. Enhanced Performance of an Affinity Biosensor Interface Based on Mixed Self-Assembled Monolayers of Thiols on Gold. *Langmuir* **2003**.

(175) Bonroy, K.; Frederix, F.; Reekmans, G.; Dewolf, E.; Palma, R. De; Borghs, G.; Declerck, P.; Goddeeris, B. Comparison of Random and Oriented Immobilisation of Antibody Fragments on Mixed Self-Assembled Monolayers. **2006**, *312*, 167–181.

(176) Editorial. Commercializing Plasmonics. *Nat. Photonics* **2015**, *9* (8), 477–477.

(177) Li, J.; Chen, C.; Jans, H.; Xu, X.; Verellen, N.; Vos, I.; Okumura, Y.; Moshchalkov, V. V.; Lagae, L.; Van Dorpe, P. 300 Mm Wafer-Level, Ultra-Dense Arrays of Au-Capped Nanopillars with Sub-10 Nm Gaps as Reliable SERS Substrates. *Nanoscale* **2014**, *6* (21), 12391–12396.

(178) Fratoddi, I.; Venditti, I.; Cametti, C.; Russo, M. V. How Toxic Are Gold Nanoparticles? The State-of-the-Art. *Nano Res.* **2015**, *8* (6), 1771–1799.

(179) Gerber, A.; Bundschuh, M.; Klingelhofer, D.; Groneberg, D. A. Gold Nanoparticles: Recent Aspects for Human Toxicology. *J. Occup. Med. Toxicol.* **2013**, *8*, 32.

(180) Wang, Y. W.; Kang, S.; Khan, A.; Bao, P. Q.; Liu, J. T. C. In Vivo Multiplexed Molecular Imaging of Esophageal Cancer via Spectral Endoscopy of Topically Applied SERS Nanoparticles. *Biomed. Opt. Express* **2015**, *6* (10), 3714.

(181) Harmsen, S.; Bedics, M. A.; Wall, M. A.; Huang, R.; Detty, M. R.; Kircher, M. F. Rational Design of a Chalcogenopyrylium-Based Surface-Enhanced Resonance Raman Scattering Nanoprobe with Attomolar Sensitivity. *Nat. Commun.* **2015**, *6*, 1–9.

(182) Bohndiek, S. E.; Wagadarikar, A.; Zavaleta, C. L.; Van de Sompel, D.; Garai, E.; Jokerst, J. V.; Yazdanfar, S.; Gambhir, S. S. A Small Animal Raman Instrument for Rapid, Wide-Area, Spectroscopic Imaging. *Proc. Natl. Acad. Sci.* **2013**, *110* (30), 12408–12413.

(183) Harmsen, S.; Huang, R.; Wall, M. A.; Karabeber, H.; Samii, J. M.; Spaliviero, M.; White, J. R.; Monette, S.; O'Connor, R.; Singer, S.; et al. Surface-Enhanced Resonance Raman Scattering Nanostars for High Precision Cancer Imaging. *Sci. Transl. Med.* **2015**, *21* (7), 271ra7.

(184) Laing, S.; Jamieson, L. E.; Faulds, K.; Graham, D. Surface-Enhanced Raman Spectroscopy for in Vivo Biosensing. *Nat. Rev. Chem.* **2017**, *1*, 1–20.

List of publications

Journal Papers

- Jian Ye, **Masahiko Shioi,** Kristof Lodewijks, et. al., “Tuning plasmonic interaction between gold nanorings and a gold film for surface enhanced Raman scattering”, *Applied Physics Letters* 97, 163106 (2010）
- **Masahiko Shioi**, Hilde Jans, Kristof Lodewijks, Pol Van Dorpe, Liesbet Lagae, and Tatsuro Kawamura, “Tuning the interaction between propagating and localized surface plasmons for surface enhanced Raman scattering in water for biomedical and environmental applications”, *Applied Physics Letters* 104, 243102 (2014);
- Yasuaki Okumura, Hilde Jans, Pol van Dorpe, Jiaqi Li, Masaru Minamiguchi, **Masahiko Shioi**, Lieven Vlaminck, Liesbet Lagae, and Tatsuro Kawamura, “Robustness of surface-enhanced Raman scattering substrate with a mercaptosilane adhesive layer for in vivo sensing applications”, *Japanese Journal of Applied Physics* 54, 067002 (2015)
- **Masahiko Shioi**, Emina Ikeuchi, Hiroto Yanagawa, Noriko Shimba, Shunsuke Kori, Kouhei Tsumoto and Minoru Fujii, ” VHH-based immunoassay for influenza A nucleoprotein using surface enhanced fluorescence”, Submitted to “*Biochemical and Biophysical Research Communications*” (2019/1)

- Takahiro Aoki, Yasuaki Okumura, **Masahiko Shioi**, and Tatsuro Kawamura, “Evaluation of PEG-SAM Stabilities and Inhibition of Nonspecific Protein Adsorption during Storage for 2 Months” , *Chemistry Letters* 44, 1661–1663 (2015)
- Hiroto Yanagawa, Asuka Inoue, Hiroshi Sugimoto, **Masahiko Shioi,** Minoru Fujii, “Photoluminescence enhancement of silicon quantum dot monolayer by plasmonic substrate fabricated by nano-imprint lithography”, Journal of Applied physics 122, 22, 223101 (2017)

Patents

(Only original applications and related to this thesis)

- Pol Van Dorpe, Kristof Lodewijks, Masahiko SHIOI, Jian Ye, EP101015726.8 (Filed: 2010/3/22)
- 塩井 正彦、Kristof Lodewijks, Pol Van Dorpe, Hilde Jans、特願 2012-1479（出願日：2012/1/6）
- Hilde Jans, Masahiko SHIOI, Karolien Jans, Liesbet Lagae, US1361/765,367 (Filed: 2013/2/15)
- 柳川 博人、塩井 正彦、西尾 和晃, 池内 江美奈 特願 2017-181836 (出願日：2017/9/21)

Book

- 奥村 泰章、塩井 正彦、"バイオチップの基礎と応用　ー原理から最新の研究・開発動向まで"　第 2 編 8 章： 伊藤嘉浩監修、株式会社シーエムシー出版　（2015）

Acknowledgement

Quite a long time has been passed since I came back to Japan from Belgium where I had enjoyed doing research with nice foreign colleagues for 2 years. The experience in Belgium made me feel trying to take a degree to become a full-fledged researcher both in name and reality.

Panasonic has collaborative laboratories with Kobe University, that’s why I came to know about Fujii Laboratory and their scientific activities which are quite interesting and exciting. The greatest appreciation and respect goes to Prof. Minoru Fujii to give me the opportunity to learn under him through my doctoral course while working at Panasonic. I always troubled him because my slow academic activities. And I learned quite a lot from him, from how to write a paper to ideal relationship between academia and industry.

To my PhD jury members, Prof. Takashi Kita and Prof. Toshifumi Takeuchi, thank you for reviewing my thesis and the constructive comments and helpful discussion.

I would like to thank Prof. Kouhei Tsumoto, department of bioengineering, school of engineering, the University of Tokyo for his helpful comments and insightful suggestions and discussion for VHH immunoassay developments.

I would like to express my acknowledgment to my former “big boss” Dr. Toshihiko Yoshioka who gave me the opportunity to learn at Fujii laboratory. He taught me a lot of quite important issues about how to bridge a research to a industrialization of biosensor and management.

I would like to thank my colleagues at Panasonic for daily supports and insightful suggestions. Special thanks to Tojo-san for teaching me many important things about management, Kawamura-san, Yanagawa-san, Wakita-san, Sasaki-san, and Kanno-san for optical sensing issues, Ikeuchi-san, Shimba-san, Kori-san, Yugawa-san, and Kushida-san for immunoassay issues.

I would also like to acknowledge my current colleagues at Eco solutions Company, Takahama-san, Tsubaki-san, Maruo-san, Konaka-san, Yano-san, Takano-san, Sakaguchi-san, Ueya-san, Yamaguchi-san, and also Kori-san for cooperation to completion of my PhD thesis.

I really appreciate to my colleagues at imec, Belgium, Liesbet, Tim (Stakenborg), Pol, Jian, Kristof, Karolien, Hilde, Jesse, and Tim (Steylaerts). I learned quite a lot about plasmonics and FDTD simulation, surface chemistry, fabrication technique, biocompatibility and how to enjoy collaborative research and Belgian life from all of you.

I cannot thank Dr. Yasuaki Okumura enough for his helpful and insightful suggestions for entire work at both Panasonic and imec. I really enjoyed bringing our projects forward with you.

To my dear parents and sister, and family in law. Thank you for your continuous supports which always give me encouraged.

To my dear wife Masayo. You are always there with lovely smile which always gives me a will and power to overcome my difficulties in work. You always give me joy, energy, happiness, peace of mind, and love, which completely blow off my tiredness and negative state of mind. Thanks!

Last, to my dear sons, Soma and Keima. I have troubled both of you because you had to go to Belgian school even though you couldn’t speak Dutch. But finally, you got to speak Dutch and enjoyed Belgian school life! It is always our great pleasure to see your growth. Also, I couldn’t do something with you because I worked on this thesis even weekends. After completion of my PhD thesis, let’s go fishing!

Masahiko SHIOI

January, 2019

Osaka, Japan

Doctor Thesis, Kobe University

“Surface Enhanced Spectroscopy for Biosensing Applications”, 139 pages

Submitted on January, 22nd. 2019

The date of publication is printed in cover of repository version published

in Kobe University Repository Kernel.